SYSTEM-LEVEL SEISMIC PERFORMANCE QUANTIFICATION OF REINFORCED MASONRY BUILDINGS WITH BOUNDARY ELEMENTS

SYSTEM-LEVEL SEISMIC PERFORMANCE QUANTIFICATION OF REINFORCED MASONRY BUILDINGS WITH BOUNDARY ELEMENTS

By

Mohamed Sayed Hassan Mohamed Ezzeldin

B.Sc., M.Sc.

A Thesis Submitted to the School of Graduate Studies in Partial Fulfillment of the Requirements for the Degree Doctor of Philosophy

McMaster University

December 2016

Doctor of Philosophy (2016) McMaster University

(Civil Engineering) Hamilton, Ontario

TITLE:	SYSTEM-LEVEL SEISMIC PERFORMANCE QUANTIFICATION OF REINFORCED MASONRY BUILDINGS WITH BOUNDARY ELEMENTS
AUTHOR:	Mohamed Ezzeldin B.Sc., M.Sc. (AinShams University)
SUPERVISORS:	Dr. Wael El-Dakhakhni Dr. Lydell Wiebe
NUMBER OF PAGES:	xviii, 228

Abstract

The traditional construction practice used in masonry buildings throughout the world is limited to walls with rectangular cross sections that, when reinforced with steel bars, typically accommodate only single-leg horizontal ties and a single layer of vertical reinforcement. This arrangement provides no confinement at the wall toes, and it may lead to instability in critical wall zones and significant structural damage during seismic events. Conversely, the development of a new building system, constructed with reinforced masonry (RM) walls with boundary elements, allows closed ties to be used as confinement reinforcement, thus minimizing such instability and its negative consequences. Relative to traditional walls, walls with boundary elements have enhanced performance because they enable the compression reinforcement to remain effective up to much larger displacement demands, resulting in a damage tolerant system and eventually, more resilient buildings under extreme events.

Research on the *system-level* (complete building) performance of RM walls with boundary elements is, at the time of publication of this dissertation, nonexistent in open literature. What little research has been published on this innovative building system has focused only on investigating the *component-level* performance of RM walls with boundary elements under lateral loads. To address this knowledge gap, the dissertation presents a comprehensive research program that covered: component-level performance simulation; system-level (complete building) experimental testing; seismic risk assessment tools; and simplified analytical models to facilitate adoption of the developed new building system. In addition, and in order to effectively mobilize the knowledge generated through the research program to stakeholders, the work has been directly related to building codes in Canada and the USA (NBCC and ASCE-7) as well as other standards including FEMA P695 (FEMA 2009) (Chapter 2), TMS 402 and CSA S304 (Chapter 3), FEMA P58 (FEMA 2012) (Chapter 4), and ASCE-41 (Chapter 5).

Chapter 1 of the dissertation highlights its objectives, focus, scope and general organization. The simulation in Chapter 2 is focused on evaluating the component-level overstrength, period-based ductility, and seismic collapse margin ratios under the maximum considered earthquakes. Whereas previous studies have shown that traditional RM walls might not meet the collapse risk criteria established by FEMA P695, the analysis presented in this chapter clearly shows that RM shear walls with boundary elements not only meet the collapse risk criteria, but also exceed it with a significant margin.

Following the component-level simulation presented in Chapter 2, Chapter 3 focused on presenting the results of a complete two-story asymmetrical RM shear wall building with boundary elements, experimentally tested under simulated seismic loading. This effort was aimed at demonstrating the discrepancies between the way engineers design buildings (as individual components) and the way these buildings actually behave as an integrated *system*, comprised of these

components. In addition, to evaluate the enhanced resilience of the new building system, the tested building was designed to have the same lateral resistance as previously tested building with traditional RM shear walls, thus facilitating direct comparison. The experimental results yielded two valuable findings: 1) it clearly demonstrated the overall performance enhancements of the new building system in addition to its reduced reinforcement cost; and 2) it highlighted the drawbacks of the building acting as a system compared to a simple summation of its individual components. In this respect, although the slab diaphragm-wall coupling enhanced the building lateral capacity, this enhancement also meant that other unpredictable and undesirable failure modes could become the weaker links, and therefore dominate the performance of the building system. Presentation of these findings has attracted much attention of codes and standards committees (CSA S304 and TMS 402/ACI 530/ASCE 5) in Canada and the USA, as it resulted in a paradigm shift on how the next-generation of building codes (NBCC and ASCE-7) should be developed to address system-levels performance aspects.

Chapter 4 introduced an innovative system-level risk assessment methodology by integrating the simulation and experimental test results of Chapters 2 and 3. In this respect, the experimentally validated simulations were used to generate new *system-level* fragility curves that provide a realistic assessment of the *overall* building risk under different levels of seismic hazard. Although, within the scope of this dissertation, the methodology has been applied only on buildings constructed with RM walls with boundary elements, the developed new methodology is expected to be adopted by stakeholders of other new and existing building systems and to be further implemented in standards based on the current FEMA P58 risk quantification approaches.

Finally, and in order to translate the dissertation findings into tools that can be readily used by stakeholders to design more resilient buildings in the face of extreme events, simplified backbone and hysteretic models were developed in Chapter 5 to simulate the nonlinear response of RM shear wall buildings with different configurations. These models can be adapted to perform the nonlinear static and dynamic procedures that are specified in the ASCE-41 standards for both existing and new building systems. The research in this chapter is expected to have a major positive impact, not only in terms of providing more realistic model parameters for exiting building systems, but also through the introduction of analytical models for new more resilient building systems to be directly implemented in future editions of the ASCE-41.

This dissertation presents a cohesive body of work that is expected to influence a real change in terms of how we think about, design, and construct buildings as complex *systems* comprised of individual components. The dissertation's overarching hypothesis is that previous disasters have not only exposed the vulnerability of traditional building systems, but have also demonstrated the failure of the current *component-by-component* design approaches to produce resilient building *systems* and safer communities under extreme events.

Dedications

To Sayed & Madiha,

Abdelwahab & Azzah,

Nirmeen,

Jana & Lara

Acknowledgments

I would like to express my deep appreciation to my supervisors Dr. Wael El-Dakhakhni and Dr. Lydell Wiebe. I was lucky to be supervised by such advisors with their encouragement, support, advices, and innovative ideas. I am especially grateful for our discussions that significantly impacted the quality of the dissertation. Special thanks are due to my supervisory committee members, Dr. Siva Sivakumaran and Dr. Yiping Guo for their valuable advice and suggestions. Their helpful comments and discussions during our meetings are greatly appreciated.

The experimental work would not be possible without the help of my peers and colleagues: Ahmed Siam, Tarek El Hashimy, Shady Salem, Ahmed Ghith, Ahmed Ismail, Omar El-Azizy, Vidhey Addepally, Yasser Al-Anany, Mustafa Siyam and Yasser Khalifa. They really helped me a lot and no words can express my gratitude to each of them enough. Deep thanks to my friend Ahmed Ashour for helping me during all the phases of the experimental work. A word of thanks is due to the Applied Dynamic Laboratory technicians Mr. Paul Heerema and Mr. Kent Wheeler for their unwavering help. Finally, many thanks due to my former masters supervisors in AinShams University whom introduced me to the fundamentals of structural engineering, Drs. Hesham Al-Arabaty, and Saleh Mekkawy.

I am thankful for the research funding support provided through the Natural Sciences and Engineering Research Council (NSERC) of Canada, and the Canada Masonry Design Centre (CMDC). Many thanks to Mr. David Stubbs and Dr. Bennett Banting of CMDC for providing valuable comments on the reinforced masonry practice in Canada, and for the expert masons Mr. Tim Maxson and Mr. Mario De Nicola. Support was also provided by the McMaster University Centre for Effective Design of Structures (CEDS), funded through the Ontario Research and Development Challenge Fund (ORDCF) of the Ministry of Research and Innovation (MRI). The provision of the scaled blocks through a grant from the Canadian Concrete Masonry Producers Association (CCMPA) is gratefully acknowledged.

At last but by no means the least, I would like to say that no words can express my sincere gratitude to my parents, Sayed and Madiha, to my brother, Ahmed, my sisters, Sarah and Hagar, my sisters-in-law, Niveen and Nourhan, my brother-in-law, Mohamed, for their patience, care, support and for everything they did, and are still doing for me. Without their continuous support, love, prayer and encouragement throughout my life I would have never been the one I am now. Many thanks to my father- and mother-in-law, Abdelwahab and Azzah, for their continuous care and support. Special thanks are due to my wife, Nirmeen, for her patience, understanding, and unwavering encouragement and support throughout both the tough and the good times at McMaster. She has happily supported me far beyond her fair share. I would also like to acknowledge my daughters (my little pumpkins), Jana and Lara, for their innocent and positive energy that eased the long nights of work.

Co-Authorship

This thesis has been prepared in accordance with the regulations for a sandwich thesis format or as a compilation of research papers stipulated by the faculty of graduate studies at McMaster University. This research presents experimental and analytical work carried out solely by Mohamed Ezzeldin. Advice and guidance were provided for the whole thesis by the academic supervisors Dr. Wael El-Dakhakhni and Dr. Lydell Wiebe. Information presented from outside sources, which has been used towards analysis or discussion, has been cited where appropriate; all other materials are the sole work of the author. This thesis consists of the following manuscripts in the following chapters:

Chapter 2

Ezzeldin, M., Wiebe, L., and El-Dakhakhni, W. (2016). "Seismic Collapse Risk Assessment of Reinforced Masonry Walls with Boundary Elements using the FEMA P695 Methodology." *J. Struct. Eng*., 142(11), 04016108.

Chapter 3

Ezzeldin, M., El-Dakhakhni, W., and Wiebe, L. (2016). "Experimental Assessment of the System-Level Seismic Performance of an Asymmetrical Reinforced Concrete Block Wall Building with Boundary Elements." *J. Struct. Eng*., 10.1061/(ASCE)ST.1943-541X.0001790.

Chapter 4

Ezzeldin, M., Wiebe, L., and El-Dakhakhni, W. (2016). "System-Level Seismic Risk Assessment Methodology: Application to Reinforced Masonry Buildings with Boundary Elements." *J. Struct. Eng*., submitted for publication in July 2016.

Chapter 5

Ezzeldin, M., El-Dakhakhni, W., and Wiebe, L. (2016). "Reinforced Masonry Building Seismic Response Models for ASCE/SEI-41." *J. Struct. Eng*., submitted for publication in November 2016.

Table of Content

List of Figures

List of Tables

CHAPTER 1
INTRODUCTION

1.1 BACKGROUND AND MOTIVATION

Reinforced Masonry (RM) shear walls with traditional rectangular cross sections are usually constructed with single-leg horizontal reinforcement and a single layer of vertical reinforcement because of practical limitations associated with standard concrete masonry unit (CMU) configurations used in North America (see the two-cell 190-mm block shown in Fig. 1.1(a)). Such CMU configurations and reinforcement arrangements provide no confinement at the wall toes, and may lead to instability in critical wall zones and structural damage during seismic events (Shedid et al. 2010). Conversely, boundary elements at the wall ends allow closed ties to replace the typical 180° hook formed by the horizontal shear reinforcement, and they also accommodate multiple layers of vertical bars, as shown in Fig. 1.1(b). This creates a reinforcement cage that confines the wall region subjected to high compressive stresses, and thus delays buckling of the wall's vertical reinforcement (Banting and El-Dakhakhni 2012; and Cyrier 2012). As a result, the compression reinforcement remains effective up to much higher displacement demands after the CMU face shell has spalled, thus enhancing the overall performance and resulting in a more resilient seismic force resisting system (SFRS) under extreme events.

Very little research has been carried out on the performance of RM walls with boundary elements under lateral load because early methods of confining masonry were focused on developing applications that are specifically tailored for walls with rectangular cross sections. More specifically, research was focused on introducing alternative materials that could be placed within CMU to provide confining effects. For example, steel plates were placed on the mortar bed joints of the units to confine masonry (Priestley and Bridgeman 1974; Priestley and Elder 1982). This technique had the effect of increasing the ultimate compressive strain in the confined masonry and thus increasing the overall displacement ductility capacity of the wall. Hart et al. (1988) proposed different types of steel confinement reinforcement (e.g. closed wire mesh and seismic combs) to improve the post-peak behavior of RM prisms. More recent work focused on confinement of unreinforced grouted concrete block using two types of welded wire mesh (Dhanasekar and Shrive 2002) to confine the grouted cells in unreinforced concrete block prisms. The wire mesh proved to be an effective means of increasing the peak compressive strength. The previous methods have the benefit of increasing the compressive strain capacity of the masonry, but they do not offer stability enhancement for a single row of vertical reinforcement. However, the introduction of masonry boundary elements detailed as confined masonry column pilasters not only minimizes the wall structural damage and instability, but also does not deviate from traditional masonry construction practice. As such, the use of boundary elements presents an attractive opportunity for practical application and formalized prescriptive design code requirements (Shedid et al. 2010 and Banting and El-Dakhakhni 2012).

Previous research work has also indicated that there are some key system-level aspects (e.g. slab's in-plane and out-of-plane rigidity) that cannot be quantified through component-level studies (i.e. individual walls). As such, several experimental studies have been conducted on RM walls at the system-level (i.e. complete buildings). Abrams (1986) studied the effect of wall openings on the seismic response of full scale RM shear wall building tested under a quasi-static cyclic loading. Abrams and Paulson (1991) tested three 1/4 scale buildings within the Technical Coordinating Committee for Masonry Research (TCCMAR) program. The authors reported that masonry can dissipate energy under seismic loading with an acceptable level of ductility. Within the same program, Seible et al. (1993) tested a full-scale five-story building under simulated seismic load and reported the building reached significant displacement ductility in both directions. Tomaževič and Weiss (1994) tested two 1/5 scale buildings under dynamic loading. The first unreinforced masonry building showed poor energy dissipation with a soft story failure mechanism, while the other RM building showed higher energy dissipation with a failure mechanism of coupled shear walls. Zonta et al. (2001) subjected a 1/3 scale RM building to scaled accelerations for the purposes of quantifying the building ductility and the effects of using a reduced scale model. Mavros et al. (2016) tested a two-story RM building under dynamic loading and reported that slab flexural coupling was an important system-level aspect that affected the overall RM building performance. This included the building stiffness, lateral resistance capacity, and trend of stiffness degradation, which in turn would significantly change the overall building response under seismic loading.

All the published experimental studies to date have been performed for traditional rectangular RM wall components and systems. For this reason, North American building codes (NBCC and ASCE-7) and standards (TMS 402 and CSA S304) provide a set of seismic response modification factors and prescriptive reinforcement detailing requirements for such traditional systems only. Conversely, RM walls with boundary elements are an innovative building system. Therefore, these codes and standards have not provided design requirements for this building system due the lack of research on their performance. For example, the Masonry Standards Joint Committee has not yet established requirements for longitudinal and transverse reinforcement of such a system and has recommended in the commentary to *Clause 9.3.6.5.5* that "*more testing is needed to facilitate the development of prescriptive design requirements*" (MJSC 2013).

Although presenting the results of a standalone project, this dissertation also represents the fourth phase (*Phase IV)* of a multi-phase research program that was initiated at McMaster University to facilitate a better understanding of the discrepancies between the component- and system-level seismic response of RM shear walls buildings without and with boundary elements. *Phase I* was reported by Siyam et al. (2015), where the experimental program focused on the flexural response of six reduced-scale two-story fully grouted RM shear walls under a displacement-controlled quasi-static cyclic fully-reversed loading. This first phase assessed the component-level performance of RM walls with different configurations and aspect ratios. *Phase II*, reported by Heerema et al. (2015), was focused on testing identical walls to those studied in *Phase I*, but within a scaled two-story asymmetrical RM shear wall building (referred to as *Building II* hereafter), as shown in Fig. 1.2(a). In *Phase II*, the level of coupling between walls during the test was minimized in order to isolate and quantify the torsional response of the building. This was done by detailing the building with hinge lines along the two floor slabs, as shown in Fig. 1.2(b), in order to prevent coupling and to enable in-plane diaphragm rotation and subsequent building twist. In *Phase III*, the building reported by Ashour et al. (2016), referred to as *Building III* hereafter, was identical to that studied in *Phase II*, but without hinge lines in order to investigate the effects of wall coupling on the building and wall response. All walls in *Phases I, II* and *III* had traditional rectangular cross sections.

The main motivation behind *Phase IV*, presented in the current dissertation, is to facilitate the adoption of RM walls with boundary elements as a new resilient SFRS in North American codes and standards. In this respect, this dissertation first presents a simulation that focuses on seismic collapse risk assessment of RM walls with boundary elements at the component-level, following the FEMA P695 (FEMA 2009) methodology. The assessment focuses on evaluating the wall overstrength, period-based ductility, and seismic collapse margin ratios under the maximum considered earthquake (MCE). Following the component-level simulation, the dissertation focuses on presenting the results of a complete two-story asymmetrical RM shear wall building with boundary elements, experimentally tested within *Phase IV* (referred to as *Building IV* hereafter) under simulated seismic loading. The RM shear walls in *Building IV* are designed to have the same lateral resistance as their counterparts in *Building III* to evaluate the enhanced resilience of the new building system. However, the RM shear walls located along the main direction of loading in *Building III* are replaced by RM shear walls with confined boundary elements, as shown in Fig. 1.3. The experimental results of *Buildings II*, *III* and *IV* are subsequently used to develop an innovative system-level risk assessment methodology in an effort to provide a more realistic methodology that can be adapted in the future editions of standards based on the current FEMA P58 (FEMA 2012) risk quantification assessment. Finally, the dissertation develops simplified backbone and hysteretic models for simulating the nonlinear response of RM shear wall buildings with different configurations. These models can be adapted by practicing engineers and code developers to perform the nonlinear static procedure (NSP) and nonlinear dynamic procedure (NDP), specified in North American codes and standards. (e.g. ASCE/SEI 41-13).

1.2 RESEARCH OBJECTIVES

The main objective of this dissertation is to provide necessary data to support the codification of RM shear walls with boundary elements. To do this, the following objectives were defined:

1) Assessing the collapse margin ratios of RM walls with boundary elements under MCE at the component-level through nonlinear incremental dynamic analysis (IDA).
2) Quantifying several aspects pertaining to the system-level seismic performance of RM shear wall buildings with boundary elements.
3) Proposing a methodology, with two different approaches (component seismic losses and component strengths), for the generation of fragility curves that can be adopted for different SFRS.
4) Developing simplified analytical backbone and hysteretic models that account for the observed system-level influences and that can be adopted in force- or displacement-base seismic design approaches.

1.3 ORGANIZATION OF THE DISSERTATION

This dissertation comprises six chapters:

- Chapter 1 presents the motivation and objectives of the dissertation as well as background information pertaining to the research program.
- Chapter 2 contains seismic collapse risk assessment of 20 RM walls with boundary elements at the component-level, following the FEMA P695 (FEMA 2009) methodology. These walls are designed for the same seismic performance factors as previously reported RM shear walls without boundary elements to evaluate the enhanced performance of the new building system.. Afterwards, NSP analyses and IDA are performed following the FEMA P695 methodology. Finally, the analysis results are compared to corresponding results for traditional RM shear walls in terms of equivalent safety against collapse risk under the MCE.
- Chapter 3 contains a description of the experimental program, building layout, test setup, loading protocol and instrumentation of *Building IV*. Following the experimental program description, the chapter focuses on quantifying the effects of boundary elements on the system-level response by comparing the damage sequence and the load-displacement hysteretic behavior between *Buildings III* and *IV*. Finally, the twist angles of *Buildings III* and *IV* are compared at different drift levels throughout the tests, in order to evaluate the effects of boundary elements on the twist

response.

- Chapter 4 proposes an innovative methodology for generating system-level fragility curves for shear wall buildings with boundary elements. This methodology is designed to integrate the contributions of multiple structural components with distinct fragilities to the overall seismic fragility of the complete building system. In this respect, a fiber-based three-dimensional numerical model of RM shear wall buildings is developed and validated using the experimental results of *Phases II, III* and *IV*. Following the model validation, fragility curves are developed at different damage states for the components of an archetype building by performing NDP analyses on the building using a suite of 44 ground motion records. Finally, these individual component fragilities are combined using two different proposed approaches, component seismic losses and component strengths, to generate the overall system-level fragility curves.
- Chapter 5 presents the development of backbone and hysteretic models for simulating the nonlinear response of RM shear wall buildings with different configurations that account for the observed system-level influences and can be adapted to perform the NSP and NDP, respectively. In this respect, a backbone analytical model is developed and validated against the experimental results of *Phase III* and *IV*. The current

parameters assigned to RM shear walls in ASCE/SEI 41-13 (ASCE 2014) are then assessed and a new set of modified parameters are proposed and validated. The developed backbone model is subsequently utilized to create a concentrated plasticity (spring) model in *OpenSees* (McKenna et al. 2000) to simulate the hysteretic response of RM shear wall buildings. Finally, the proposed spring model is shown to capture the experimentally observed hysteretic response in terms of the most relevant characteristics, including the initial stiffness, peak load, stiffness degradation, strength deterioration, hysteretic shape and pinching behavior at different drift levels.

- Chapter 6 presents the dissertation summary, major conclusions and recommendations for future research.

It should be noted that although each chapter presents a standalone journal manuscript, Chapters 2, 3, 4 and 5 collectively describe a cohesive research program as outlined in this introduction chapter of the dissertation. Nonetheless, for completeness of the individual standalone chapters/manuscripts, some overlap might exist including the building layout and the wall configurations.

1.4 REFERENCES

Abrams, D. (1986). “Measured hysteresis in a masonry building system.” Proc., 3rd *U.S. Conference on Earthquake Engineering*, Charleston, SC.

Abrams, D., & Paulson, T. (1991). “Modeling earthquake response of concrete masonry building structures.” *ACI structural Journal*, 88(4).

ASCE/SEI (Structural Engineering Institute). (2014). “Seismic Evaluation and Retrofit of Existing Buildings.” *ASCE/SEI 41-13*, Reston, VA.

Ashour, A., El-Dakhakhni, W., and Shedid, M. (2016). “Experimental evaluation of the system-level seismic performance and robustness of an asymmetrical reinforced concrete block building.” *J. of Struct. Eng.*, 04016072.

Banting, B., and El-Dakhakhni, W. (2012). ”Force-and displacement-based seismic performance parameters for reinforced masonry structural walls with boundary elements.” *J. Struct. Eng*., 10.1061/(ASCE)ST.1943-541X.0000572, 1477–1491.

Cyrier, W. B. (2012). “Performance of concrete masonry shear walls with integral confined concrete boundary elements” Ph.D. dissertation, Washington State Univ.

Dhanasekar, M., and Shrive, N., G. (2002). “Strength and deformation of confined and unconfined grouted masonry.” *ACI Struct. J*., 99(6), 819-826.

FEMA. (2012). “*Seismic performance assessment of buildings.*” *FEMA P58-1*, Washington, DC.

FEMA. (2009). “Quantification of building seismic performance factors.” *FEMA P695*, Washington, DC.

Hart, G. C., Noland, J. L., Kingsley, G. R., Englekirk, R. E., and Sajjad, N. A. (1988). “The use of confinement steel to increase the ductility in reinforced masonry shear walls.” *Masonry Soc. J.*, 7(2), 19-42.

Heerema, P., Ashour, A., Shedid, M., and El-Dakhakhni, W. (2015). "System-level displacement and performance-based seismic design parameter quantifications for an asymmetrical reinforced concrete masonry building." *J. Struct. Eng*., 10.1061/(ASCE)ST.1943- 541X.0001258 04015032.

Mavros, M., Ahmadi, F., Shing, P. B., Klingner, R. E., McLean, D., and Stavridis, A. (2016). “Shake-table tests of a full-scale two-story shear-dominated reinforced masonry wall structure”. *J. Struct. Eng.*, 04016078.

McKenna, F., Fenves, G. L., and Scott, M. H. (2000). *Open system for earthquake engineering simulation*, Univ. of California, Berkeley, Calif., http://opensees.berkeley.edu.

MSJC (Masonry Standards Joint Committee). (2013). “Building code requirements for masonry structures.” *TMS 402-13/ASCE 5-13/ACI 530-13*, ASCE, Reston, VA.

Priestley, M., J., N. and Bridgeman, D., O. (1974). “Seismic resistance of brick masonry walls.” *Bulletin of the New Zealand National Society for Earthquake Engine*ering, 7(4), 167-187.

Priestley, M., J., N., and Elder, D., M. (1982). *Seismic Behaviour of Slender Concrete Masonry Shear Walls*. Research Report, University of Canterbury, Christchurch, New Zealand.

Seible, F., Hegemier, G., Priestley, M. J. N., Kingsley, G., Igarashi, A., and Kurkchubasche A. (1993). "Preliminary results from the TCCMAR 5- story full scale reinforced masonry research building test." *The Masonry Society Journal*, 12(1), 53-60.

Shedid, M. T., El-Dakhakhni, W. W. and Drysdale, R. G. (2010). "Alternative strategies to enhance the seismic performance of reinforced concrete-block shear wall systems." *J. Struct. Eng*., 136(6), 676-689.

Siyam, M., El-Dakhakhni, W., Shedid, M., and Drysdale, R. (2015). "Seismic response evaluation of ductile reinforced concrete block structural walls. I: experimental results and force-based design parameters." *J. Perform. Constr. Facil.* , 10.1061/(ASCE)CF.1943-5509.0000794, 04015066.

Tomaževič, M., and Weiss, P. (1994). "Seismic behavior of plain- and reinforced masonry buildings." *J. Struct. Eng*., 120(2), 323-338.

Zonta, D., Zanardo, G., and Modena, C. (2001). "Experimental evaluation of the ductility of a reduced-scale reinforced masonry building." *Mater. Struct*., 34 (10), 636-644.

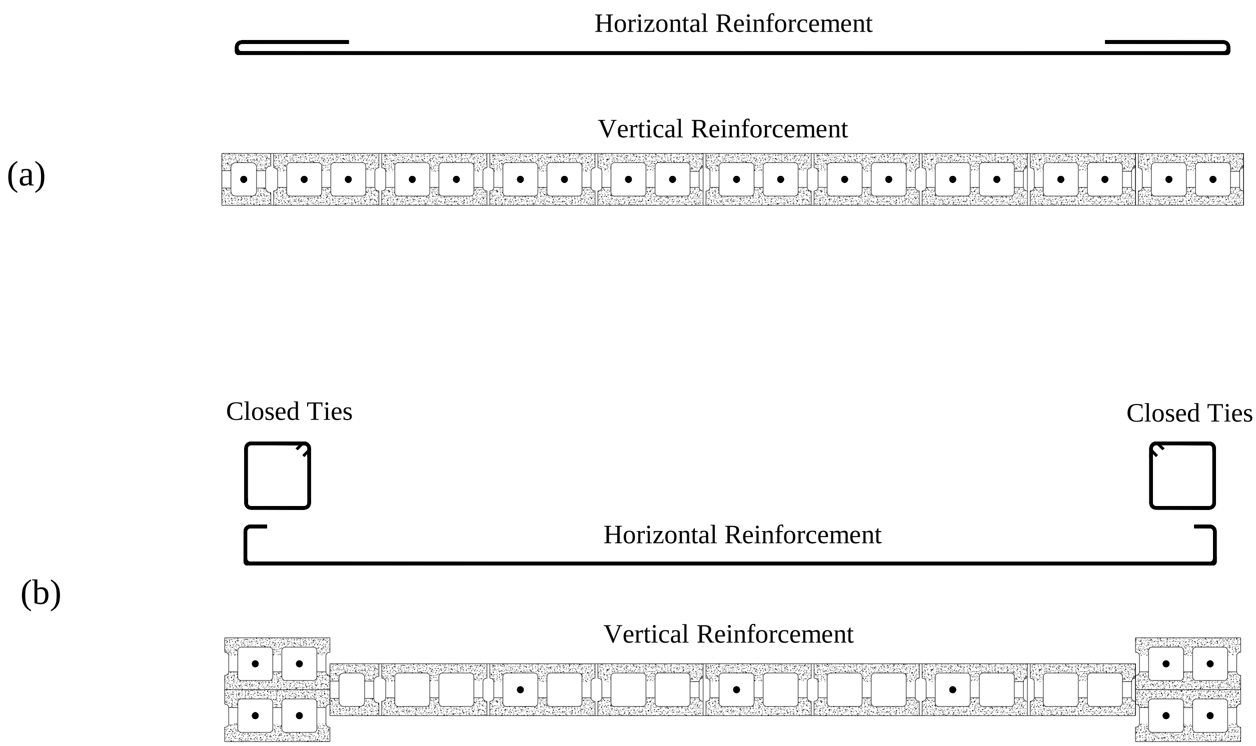

Fig. 1.1: Wall configurations: (a) Walls with rectangular cross section; (b) Wall with boundary elements.

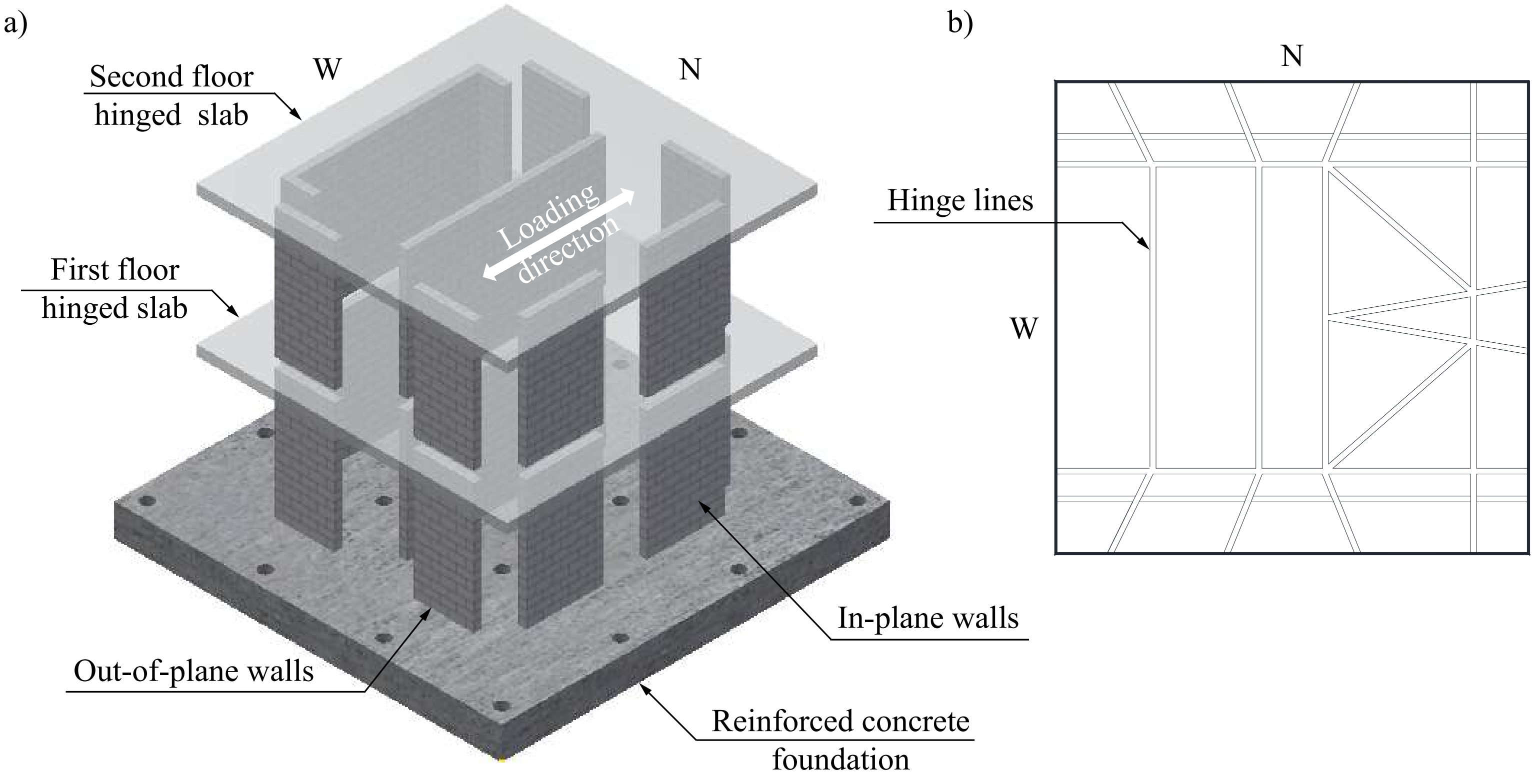

Fig. 1.2: *Building II* configuration; a) Isometric view from South - East direction; b) RC slab detailed with hinge lines (Heerema et al. 2015).

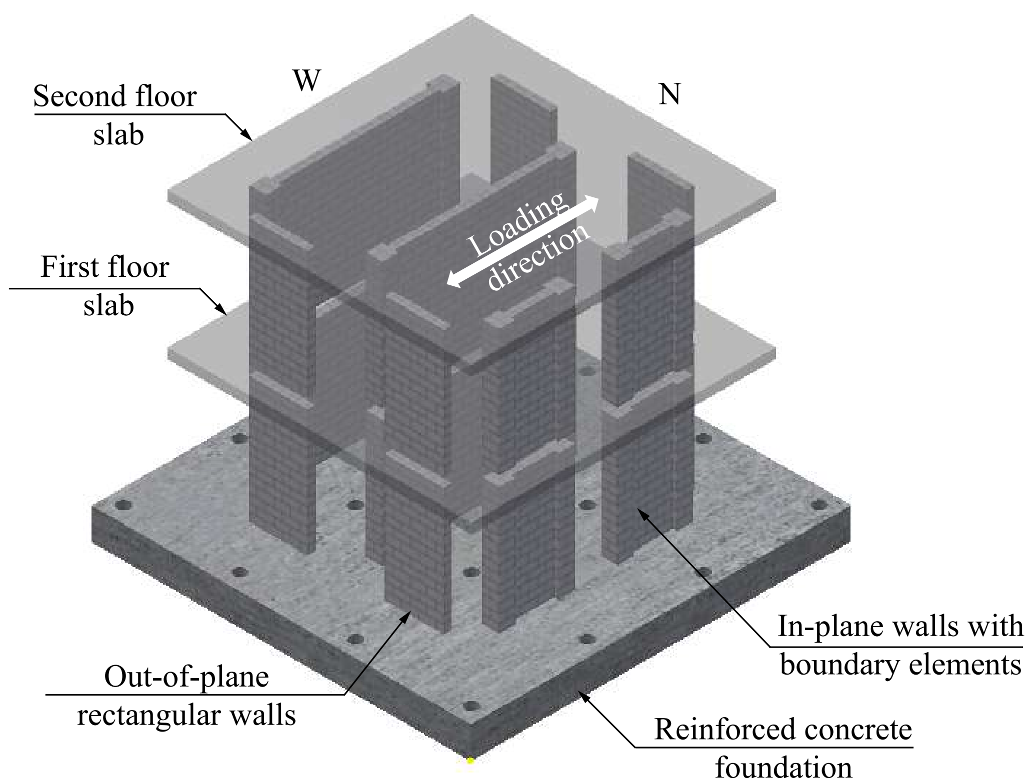

Fig. 1.3: Isometric view of *Building IV* from South - East direction.

CHAPTER 2
SEISMIC COLLAPSE RISK ASSESSMENT OF REINFORCED MASONRY WALLS WITH BOUNDARY ELEMENTS USING THE FEMA P695 METHODOLOGY

2.1 ABSTRACT

Using boundary elements in Reinforced Masonry (RM) walls allows closed ties to be used and multiple layers of vertical bars to be accommodated, thus providing a confining reinforcement cage. This enhances the overall performance of the RM wall with boundary elements relative to traditional RM walls with rectangular cross sections. This is attributed to the fact that traditional RM walls can typically only accommodate single-leg horizontal reinforcement and a single layer of vertical reinforcement because of practical limitations associated with concrete masonry unit geometrical configuration and construction techniques. Following the FEMA P695 methodology for Quantification of Building Seismic Performance Factors, the National Institute of Standards and Technology reported that some low-rise traditional rectangular RM walls (without boundary elements) might experience an excessive risk of collapse under the maximum considered earthquake (MCE). Moreover, although North American codes give seismic modification factors for RM shear walls with rectangular cross sections, no distinctive corresponding values are provided for RM shear walls with boundary elements. To address these issues, this chapter examines the effect of adopting the seismic response modification factors assigned for traditional RM shear walls on the collapse risk of RM shear walls with boundary elements. In this respect,

OpenSees was used to create macro models to simulate the seismic response of 20 RM shear walls with boundary elements, designed with different configurations under different gravity load levels. The modeling approach was experimentally validated and the models were subsequently used to perform nonlinear static pushover analyses and incremental dynamic analyses following the FEMA P695 methodology. The analyses focused on evaluating the wall overstrength, period-based ductility, and seismic collapse margin ratios under the MCE. The results show that RM walls with boundary elements designed considering the ASCE7-10 force reduction factor currently assigned to RM walls with rectangular cross sections experience an enhanced performance that is enough to meet the FEMA P695 acceptance criteria for the expected seismic collapse risk under the MCE.

2.2 INTRODUCTION

The concrete block unit configuration that is associated with traditional reinforced masonry (RM) shear walls with rectangular cross section, typically allows only for single leg of horizontal reinforcement and a single layer of vertical reinforcement to be used, as shown in Fig. 2.1(a). This arrangement provides no confinement at the wall toes, and it may lead to instability of the compression zone during cyclic loading. Conversely, the use of a boundary element in a RM wall allows a closed tie to replace the typical 180° hook formed by the horizontal shear reinforcement, as shown in Fig. 2.1(b). Boundary elements also accommodate multiple layers of vertical bars to create a reinforcement cage that confines the wall region subjected to high compressive stresses, and thus delays the buckling of the wall's vertical reinforcement. Relative to rectangular RM walls, this enables the compression reinforcement to remain effective up to much larger displacement demands after the concrete masonry unit face shell has spalled. In addition, the introduction of boundary elements in RM walls results in a reduced depth of the compression zone (neutral axis), which decreases the curvature at the yield (of the vertical reinforcement) and increases the ultimate curvature. This results in an increase of the curvature-, and subsequently, the displacement ductility capacities (Banting and El-Dakhakhni 2012). However, the decreased compression zone depth would also result in an increased demand on the tensile reinforcement strains; an aspect that should be accounted for during the wall design and reinforcement detailing.

Very little research has been carried out on the performance of RM walls with boundary elements under lateral load because early methods of confining masonry were similar to a conventional rectangular wall layout, with a single layer of vertical reinforcement. Different types of steel confinement reinforcement were proposed (e.g. closed wire mesh, seismic combs and Priestley plates) to improve the post-peak behavior of RM prisms (Hart et al. 1988). More recent work on confinement of unreinforced grouted concrete block used two types of welded wire mesh (Dhanasekar and Shrive 2002) to confine the grouted cells in unreinforced concrete block prisms. The wire mesh proved to be an effective means of increasing the peak compressive strength. However, the use of masonry boundary elements detailed as confined columns, which does not deviate from conventional pilasters construction practice, presents an attractive opportunity for practical application and formalized prescriptive design code requirements (Shedid et al. 2010 and Banting and El-Dakhakhni 2012).

Boundary elements allow for closed ties in every course through thickened wall ends, providing a confining reinforcing cage within the RM wall that delays both buckling of the vertical wall reinforcement and also crushing of the grout core. As a result, masonry face shell spalling in the compression toes does not cause an abrupt drop in resistance (Banting and El-Dakhakhni 2014). The same authors studied the compression behavior of confined boundary elements under displacement controlled loading and severe strength degradation was not observed. The increase of the confinement ratio had a significant effect on the post-peak behavior by softening the descending branch of the stress–strain curve after reaching the peak strength and providing more strain ductility (El Ezz et al. 2015).

For seismic design of different seismic force resisting systems, the ASCE/SEI 7-10 (ASCE 2010) provides a set of corresponding seismic response modification factors, such as the response modification factor (R), the system overstrength factor (Ω_o) and the deflection amplification factor (C_d). These modification factors are generally defined so that an increase in ductility is reflected by an increase in R that reduces the seismic force demands. Within ASCE/SEI 7-10 (ASCE 2010), values of R for *special* and *ordinary* RM shear wall systems (Masonry Standards Joint Committee (MSJC) 2013) are 5.0 and 2.0, respectively. These values were developed for RM shear walls with rectangular cross section, whereas RM walls with boundary elements are a newly proposed structural system. The Masonry Standards Joint Committee has not yet established reinforcement and detailing requirements for RM walls with boundary elements and has recommended that more testing is needed (MSJC 2013) to facilitate the development of prescriptive design requirements. As such, no distinctive R value is assigned in ASCE/SEI 7-10 (ASCE 2010) for RM walls with boundary elements to date.

A methodology to assess the suitability of seismic performance factors has been proposed in the FEMA P695 (FEMA 2009), Qualification of Building Seismic Performance Factors. This methodology uses collapse analyses to assess the adequacy of using specific sets of response parameters (R, C_d and Ω_o) for the corresponding seismic force-resisting system design The methodology considers uncertainties in ground motion, design, modelling and test data in the probabilistic assessment of collapse risk. The acceptance criteria are defined based on achieving specified minimum ratio between the median collapse intensity and intensity of the Maximum Considered Earthquake (MCE).

The objective of this chapter is to utilize the FEMA P695 (FEMA 2009) methodology to quantitatively evaluate the seismic collapse risk of RM shear walls with boundary elements when the performance factors assigned to traditional RM shear walls are adopted. In this respect, a simplified two-dimensional numerical model was developed using OpenSees (Open System of Earthquake Engineering Simulation, McKenna et al. 2000). Subsequently, data from experimental test programs were used to validate the proposed modelling technique. Following the model validation, nonlinear static pushover analyses and incremental dynamic analyses using the 44 ground motions, recommended by the FEMA P695 methodology, were performed on 20 RM shear walls with boundary elements archetypes. The analysis results were compared to the corresponding ones for traditional RM shear walls in terms of equivalent safety against collapse risk under the MCE.

2.3 MASONRY WALL MODEL

Extensive studies have been conducted to simulate the nonlinear behavior of RM shear walls. These studies can be categorized using two levels of refinement: (1) micro-modelling, where each component of the masonry wall is modelled individually, and (2) macro-modelling, where an equivalent material is used to model the masonry wall. Although micro-modelling can produce very accurate representation, it is computationally intensive because the relatively small dimensions of the comprising components require a very fine mesh. Conversely, macro-modelling is based on representing the overall structure with larger elements, each of which has properties that are equivalent to the sum of its components. This method does not require the level of detailed representation that is needed for micro-modelling. Macro-modelling has been used by researchers to simulate the behavior of masonry structures (e.g. Stavridis and Shing 2010 and Karapitta et al. 2011). However, the previous models still need a high level of detail that results in a high level of computational effort. Therefore, there is still a need to develop simpler models based on material and geometrical properties to simulate the overall behavior of RM wall systems.

2.3.1 Geometrical Model

In this chapter, OpenSees (McKenna et al. 2000) is used to create macro models of the in-plane response of RM walls with and without boundary elements. Figure 2.2 shows a schematic diagram of the wall model, including the distribution of nodes and elements. Five gauss integration points are used for each element. Also, all walls were assumed to have perfect base fixity and soil-structure interaction was neglected as per the NIST (2010) study. As can be seen in Fig. 2.2, the model uses displacement-based beam-column elements, which assume a linear curvature distribution and a constant axial strain. The beam-column elements are assigned fiber sections that model the reinforcement and masonry regions. However, the choice of element length is important when displacement-based beam-column elements are used with distributed plasticity and strain-softening material definitions (Ezzeldin et al. 2014). This is attributed to strain localization, in which the plastic deformation tends to concentrate in the first element above the base of the wall, while the adjacent elements remain elastic (Calabrese 2008). Therefore, the required element length was studied by comparing pushover analysis results to experimental results from cyclic testing taking the average of the load at peak displacement in each direction. Figure 2.3(a) compares experimental lateral load versus top displacement response of Wall W6 reported by Siyam et al. (2015) to the numerical pushover model with element lengths of $1.0\,L_w$, $0.5\,L_w$ and $0.2\,L_w$, where L_w is the wall length. As can be seen in Fig. 2.3(a), a large element length ($1.0\,L_w$) results in larger lateral load capacity of the wall and no strength degradation, whereas a small element length ($0.2\,L_w$) underestimates the lateral load capacity of the wall. The figure also shows that the load-displacement responses are well estimated when element length of ($0.5\,L_w$) is used. Figure 2.3(b) shows an example of the local behavior of the walls by comparing the peak compressive strain in masonry from the numerical model with that obtained from the experimental test. High strains are obtained using element length of $0.2\,L_w$, while the strains are underestimated using an element length of $1.0\,L_w$. It is also clear from Fig. 2.3(b) that using an element length of $0.5\,L_w$ results in matching the predicted strains with the corresponding experimental results, leading to a good estimation of the load-displacement response. However, using an element length of $0.5\,L_w$ is found to be only appropriate for Wall W6 and cannot be used for all the experimental RM shear walls used in this study to validate the model.

In general, the wall response can be well captured if the element length is a reasonable estimate of the plastic hinge length, L_p. Several formulae are available in the literature to estimate the plastic hinge length, L_p, of shear walls (e.g. Park and Paulay 1975; Paulay and Priestley 1992 and Priestley et al. 2007) However, none of these formulas provided good correlation with the experimental results of the RM shear walls considered in this study. For this purpose, the formula proposed by Bohl and Adebar (2011), which is based on nonlinear finite element analysis results of 22 isolated reinforced concrete shear walls, was found to give the best estimate of the plastic hinge length, L_p, for the RM shear walls with and without boundary elements (Ezzeldin et al. 2015a). The formula (Eq. 2.1) is a function of the wall length, L_w, the moment-shear ratio, Z, the gross area of wall cross section, A_g, the concrete compressive strength, $f_c^{'}$, and the axial compression, P:

$$L_p = (0.20L_w + 0.05Z)(1 - \frac{1.5P}{f'_c A_g}) \leq 0.80L_w \tag{2.1}$$

2.3.2 Material Model

All the material properties in the model were defined using the individual masonry material characteristics, without any calibration to the overall wall response. Figure 2.4 shows the material distribution through the cross-section area of the walls used in the model. Fiber sections are used to simulate the response of the RM walls. The cross-section is broken down into fibers where uniaxial materials are defined independently. Two uniaxial stress-strain relations were needed to model the behavior of the RM walls with rectangular cross sections:

one for the masonry and another for the reinforcing steel. Based on the cross-sectional area of each fiber and its position in the element cross section, the resultant internal forces at the section were calculated by numerical integration. The concrete masonry in this work was modelled using Chang and Mander's model for concrete (Chang and Mander 1994, Concrete07 in OpenSees). This model depends on the compressive strength, the strain at the maximum compressive strength, the elastic modulus and other parameters that define strength and stiffness degradation. A value of 0.003 was assigned to represent the strain at maximum compressive strength, ε_m, according to prism test data of Atkinson and Kingsley (1985). The elastic modulus, E_m, was calculated according to the MSJC (2013) code as 900 $f_m^{'}$, where $f_m^{'}$ is the masonry compressive strength. The strength and stiffness degradation parameters were taken according to the formulae reported in Chang and Mander (1994). The masonry parameters used in this chapter were validated using several experimental programs as will be discussed later.

Unlike traditional RM shear walls, RM walls with boundary elements have the vertical reinforcement near the extreme compression fiber confined by stirrups. Such confinement achieves a significant enhancement in both strength and ductility of the compressed masonry zone (boundary element region). This was taken into consideration within the numerical model by assigning different material properties to the confined masonry within the boundary element area. As such, the model by Mander et al. (1988) was used to calculate the compressive strength, f'_{mc}, and the strain at maximum compressive strength, ε_{mc}, within the boundary element confined area as shown in Fig. 2.4:

$$f'_{mc} = f'_{m}(1 + k_1 x') \tag{2.2}$$

$$\varepsilon_{mc} = \varepsilon_{m}(1 + k_2 x') \tag{2.3}$$

Where k_1, k_2 and x' are factors that depend on the vertical and horizontal reinforcement ratios in the boundary elements. Figure 2.4 also shows that the reinforcing steel was modelled using a Giuffre-Menegotto-Pinto model (Steel02 in OpenSees). The model was defined using the measured yield strength and strain hardening ratio for the model validation, whereas for the archetype structures, it was defined using a yield strength of 468 MPa and a strain hardening ratio of 1.20% based on NIST (2010). In all cases, the initial elastic modulus was 200 GPa and other constants that control the transition from elastic to plastic zone were R_0, CR_1 and CR_2, which were taken as 10, 0.925 and 0.15, respectively.

Buckling of longitudinal reinforcement is important in unconfined areas of RM shear walls, but cannot be simulated directly using Steel02 in OpenSees. Therefore, the fracture strain of the unconfined vertical bars was taken as 0.05 using the MinMax material option available in OpenSees, which is about 50% of the fracture strain that was measured in direct uniaxial tension tests (Rodriguez et al. 1999, Zong and Kunnath 2008). These studies reported that the actual fracture strain of the bar is influenced by low-cycle fatigue, which causes the bar to kink. For confined bars, the fracture strain was taken as 0.1 based on NIST (2010). In addition, strain penetration was modelled by using a zero-length element at the base, as shown in Fig. 2.2, where the vertical reinforcement was represented using the Bond_SP01 material in OpenSees. The total bar slip due to strain penetration is calculated in this model as a function of bar stress (Zhao and Sritharan 2007).

Finally, shear behavior was modelled using the Pinching4 material model in OpenSees with the section aggregator option to include this shear behavior of the wall with the flexural behavior of the fiber section. In this respect, three points are needed to define the response envelope of Pinching4 material. These points were defined as recommended by Waugh and Sritharan (2010). The lateral force corresponding to the first flexural cracking and the uncracked shear stiffness were used to define the first point. In addition, the lateral force causing flexural yielding of the vertical reinforcement and the effective shear stiffness (20% of the uncracked stiffness) were selected to define the second point. Finally, the third point was defined using the ultimate lateral force and the post-yield shear stiffness (1% of the effective shear stiffness).

2.3.3 Model Validation

The numerical models of RM shear walls without and with boundary elements were validated against the experimental results of Siyam et al. (2015), Shedid et al. (2008), Shedid et al. (2010) and Banting and El-Dakhakhni (2014). These experimental programs were selected because they include walls of both types with a range of aspect ratios, from 1.5 to 4.6. For the wall model, the axial loads were held constant and reversed cyclic horizontal displacements were applied at the top of the wall using the same loading protocol as the experimental tests. Table 2.1 summarizes the RM wall dimensions, vertical and horizontal reinforcement ratios, masonry compressive strength, reinforcement yield strength and aspect ratios for all the walls that were used to validate the model.

Figures 2.5(a and b) compare the numerical model predictions with the experimental results for specimens W6 and W5 that were tested by Siyam et al. (2015). These walls were one-third-scale fully-grouted rectangular RM shear walls with a height of 2.16 m and lengths of 0.46 m and 0.59 m, respectively. The figures show the good agreement between the experimental hysteresis loops and the corresponding loops from the cyclic analyses using OpenSees. The model is able to simulate most relevant characteristics of the cyclic response, including the initial stiffness, peak load, stiffness degradation, strength deterioration, hysteretic shape and pinching behavior at different drift levels. These ranges cover almost the entire portion of the load-displacement curve up to 80% strength degradation. The lateral capacity of the wall is predicted very closely for most of the lateral drift levels, with a maximum error in the lateral load prediction of less than 15%. In addition, the numerical model captures the variation of stiffness with increased displacement to within a maximum error of 11%. The increase of energy dissipation and equivalent viscous damping with loading is also represented well by the numerical model, with maximum errors of 12% and 11%, respectively (Ezzeldin et al. 2014).

To verify the robustness of the developed numerical model for walls with boundary elements with the configuration shown in Fig. 2.1(b), experimental results from two half-scale RM shear walls were used. The first wall was specimen W3 from Shedid et al. (2010), which had a length of 1.80 m and a height of 3.99 m. The second was specimen W1 reported by Banting and El-Dakhakhni (2014), which had a length of 2.65 m and a height of 3.99 m. The results of the experimental and numerical models are compared in Figs. 2.5(c and d), respectively. Relative to the experimental results, the maximum error in the lateral load in either push or pull direction is less than 9% and 12% in Walls W3 and W1, respectively. In addition, the maximum difference between numerical and experimental effective stiffness at any level of drift ratios is less than 8 % and 13% for Walls W3 and W1, respectively. Moreover, the model captures the increase of equivalent viscous damping with loading with a maximum error of approximately 18% and 16% for Walls W3 and W1, respectively. The error in equivalent viscous damping is more than the error in energy dissipation because the model overestimates the energy dissipation, E_d, in some of the same cycles that it underestimates the elastic strain energy, E_s (Ezzeldin et al. 2015b). Overall, however, this level of agreement between the experimental and numerical results is considered to be very good in terms of RM shear wall response predictions.

2.3.4 Collapse Criteria

For the analyses in this chapter, collapse was defined following the GCR 10-917-8 (NIST 2010) study as the point when the wall reaches either of the following two conditions:

1- Masonry crushing: Crushing was considered to occur when 30% of the cross-section reached the crushing strain. For unconfined areas, the crushing strain was taken as 0.01, which represents the strain at the end of the descending branch of the typical masonry stress-strain relation (NIST 2010). For confined areas, the crushing strain was defined as the strain at the end of the descending branch of confined masonry stress-strain relation according to Mander et al. (1988).

2- Steel Rupture or buckling: Fracture of reinforcement was defined as when 30% or more of the bars in the wall cross-section reached the failure strain. The fracture strain was taken as 0.05 and 0.1 for unconfined and confined bars, respectively (NIST 2010).

2.4 STRUCTURAL ARCHETYPE

2.4.1 RM Shear Wall Configurations

This chapter adopted the same buildings that the National Institute of Standards and Technology (NIST 2010) used in their study GCR 10-917-8 to investigate the FEMA P-695 (FEMA 2009) methodology. That study evaluated 20 fully grouted rectangular shear walls for a range of building heights and design parameters to cover a wide design space. Walls representing RM buildings for retail occupancies were designed for the one-story configurations, while other walls representing RM buildings for hotels and residential occupancies were designed with 2, 4, 8 and 12 stories. The detailed plan configurations and dimensions are provided in Appendix A of the GCR 10-917-8 (NIST 2010) study.

To facilitate direct comparison of the response of walls with and without boundary elements, the same 20 walls were redesigned with boundary elements but using the same seismic performance factors (R, C_d and Ω_o). Table 2.2 summarizes the RM wall dimensions, aspect ratios and reinforcement details of the first floor for all the 20 archetypes (S1-B to S20-B). The boundary elements at the wall ends were selected to be 40.64 cm (16 inch) in both wall in-plane and out-of-plane directions. These dimensions were chosen based on using two standard concrete masonry units to form the boundary elements. The unconfined masonry compressive strength, f'_m, varied from one archetype to another in the previous study (NIST 2010), so the same values were used to design and model each corresponding archetype with boundary elements in this chapter. As can be seen in Table 2.2, four vertical reinforcement bars were placed in two layers and confined with steel reinforcement ties in every course through thickened wall ends. Ties were located at the same level as the horizontal reinforcement of the walls for ease of construction using #3 bars with an area of 71 mm^2 each. Archetypes were separated in NIST (2010) into eight groups with common gravity loads, number of stories, and seismic design category (SDC). Table 2.3

shows that the 20 RM walls with boundary elements were divided into the same eight performance groups. The table also indicates that the archetypes cover a wide range of RM wall systems with variation of the axial load (low and high) and the SDC (D_{min} and D_{max}). Although a minimum of three archetypes are required in each performance group according to the full application of the FEMA P695 (2009) methodology, the same number of archetypes was used in this chapter as in the GCR 10-917-8 (NIST 2010) study to facilitate direct comparison.

2.4.2 Design Requirements

According to the MSJC (2013), special RM Shear walls are required for SDC D. The RM shear walls with boundary elements were designed and detailed in accordance with the requirements of MSJC (2013). The system design requirements of ASCE/SEI 7-10 (ASCE 2010), including minimum base shear and story drift limits, were used as the basis for design, with the exception that C_d was taken equal to R, as specified in the FEMA P-695 (FEMA 2009) methodology. The force reduction factor, R, was taken as 5.0 for the RM shear walls.

Table 2.4 presents the seismic design parameters of the RM shear walls with boundary elements, including: the seismic base shear coefficient, V/W (where V is the base shear and W is the seismic weight); MCE spectral acceleration, S_{MT}; the code-defined estimate of the fundamental period, T; and the fundamental period of the numerical model, T_1. ASCE/SEI 7-10 (ASCE 2010) states that T shall not exceed the product of the coefficient for the upper limit on the calculated period, C_u, and the approximate fundamental period, T_a. The fundamental period, T, was calculated in this study as $C_u T_a$, but subject to the lower bound value of 0.25s as recommended in FEMA P695 (FEMA 2009). The code estimates of fundamental period, T, for walls with boundary elements were taken to be the same as in the GCR 10-917-8 (NIST 2010) study because the formula used is independent of the shape of the wall. The calculated values of T_1 were based on the modulus of elasticity given by MSJC (2013) and taking the effective moment of inertia, I_e, as 50% of the uncracked section of masonry shear wall. The T_1 values for walls with boundary elements were within 10% of the values for rectangular walls.

2.5 NONLINEAR RESPONSE ANALYSES

Nonlinear static pushover analyses and Incremental Dynamic Analyses (IDA) were performed on all archetypes. For all analyses, 1.05 times the specified dead load, D, was applied together with 0.25 times the specified live load, L, as recommended in FEMA P695 (FEMA 2009).

2.5.1 Static Pushover Analyses

For each wall, a pushover analysis was performed, using the design distribution of lateral forces from ASCE/SEI 7-10 (ASCE 2010), to compute the overstrength factor, W, and period-based ductility, μ_T. The overstrength factor, W, is defined (Eq. 2.4) as the ratio of the maximum base shear, $V_{\max}$, to the design base shear, V:

$$\mathrm{W} = \frac{V_{\max}}{V} \tag{2.4}$$

The period-based ductility, μ_T, is defined (Eq. 2.5) as the ultimate roof drift, δ_u, corresponding to a 20% reduction in base shear, divided by the effective yield drift at the roof, $\delta_{y,eff}$, calculated according to Eq. 2.6 where C_o is a modification factor to relate the spectral displacement of an equivalent single-degree-of-freedom (SDOF) system to the roof displacement of the building multi-degree-of-freedom (MDOF) system calculated according to ASCE/SEI 41-06 (ASCE 2007), W is the building weight, $V_{\max}$ is the maximum base shear determined from the pushover curve and g is the acceleration due to gravity.

$$\mu_T = \frac{\delta_u}{\delta_{y,eff}} \tag{2.5}$$

$$\delta_{y,eff} = C_o \frac{V_{\max}}{W} \frac{g}{4\pi^2} \max(T, T_1)^2 \tag{2.6}$$

Figure 2.6 presents example pushover curves for walls with and without boundary elements for archetypes S2, S5, S13 and S15. As can be seen in Fig. 2.6, the stiffness up to yielding are almost identical for walls with and without boundary elements, but boundary elements increase the ultimate displacement capacities by up to 80% relative to walls without boundary elements. This is because boundary elements decrease the curvature at the onset of yield of the vertical reinforcement and increase the curvature at ultimate conditions, which in turn increase the ductility relative to the corresponding walls without boundary elements. Figure 2.6 also shows that whether or not boundary elements were used, walls subjected to high axial load (S2 and S5) were less ductile than walls subjected to low axial load (S13 and S15) and high-rise walls (S5 and S15) were more ductile than low-rise walls (S2 and S13). For low-rise walls, the periods that were estimated during design, T, were much greater than the modelled periods, T_1, leading to high effective yield drifts, $\delta_{y,eff}$, and therefore low period-based ductility, μ_T.

2.5.2 Ground Motion Selection

Each archetype was analyzed using the set of 44 far-field ground motion records (22 pairs of horizontal components) provided as part of the FEMA P695 (FEMA 2009) methodology. The ground motion records are normalized by their respective peak ground velocity to remove unwarranted variability, and the records are scaled so that the median value of the records matches the MCE at the fundamental period, T (FEMA 2009). Figure 2.7 compares the response spectra of the 44 normalized ground motions to the design spectra of SDC D_{max} and SDC D_{min}.

2.5.3 Dynamic Analyses

The FEMA P695 procedure for conducting nonlinear dynamic analyses is based on the concept of IDA (Vamvatsikos and Cornell 2002), in which each ground motion is scaled to increasing intensities until the structure reaches a collapse point. Based on NIST (2010), Rayleigh damping proportional to initial stiffness of 5% was assigned at the periods of the first and third modes for all archetypes, except for those with two stories or fewer, where T_1 and $0.2T_1$ were used instead. Figure 2.8 shows example of IDA results for four different archetypes (S2-B, S5-B, S1-B and S15-B). Each point in each IDA curve represents a single nonlinear dynamic analysis of one archetype model subjected to one ground motion record scaled to one intensity level. The differences in the response of each archetype model, when subjected to different ground motions with different frequency characteristics, are shown from the scatter of the story drift ratios in Fig. 2.8.

For each archetype, the median collapse spectral intensity, S_{CT}, was determined as the spectral acceleration when 50% of the ground motions cause the structure to collapse. For each record, the maximum considered earthquake spectral acceleration, S_{MT}, corresponding to the fundamental period of the archetype, T, was also determined. Although the IDAs of RM shear walls without boundary elements in the GCR 10-917-8 (NIST 2010) study (from S1 to S20) were stopped when 22 ground motions indicated collapse, the IDAs in this chapter were completely performed to all the 44 ground motions for each RM shear wall with boundary elements (from S1-B to S20-B) in order to draw complete collapse fragility curves for all walls. According to the methodology, the collapse safety of the structure is characterized by calculating the Collapse Margin Ratio (CMR):

$$CMR = \frac{S_{CT}}{S_{MT}} \tag{2.7}$$

Values of overstrength, Ω, from the pushover analyses, and collapse margin ratio, CMR, calculated from Eq. 2.7 for all archetypes with and without boundary elements, are summarized in Table 2.5 for archetypes S1 to S10 and Table 2.6 for archetypes S11 to S20. To verify the robustness of the model used in this chapter for different aspect ratios, three of the archetypes reported in the GCR 10-917-8 (NIST 2010) study, S1, S2 and S5, were modelled independently as part of this chapter. The aspect ratios of the three walls were 0.5, 0.63 and 3.75. The CMR of the three walls, shown in Table 2.5, are similar to the values obtained in the GCR 10-917-8 (NIST 2010) study, which confirms that the numerical approach used here was consistent with the previous work. Therefore, the other archetypes were not reanalyzed. Instead, the CMR values that were reported in the GCR 10-917-8 (NIST 2010) study were used for comparison with the results of this chapter on walls with boundary elements.

Using collapse data from the IDA results, a collapse fragility curve can be defined through a cumulative distribution function (CDF) that relates the ground motion intensity to the probability of collapse. Figure 2.9 compares the collapse fragility curves drawn for four walls without boundary elements (S2, S5, S13 and S15) to the fragility curves for walls with boundary elements (S2-B, S5-B, S13-B and S15-B). Although the full IDA results are available, the curves are based on the median value with the assumed variability that is given by FEMA P695 (FEMA 2009). It is clear from Fig. 2.9 that the assumed variability was generally similar to the actual cumulative distribution function data, except for archetype S15. For all four archetypes shown in Fig. 2.9, the walls with boundary elements have a much greater collapse spectral intensity, S_{CT}, than the corresponding rectangular walls. This is because the larger ultimate curvature of walls with boundary elements delays the collapse of these walls and thus has the potential to reduce the risk of collapse under high seismic loads.

2.6 COLLAPSE RISK ASSESSMENT

According to the FEMA P695 (FEMA 2009) methodology, the Adjusted Collapse Margin Ratio ($ACMR$) is computed as the product of the spectral shape factor, SSF, and the CMR obtained from the IDA results. The SSF values are given as a table in FEMA P695 (FEMA 2009) and depend on the fundamental period, T, and the period-based ductility, μ_T, obtained from pushover analyses. The calculated values of the $ACMR$, as shown in Tables 2.7 and 2.8, are then compared with acceptable values, which are defined in terms of the total system uncertainty, β_{TOT}, which is calculated as per the methodology as:

$$\beta_{TOT} = \sqrt{\beta^2{}_{RTR} + \beta^2{}_{DR} + \beta^2{}_{TD} + \beta^2{}_{MDL}} \tag{2.8}$$

In this equation, β_{RTR} is the record-to-record uncertainty due to variations in frequency content and dynamic characteristics of the various records, as well as variability in the hazard characterization as reflected in the ground motion records. A value of 0.4 is assigned for systems with a period-based ductility greater than or equal to 3.0 (FEMA 2009). The second term, β_{DR}, accounts for the completeness and robustness of the design requirements, and the extent to which they provide safeguards against unanticipated failure modes. These design requirements are categorized as "B-Good" (β_{DR}=0.2) because special RM shear walls are considered well developed and reasonably substantiated by experimental data (NIST 2010). The third term, β_{TD}, describes the completeness and robustness of the test data used to define the system. The test data used in this chapter cover a wide range of RM shear wall parameters, but they do not cover the full range of reinforcement ratios, wall aspect ratios, and axial load levels. Based on these observations, this test data set is categorized as "B-Good" (β_{TD}=0.2) (NIST 2010). Finally, the uncertainty of numerical models is considered through factor β_{MDL}. Model uncertainty is based on how well the analysis models capture structural collapse behavior through direct simulation or non-simulated failure modes. Numerical models for RM shear walls without and with boundary elements were assigned a quality rating of "B-Good" (β_{MDL}=0.2) because model validation demonstrated that behavior of RM walls with or without boundary elements can be simulated using numerical models (NIST 2010).

Based on these values, β_{TOT} was calculated according to Eq. 2.8 as 0.525. Although RM shear walls with boundary elements are a new proposed system relative to the traditional rectangular walls, β_{TOT} was kept constant for both types. This assumption is considered acceptable as construction practice of RM walls with boundary elements does not deviate significantly from that of traditional RM walls. The FEMA P695 methodology assesses the seismic collapse risk through defining two acceptable $ACMR$ values in terms of the total system uncertainty, β_{TOT}. First, the acceptable $ACMR_{20\%}$ is defined as 1.56 to ensure a probability of collapse less than 20% for each index archetype within a performance group. Second, FEMA P695 defines the acceptable $ACMR_{10\%}$ as 1.96 to ensure a probability of collapse less than 10% on average across a performance group. Both criteria must be achieved to pass the performance evaluation as per the methodology.

Tables 2.7 and 2.8 compare the $ACMR$ with the acceptable $ACMR$ for the all archetypes for both systems (RM shear walls with and without boundary elements). Special RM shear walls without boundary elements do not fully meet the acceptance criteria of the methodology. However, RM shear walls with boundary elements, which were designed for the same lateral load as RM shear walls without boundary elements, passed the acceptance criteria of the methodology with a significant margin. As can be seen in Tables 2.7 and 2.8, the $ACMR$ values, calculated for all archetypes with boundary elements (S1-B to S20-B), satisfy the acceptable $ACMR$ limits. This is because using stirrups for confinement increases the ultimate strain of the RM in the boundary region, increasing the ductility capacity and leading to much higher $ACMR$. Also, Tables 2.7 and 2.8 show that there is a wide difference in the ductility capacity between low-rise (1-4 stories) and high-rise walls (8-12 stories) subjected to earthquake ground motion regardless of the type of the system. However, ASCE/SEI 7-10 (ASCE 2010) assigns a single R factor for all RM shear walls regardless of their aspect ratios. The CMRs in Tables 2.7 and 2.8 show that the current R factor assigned to rectangular low-rise walls is too large to meet the acceptance criteria of the methodology, but the addition of boundary elements enables low-rise walls to pass the methodology through higher $ACMR$ values relative to the acceptable $ACMR$ limits. For high-rise walls (8-12 stories), walls without boundary elements that are designed with the current R factor satisfy the methodology, but the results suggest that R could be increased if boundary elements are used. Finally, the system overstrength factor, Ω_o, is taken as the largest average value of the mean overstrength factor calculated for each performance group (FEMA 2009). Tables 2.7 and 2.8 show that the system overstrength factor, Ω_o, for RM shear walls without and with boundary elements are 2.12 and 2.61, respectively. The value provided in ASCE/SEI 7-10 (ASCE 2010) is 2.5, which is conservative for rectangular walls and within 5% of the calculated value for walls with boundary elements.

2.7 CONCLUSIONS

This chapter evaluated the collapse risk of RM shear walls with boundary elements under the MCE when the seismic performance factors that are currently assigned to rectangular RM shear walls are adopted. In this respect, 20 archetypes of RM shear walls with boundary elements were evaluated using the FEMA P695 (FEMA 2009) methodology utilizing a two-dimensional model developed using OpenSees. The experimentally validated model satisfies the methodology requirements in terms of simulating stiffness, strength, and inelastic deformation under reversed cyclic loading. Finally, nonlinear pushover analyses and incremental dynamic analyses were performed to evaluate the overstrength, Ω, period-based ductility, μ_T, and collapse capacity, S_{CT}, for all walls.

The GCR 10-917-8 (NIST 2010) study found that RM shear walls with rectangular cross sections that were designed using R =5.0 did not fully meet the acceptance criteria of the methodology: the one- and two-story archetypes both had a collapse margin ratio that did not limit the probability of collapse under a maximum considered earthquake to less than 20%. Where previous results had suggested that the R factor currently assigned to rectangular low-rise walls is too large to meet the acceptance criteria of the methodology, the results presented here suggested that adding boundary elements enables low-rise walls to pass the methodology by achieving higher collapse margin ratios (i.e. lower collapse risk in an earthquake). Considering structures with more than two stories, walls without boundary elements that are designed with the current R factor satisfy the acceptance criteria of the methodology, but the results suggest that R could be increased if boundary elements are used. The system overstrength factor, Ω_o, is conservative for rectangular walls and within 5% of the calculated value for walls with boundary elements.

The analyses in this chapter were limited to individual RM shear walls with a specific configuration of boundary elements because of a lack of experimental data for other wall systems, such as coupled shear walls or walls with openings. In addition, the reliability of the numerical model was shown to depend on the assumed plastic hinge length. Additional experimental tests are still needed to validate the numerical models for other wall systems to fill the gap between the practical design and current code provisions.

2.8 ACKNOWLEDGMENTS

The financial support for this project was provided through the Natural Sciences and Engineering Research Council of Canada (NSERC) and the Canada Masonry Design Centre (CMDC). Support was also provided by the McMaster University Centre for Effective Design of Structures, funded through the Ontario Research and Development Challenge Fund of the Ministry of Research and Innovation.

2.9 NOTATION

The following symbols are used in this chapter:

A_g	=	Gross section-area of wall;
C_d	=	Deflection amplification factor;
C_0	=	Modification factor to relate spectral displacement of SDOF system to roof displacement of building in MDOF system;
C_u	=	Coefficient for upper limit on calculated period;
D	=	Dead Load;
D_{max}	=	Maximum spectral acceleration intensity of SDC D;
D_{min}	=	Minimum spectral acceleration intensity of SDC D;
E_d	=	Energy dissipation at certain cycle;
E_m	=	Masonry modulus of elasticity;
E_s	=	Elastic strain energy;
$f'c$	=	Concrete compressive strength;
f'_m	=	Unconfined masonry compressive strength;
f'_{mc}	=	Confined masonry compressive strength;
f'_y	=	Reinforcement yield strength;
g	=	gravity acceleration;
K_1	=	Coefficient that function in concrete mix and lateral pressure ;
K_2	=	Coefficient that function in K_1;
L	=	Live load;
L_w	=	Length of wall;
P	=	Axial load;
R	=	Response modification factor;
S_{CT}	=	Median collapse intensity of ground motions records;
S_{MT}	=	Intensity at MCE ground motion;
T	=	Code fundamental period;
T_a	=	Approximate fundamental period;
T_1	=	Fundamental period based on eigenvalue analysis;
x'	=	Coefficient that function in horizontal reinforcement ratio;
V	=	Design base shear of wall;
V_{max}	=	Maximum base shear calculated from pushover analysis;
W	=	Seismic effective weight of wall;
β_{DR}	=	Design requirements uncertainty;
B_{MDL}	=	Analytical or numerical model uncertainty;
B_{RTR}	=	Record-to-record uncertainty;
B_{TD}	=	Test data uncertainty;
B_{TOT}	=	Total system uncertainty;
δ_u	=	Ultimate roof drift;

$\delta_{y,eff}$	=	Effective yield roof drift;
ε_m	=	Strain at maximum compressive strength of unconfined masonry;
ε_{mc}	=	Strain at maximum compressive strength of confined masonry;
ρ_v	=	Vertical reinforcement ratio;
ρ_h	=	Horizontal reinforcement ratio;
μ_T	=	Period-based ductility;
Ω	=	Overstrength factor; and
Ω_o	=	System overstrength factor.

2.10 REFERENCES

ASCE/SEI (Structural Engineering Institute). (2010). "Minimum design loads for buildings and other structures." *ASCE/SEI 7-10*, Reston, VA.

ASCE. (2007). "Seismic rehabilitation of existing buildings." *41-06*, Reston, VA.

Atkinson, R.H., and Kingsley, G.R. (1985). "A Comparison of the Behaviour of Clay and Concrete Masonry in Compression." Report No. 1.1-1, *US-Japan Coordinated Program for Masonry Building Research*, Atkinson-Noland & Associates, Boulder, Colorado.

Banting, B. and El-Dakhakhni, W. (2012). "Force-and displacement-based seismic performance parameters for reinforced masonry structural walls with boundary elements." *J. Struct. Eng*., 10.1061/(ASCE)ST.1943-541X.0000572, 1477–1491.

Banting, B. and El-Dakhakhni, W. (2014). "Seismic performance quantification of reinforced masonry structural walls with boundary elements." *J. Struct. Eng*., 10.1061/(ASCE) ST.1943-541X.0000895, 04014001.

Bohl, A., and Adebar, P. (2011). "Plastic hinge lengths in high-rise concrete shear walls." *ACI Struct. J*., 108(2), 148-157.

Calabrese, A. (2008). "Numerical issues in distributed inelasticity modelling of RC Frame elements for seismic analysis." Master's thesis, Istituto Universitario di Studi Superiori di Pavia, Università degli Studi di Pavia, Pavia, Italy.

Chang, G.A. and Mander, J.B. (1994). "Seismic energy based fatigue damage analysis of bridge columns: Part 1 – evaluation of seismic capacity." *NCEER Technical Report* No. NCEER-94-0006 State University of New York, Buffalo, N.Y.

Dhanasekar, M., and Shrive, N., G. (2002). "Strength and deformation of confined and unconfined grouted masonry." *ACI Struct. J.*, 99(6), 819-826.

El Ezz, A. A., Seif Eldin, H. M., and Galal, K. (2015). "Influence of confinement reinforcement on the compression stress–strain of grouted reinforced concrete block masonry boundary elements". *Structures*, 2, 32-43, Elsevier.

Ezzeldin, M., Wiebe, L., Shedid, M., and El-Dakhakhni, W. (2014). "Numerical modelling of reinforced concrete block structural walls under seismic loading." *9th Int. Masonry Conf.*, International Masonry Society, Surrey, UK.

Ezzeldin, M., Wiebe, L., and El-Dakhakhni, W. (2015a). "Seismic performance assessment of reinforced masonry walls with and without boundary elements using the FEMA P695 methodology." *12th North American Masonry Conf.*, Masonry Society, Longmont, USA.

Ezzeldin, M., Wiebe, L., and El-Dakhakhni, W. (2015b). "Numerical modelling of reinforced concrete block structural walls with boundary elements under seismic loading." *11th Canadian Conf. on Earthquake Engineering*, Canadian Association for Earthquake Engineering, Victoria, Canada.

FEMA. (2009). "Quantification of building seismic performance factors." *FEMA P695*, Washington, DC.

Hart, G. C., Noland, J. L., Kingsley, G. R., Englekirk, R. E., and Sajjad, N. A. (1988). “The use of confinement steel to increase the ductility in reinforced masonry shear walls.” *Masonry Soc. J.*, 7(2), 19-42.

Karapitta, L., Mouzakis, H., and Carydis, P. (2011). "Explicit finite-element analysis for the in-plane cyclic behaviour of unreinforced masonry structures." *Earthquake Eng. Struct. Dyn*., 40(2), 175-193.

Mander, J. B., Priestley, M. J. N. and Park, R. (1988). “Theoretical stress-strain model for confined concrete.” *J. Struct. Eng*., 114(8), 1804–1826.

MSJC (Masonry Standards Joint Committee). (2013). “Building code requirements for masonry structures.” *TMS 402-13/ASCE 5-13/ACI 530-13*, ASCE, Reston, VA.

McKenna, F., Fenves, G. L., and Scott, M. H. (2000). *Open system for earthquake engineering simulation*, Univ. of California, Berkeley, Calif., http://opensees.berkeley.edu.

NIST. (2010). “Evaluation of the FEMA P695 methodology for quantification of building seismic performance factors.” *NIST GCR 10-917-8*, Gaithersburg, MD.

Park, R., and Paulay, R. (1975). *Reinforced concrete structures*, Wiley, New York.

Paulay, T., and Priestley, M. (1992). *Seismic design of reinforced concrete and masonry buildings*, Wiley, New York.

Priestley, N., Calvi, G., and Kowalsky, M. (2007). *Displacement-based seismic* *design of structures*, Istituto Universitario di Studi Superiori (IUSS), Pavia, Italy.

Rodriguez, M. E., Botero, J. C., and Villa, J. (1999). "Cyclic stress-strain behaviour of reinforcing steel including effect of buckling." *J. Struct. Eng.*, 10.1061/(ASCE)0733-9445(1999)125:6(605), 605–612.

Shedid, M., Drysdale, R., and El-Dakhakhni, W. (2008). "Behaviour of fully grouted reinforced concrete masonry shear walls failing in flexure: Experimental results." *J. Struct. Eng.*, 134(11), 1754–1767.

Shedid, M. T., El-Dakhakhni, W. W. and Drysdale, R. G. (2010). "Alternative strategies to enhance the seismic performance of reinforced concrete-block shear wall systems." *J. Struct. Eng.*, 136(6), 676-689.

Siyam, M., El-Dakhakhni, W., Shedid, M., and Drysdale, R. (2015). "Seismic response evaluation of ductile reinforced concrete block structural walls. I: experimental results and force-based design parameters." *J. Perform. Constr. Facil.* , 10.1061/(ASCE)CF.1943-5509.0000794, 04015066.

Stavridis, A., and Shing, P. B. (2010). "Finite-element modeling of nonlinear behaviour of masonry-infilled RC frames." *J. Struct. Eng.*, (136)3, 285-296.

Vamvatsikos, D., and Cornell, A. (2002). "Incremental dynamic analysis." *Earthq. Eng. Struct. Dyn.*, 31(3), 491–514.

Waugh, J., and Sritharan, S. (2010) "Lessons Learned from Seismic Analysis of a Seven-Story Concrete Test Building." *Journal of Earthquake Engineering*, (14)3, 448-469.

Zhao, J., and Sritharan, S. (2007). "Modeling of strain penetration effects in fiber-based analysis of reinforced concrete structures." *ACI Struct. J.*, 104(2), 133–141.

Zong, Z., and Kunnath, S. (2008). "Buckling of reinforcing bars in concrete structures under seismic loads." *14th World Conf. on Earthquake Engineering*, International Association for Earthquake Engineering, Tokyo, Japan.

Table 2.1 Characteristics of the RM Walls used for the Model Validation.

Wall ID Number	Height (m)	Length (m)	Vertical Reinforcement ρ_v (%)	Horizontal Reinforcement ρ_h (%)	f'_m (MPa)	f_y (MPa)	Aspect Ratio
Wall-W6[a]	2.16	0.46	0.60	0.26	19.30	495	4.60
Wall-W5[a]	2.16	0.59	0.60	0.26	19.30	495	3.60
Wall-W3[b]	3.99	1.80	0.55	0.30	16.40	495	2.21
Wall-W1[c]	3.99	2.65	0.51	0.30	14.90	496	1.50

[a] Based on data from Siyam et al. (2015)

[b] Based on data from Shedid et al. (2010)

[c] Based on data from Banting and El-Dakhakhni (2014)

Table 2.2 Dimensions and Reinforcement Details of RM Walls with Boundary Elements.

Archetype Design ID Number	Height (m)	Length (m)	Vertical Reinforcement	ρ_v %	Horizontal Reinforcement	ρ_h %	Aspect Ratio
S1-B	3.65	7.31	8 # 3 + 6 # 4	0.083	# 5 @ 1220 mm	0.085	0.50
S2-B	6.09	9.75	8 # 3 + 8 # 4	0.076	# 6 @ 800 mm	0.180	0.62
S3-B	12.19	9.75	8 # 3 + 8 # 4	0.076	# 5 @ 800 mm	0.127	1.25
S4-B	24.38	9.75	8 # 4 + 8 # 5	0.125	# 4 @ 800 mm	0.082	2.50
S5-B	36.57	9.75	8 # 5 + 16 # 5	0.152	2 x #4 @ 800 mm	0.107	3.75
S6-B	3.65	7.31	8 # 3 + 8 # 4	0.100	# 5 @ 1220 mm	0.085	0.50
S7-B	6.09	9.75	8 # 3 + 8 # 4	0.076	# 5 @ 800 mm	0.127	0.62
S8-B	12.19	9.75	8 # 3 + 8 # 4	0.076	# 5 @ 800 mm	0.127	1.25
S9-B	24.38	9.75	8 # 3 + 8 # 4	0.076	# 5 @ 800 mm	0.127	2.50
S10-B	36.57	9.75	8 # 4 + 16 # 4	0.098	2 x #4 @ 800 mm	0.107	3.75
S11-B	3.65	7.31	8 # 3 + 6 # 4	0.083	# 5 @ 1220 mm	0.085	0.50
S12-B	6.09	9.75	8 # 5 + 8 # 4	0.125	# 4 @ 800 mm	0.082	0.62
S13-B	12.19	9.75	8 # 6 + 8 # 6	0.216	# 6 @ 800 mm	0.180	1.25
S14-B	24.38	9.75	8 # 8 + 8 # 8	0.387	# 4 @ 800 mm	0.082	2.50
S15-B	36.57	9.75	8 # 8 + 16 # 8	0.387	2 x #4 @1220 mm	0.072	3.75
S16-B	3.65	7.31	8 # 3 + 8 # 4	0.100	# 5 @ 1220 mm	0.085	0.50
S17-B	6.09	9.75	8 # 5 + 8 # 4	0.125	# 5 @ 800 mm	0.127	0.62
S18-B	12.19	9.75	8 # 6 + 8 # 6	0.216	# 6 @ 800 mm	0.180	1.25
S19-B	24.38	9.75	8 # 8 + 8 # 8	0.387	# 4 @ 800 mm	0.082	2.50
S20-B	36.57	9.75	8 # 8 + 16 # 8	0.387	2 x #4 @1220 mm	0.072	3.75

Table 2.3 Performance Groups for Evaluation of RM Shear Walls with Boundary Elements Archetypes.

Group Number	Archetype Design ID Number	Performance Group Summary			
		Design Load Level		Period Domain	Number of Archetypes
		Gravity	SDC		
PG-1S	S1-B to S3-B	High	D_{max}	Short	3
PG-2S	S4-B to S5-B			Long	2
PG-3S	S6-B to S7-B		D_{min}	Short	2
PG-4S	S8-B to S10-B			Long	3
PG-5S	S11-B to S13-B	Low	D_{max}	Short	3
PG-6S	S14-B to S15-B			Long	2
PG-7S	S16-B to S17-B		D_{min}	Short	2
PG-8S	S18-B to S20-B			Long	3

Table 2.4 Special RM Shear Wall with Boundary Element Archetype Design Characteristics.

Archetype Design ID Number	Key Archetype Design Parameters						
	Number of Stories	Gravity Loads	Seismic Design Category (SDC)	T (Sec)	T_1 (Sec)	V/W (g)	S_{MT} (g)
Performance Group No. PG-1S							
S1-B	1	High	D_{max}	0.25	0.12	0.200	1.50
S2-B	2	High	D_{max}	0.26	0.14	0.200	1.50
S3-B	4	High	D_{max}	0.45	0.20	0.200	1.50
Performance Group No. PG-2S							
S4-B	8	High	D_{max}	0.75	0.56	0.160	1.20
S5-B	12	High	D_{max}	1.02	1.16	0.118	0.89
Performance Group No. PG-3S							
S6-B	1	High	D_{min}	0.25	0.14	0.100	0.75
S7-B	2	High	D_{min}	0.28	0.15	0.100	0.75
Performance Group No. PG-4S							
S8-B	4	High	D_{min}	0.48	0.32	0.084	0.63
S9-B	8	High	D_{min}	0.80	0.92	0.050	0.37
S10-B	12	High	D_{min}	1.09	1.88	0.037	0.28
Performance Group No. PG-5S							
S11-B	1	Low	D_{max}	0.25	0.12	0.200	1.50
S12-B	2	Low	D_{max}	0.26	0.14	0.200	1.50
S13-B	4	Low	D_{max}	0.45	0.24	0.200	1.50
Performance Group No. PG-6S							
S14-B	8	Low	D_{max}	0.75	0.62	0.160	1.20
S15-B	12	Low	D_{max}	1.02	1.02	0.118	0.89
Performance Group No. PG-7S							
S16-B	1	Low	D_{min}	0.25	0.14	0.100	0.75
S17-B	2	Low	D_{min}	0.28	0.15	0.100	0.75
Performance Group No. PG-8S							
S18-B	4	Low	D_{min}	0.48	0.40	0.084	0.63
S19-B	8	Low	D_{min}	0.80	1.10	0.050	0.37
S20-B	12	Low	D_{min}	1.09	2.02	0.037	0.28

Table 2.5 Summary of Collapse Results for Special RM Shear Wall Archetype Designs (High Gravity Loads).

Archetype Design ID Number	Design Configuration			Pushover and IDA Results			
	Number of Stories	Gravity Loads	Seismic Design Category (SDC)	Static Ω	$S_{MT}[T]$ (g)	$S_{CT}[T]$ (g)	Collapse Margin Ratio (CMR)
Performance Group No. PG-1S							
S1	1	High	D_{max}	1.63 (1.84)	1.50	0.84 (0.78)	0.56 (0.52)
S1-B	1	High	D_{max}	1.78	1.50	3.17	2.11
S2	2	High	D_{max}	2.34 (2.28)	1.50	1.98 (1.71)	1.32 (1.14)
S2-B	2	High	D_{max}	2.66	1.50	4.36	2.90
S3	4	High	D_{max}	1.67 (1.87)	1.50	(2.33)	(1.55)
S3-B	4	High	D_{max}	1.80	1.50	4.71	3.14
Performance Group No. PG-2S							
S4	8	High	D_{max}	1.54 (1.89)	1.20	(1.57)	(1.31)
S4-B	8	High	D_{max}	1.68	1.20	2.23	1.85
S5	12	High	D_{max}	1.49 (1.61)	0.89	1.53 (1.72)	1.72 (1.94)
S5-B	12	High	D_{max}	1.59	0.89	1.97	2.21
Performance Group No. PG-3S							
S6	1	High	D_{min}	1.99 (1.62)	0.75	(0.78)	(1.04)
S6-B	1	High	D_{min}	2.27	0.75	2.13	2.84
S7	2	High	D_{min}	2.67 (2.61)	0.75	(1.44)	(1.92)
S7-B	2	High	D_{min}	2.95	0.75	2.70	3.60
Performance Group No. PG-4S							
S8	4	High	D_{min}	1.48 (1.65)	0.63	(1.04)	(1.65)
S8-B	4	High	D_{min}	1.59	0.63	2.61	4.14
S9	8	High	D_{min}	1.55 (1.93)	0.37	(0.60)	(1.63)
S9-B	8	High	D_{min}	1.66	0.37	0.92	2.48
S10	12	High	D_{min}	1.32 (1.68)	0.28	(0.58)	(2.07)
S10-B	12	High	D_{min}	1.42	0.28	0.96	3.42

(   ): Values from the GCR 10-917-8 (NIST 2010) study.

Table 2.6 Summary of Collapse Results for Special RM Shear Wall Archetype Designs (Low Gravity Loads).

Archetype Design ID Number	Design Configuration			Pushover and IDA Results			
	Number of Stories	Gravity Loads	Seismic Design Category (SDC)	Static Ω	$S_{MT}[T]$ (g)	$S_{CT}[T]$ (g)	Collapse Margin Ratio (CMR)
Performance Group No. PG-5S							
S11	1	Low	D_{max}	1.63 (1.84)	1.50	0.84 (0.78)	0.56 (0.52)
S11-B	1	Low	D_{max}	1.78	1.50	3.17	2.11
S12	2	Low	D_{max}	1.90 (1.82)	1.50	(2.57)	(1.71)
S12-B	2	Low	D_{max}	2.40	1.50	6.10	4.06
S13	4	Low	D_{max}	1.47 (1.73)	1.50	(2.48)	(1.65)
S13-B	4	Low	D_{max}	1.76	1.50	5.37	3.58
Performance Group No. PG-6S							
S14	8	Low	D_{max}	1.15 (1.59)	1.20	(1.57)	(1.31)
S14-B	8	Low	D_{max}	1.34	1.20	3.25	2.60
S15	12	Low	D_{max}	1.15 (1.47)	0.89	(1.72)	(1.94)
S15-B	12	Low	D_{max}	1.24	0.89	3.99	4.48
Performance Group No. PG-7S							
S16	1	Low	D_{min}	1.99 (1.62)	0.75	(0.78)	(1.04)
S16-B	1	Low	D_{min}	2.27	0.75	2.13	2.84
S17	2	Low	D_{min}	2.10 (1.80)	0.75	(1.79)	(2.38)
S17-B	2	Low	D_{min}	2.56	0.75	3.90	5.20
Performance Group No. PG-8S							
S18	4	Low	D_{min}	1.47 (1.41)	0.63	(1.04)	(1.65)
S18-B	4	Low	D_{min}	1.76	0.63	3.15	5.00
S19	8	Low	D_{min}	1.64 (1.22)	0.37	(0.61)	(1.63)
S19-B	8	Low	D_{min}	1.42	0.37	1.81	4.89
S20	12	Low	D_{min}	1.16 (1.46)	0.28	(0.59)	(2.13)
S20-B	12	Low	D_{min}	1.20	0.28	2.57	9.17

(   ): Values from the GCR 10-917-8 (NIST 2010) study.

Table 2.7 Summary of Collapse performance evaluation of Special RM Shear Wall Archetypes. (High Gravity Loads).

Arch. Design ID No.	Design Configuration		Computed Overstrength and Collapse Margin Parameters					Acceptance Check	
	No. of Stories	Boundary Conditions	Ω	CMR	μ_T	SSF	ACMR	Accept. ACMR	Pass/ Fail
Performance Group No. PG-1S									
S1	1	Without B.E.*	1.84	0.52	5.20	1.26	0.66	1.56	**Fail**
S1-B	1	With B.E.*	1.78	2.11	13.2	1.33	2.80	1.56	Pass
S2	2	Without B.E.*	2.28	1.14	8.10	1.33	1.52	1.56	**Fail**
S2-B	2	With B.E.*	2.66	2.90	16.0	1.33	3.85	1.56	Pass
S3	4	Without B.E.*	1.87	1.55	11.8	1.33	2.06	1.56	Pass
S3-B	4	With B.E.*	1.80	3.14	14.5	1.33	4.17	1.56	Pass
Mean of PG-1S		Without B.E.*	2.00				1.41	1.96	**Fail**
		With B.E.*	2.08				3.60	1.96	Pass
Performance Group No. PG-2S									
S4	8	Without B.E.*	1.89	1.31	6.4	1.35	1.76	1.56	Pass
S4-B	8	With B.E.*	1.68	1.85	10.6	1.39	2.57	1.56	Pass
S5	12	Without B.E.*	1.61	1.94	14.6	1.47	2.84	1.56	Pass
S5-B	12	With B.E.*	1.59	2.21	22.5	1.47	3.24	1.56	Pass
Mean of PG-2S		Without B.E.*	1.75				2.30	1.96	Pass
		With B.E.*	1.64				2.91	1.96	Pass
Performance Group No. PG-3S									
S6	1	Without B.E.*	1.62	1.04	13.3	1.14	1.19	1.56	**Fail**
S6-B	1	With B.E.*	2.27	2.84	19.0	1.14	3.23	1.56	Pass
S7	2	Without B.E.*	2.61	1.92	14.4	1.14	2.18	1.56	Pass
S7-B	2	With B.E.*	2.95	3.60	24.3	1.14	4.10	1.56	Pass
Mean of PG-3S		Without B.E.*	2.12				1.69	1.96	**Fail**
		With B.E.*	2.61				3.66	1.96	Pass
Performance Group No. PG-4S									
S8	4	Without B.E.*	1.65	1.65	28.4	1.14	1.88	1.56	Pass
S8-B	4	With B.E.*	1.59	4.14	34.8	1.14	4.71	1.56	Pass
S9	8	Without B.E.*	1.93	1.63	7.1	1.25	2.03	1.56	Pass
S9-B	8	With B.E.*	1.66	2.48	11.8	1.20	2.98	1.56	Pass
S10	12	Without B.E.*	1.68	2.07	16.0	1.37	2.84	1.56	Pass
S10-B	12	With B.E.*	1.42	3.42	24.3	1.27	4.34	1.56	Pass
Mean of PG-4S		Without B.E.*	1.75				2.25	1.96	Pass
		With B.E.*	1.56				4.01	1.96	Pass

*B.E: Boundary elements.

- Results of walls without boundary elements are from the GCR 10-917-8 (NIST 2010) study.

Table 2.8 Summary of Collapse performance evaluation of Special RM Shear Wall Archetypes. (Low Gravity Loads).

Arch. Design ID No.	Design Configuration		Computed Overstrength and Collapse Margin Parameters					Acceptance Check	
	No. of Stories	Boundary Conditions	Ω	CMR	μ_T	SSF	ACMR	Accept. ACMR	Pass/ Fail
Performance Group No. PG-5S									
S11	1	Without B.E.*	1.84	0.52	5.20	1.26	0.66	1.56	**Fail**
S11-B	1	With B.E.*	1.78	2.11	13.2	1.33	2.80	1.56	Pass
S12	2	Without B.E.*	1.82	1.71	8.3	1.33	2.27	1.56	Pass
S12-B	2	With B.E.*	2.40	4.06	14.2	1.33	5.39	1.56	Pass
S13	4	Without B.E.*	1.73	1.65	11.3	1.33	2.19	1.56	Pass
S13-B	4	With B.E.*	1.76	3.65	23.6	1.33	4.85	1.56	Pass
Mean of PG-5S		Without B.E.*	1.80				1.71	1.96	**Fail**
		With B.E.*	1.98				4.34	1.96	Pass
Performance Group No. PG-6S									
S14	8	Without B.E.*	1.59	1.31	13.6	1.40	1.82	1.56	Pass
S14-B	8	With B.E.*	1.34	2.60	28.2	1.40	3.64	1.56	Pass
S15	12	Without B.E.*	1.47	1.94	42.8	1.47	2.84	1.56	Pass
S15-B	12	With B.E.*	1.24	4.48	66.8	1.47	6.58	1.56	Pass
Mean of PG-6S		Without B.E.*	1.53				2.33	1.96	Pass
		With B.E.*	1.29				5.11	1.96	Pass
Performance Group No. PG-7S									
S16	1	Without B.E.*	1.62	1.04	13.3	1.14	1.19	1.56	**Fail**
S16-B	1	With B.E.*	2.27	2.84	19.0	1.14	3.23	1.56	Pass
S17	2	Without B.E.*	1.80	2.38	14.4	1.14	2.71	1.56	Pass
S17-B	2	With B.E.*	2.56	5.20	24.2	1.14	5.92	1.56	Pass
Mean of PG-7S		Without B.E.*	1.71				1.95	1.96	**Fail**
		With B.E.*	2.41				4.50	1.96	Pass
Performance Group No. PG-8S									
S18	4	Without B.E.*	1.41	1.65	29.0	1.14	1.88	1.56	Pass
S18-B	4	With B.E.*	1.76	5.00	48.0	1.14	5.70	1.56	Pass
S19	8	Without B.E.*	1.64	1.63	17.7	1.26	2.05	1.56	Pass
S19-B	8	With B.E.*	1.42	4.89	31.5	1.20	5.86	1.56	Pass
S20	12	Without B.E.*	1.46	2.13	20.7	1.37	2.92	1.56	Pass
S20-B	12	With B.E.*	1.20	9.17	33.7	1.27	11.60	1.56	Pass
Mean of PG-8S		Without B.E.*	1.50				2.28	1.96	Pass
		With B.E.*	1.46				7.72	1.96	Pass

*B.E: Boundary elements.

- Results of walls without boundary elements are from the GCR 10-917-8 (NIST 2010) study.

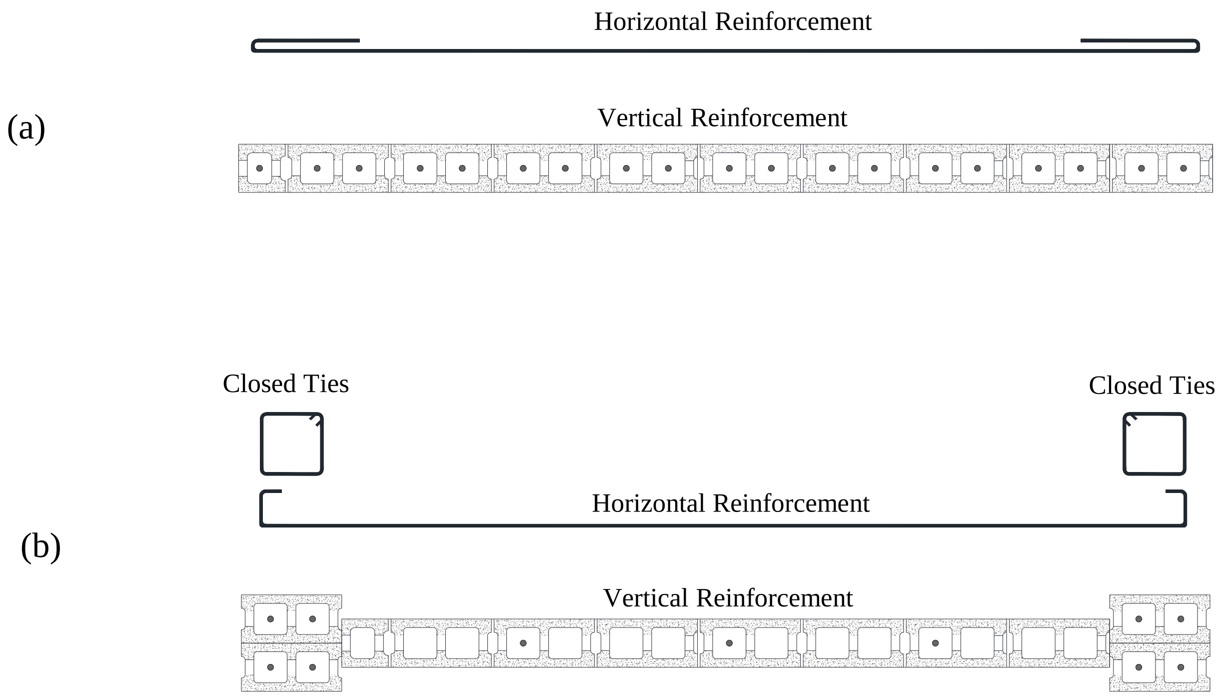

Fig. 2.1: Wall configurations: (a) Walls with rectangular cross section; (b) Wall with boundary elements.

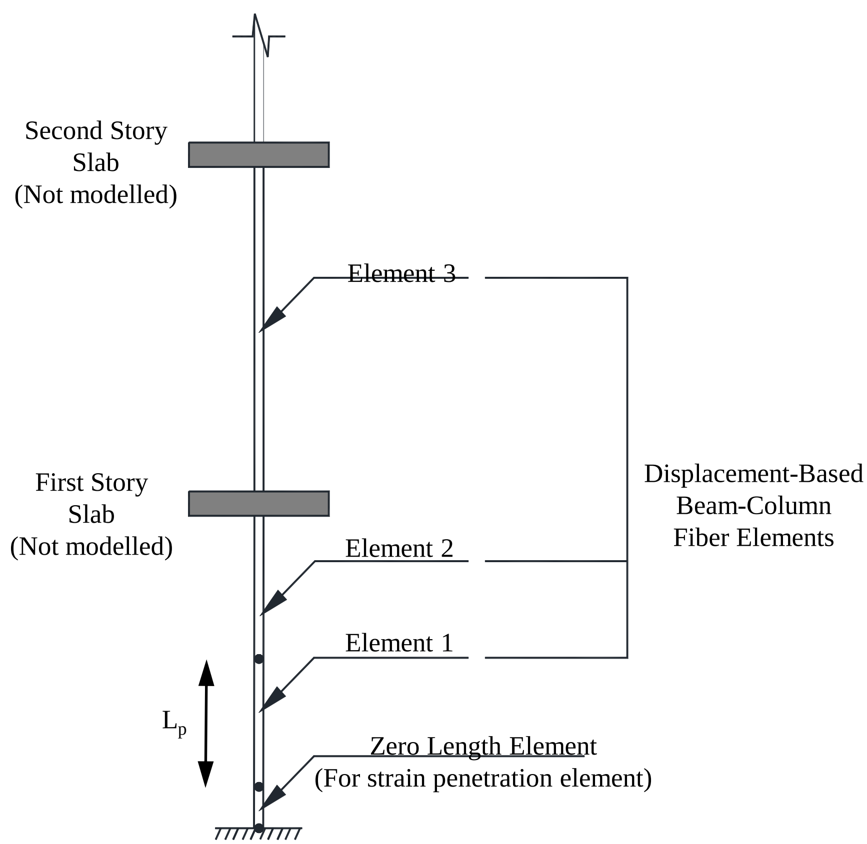

Fig. 2.2: Schematic diagram of the model.

(a)

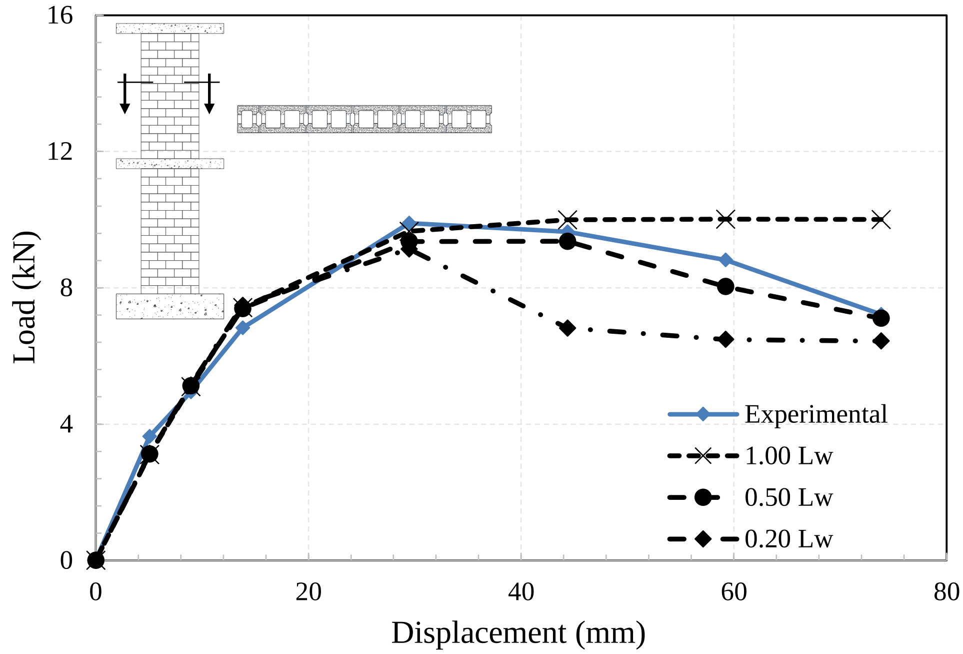

(b)

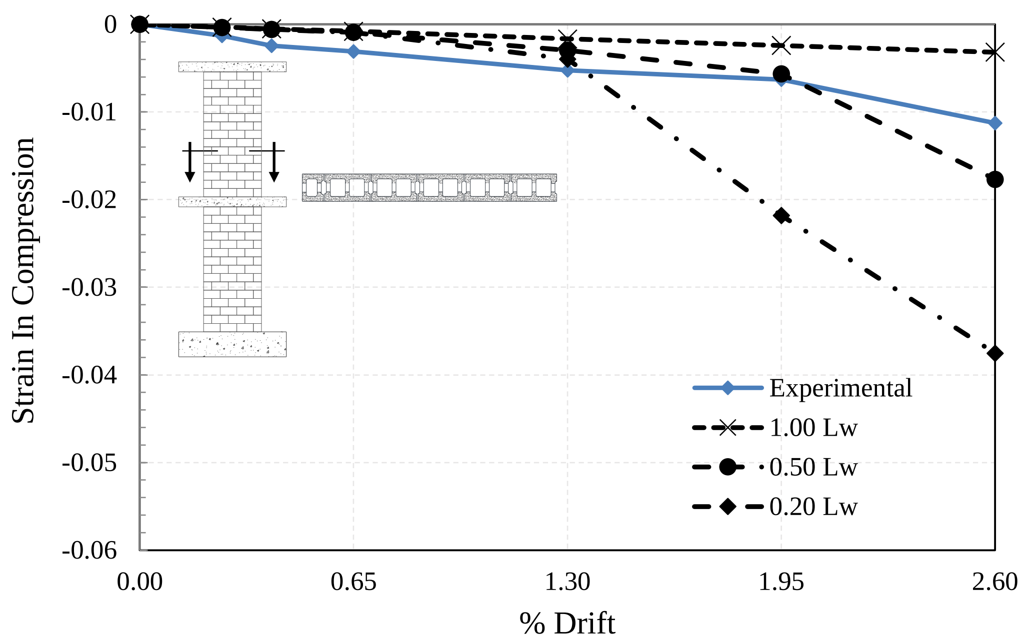

Fig. 2.3: Effect of element length on Wall W6:
(a) Load-displacement response; (b) Strain in compression.

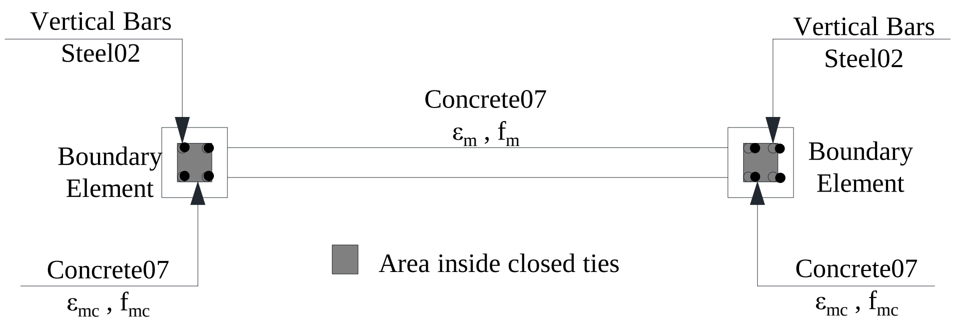

Fig. 2.4: Material distribution of RM shear walls with boundary elements used in the model.

(a)

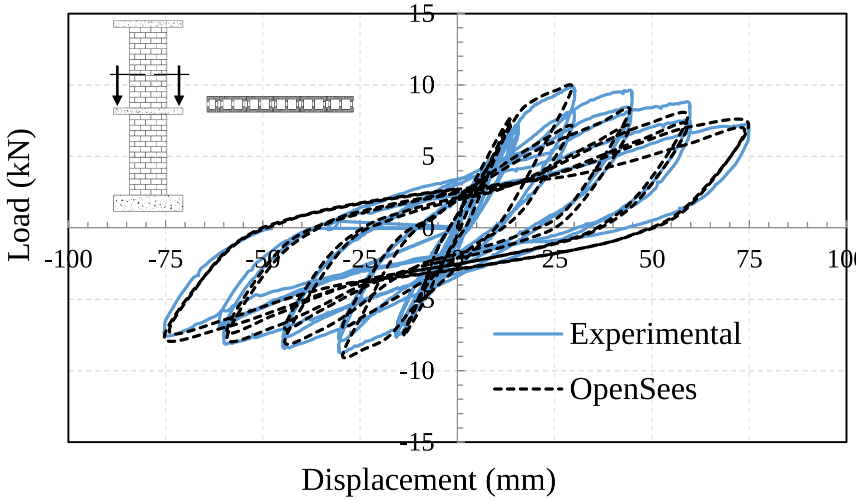

(b)

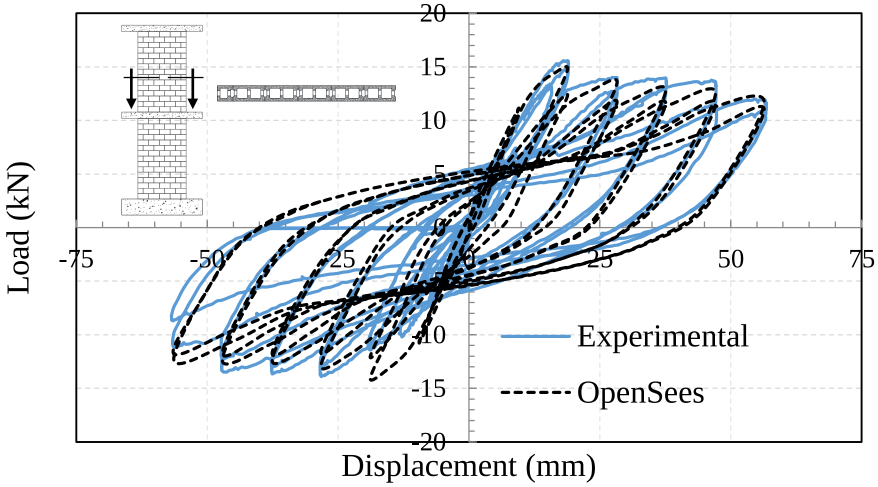

Fig. 2.5: Experimental and numerical hysteresis loops:

(a) Wall-W6 (Siyam et al.2015); (b) Wall-W5 (Siyam et al.2015).

(c)

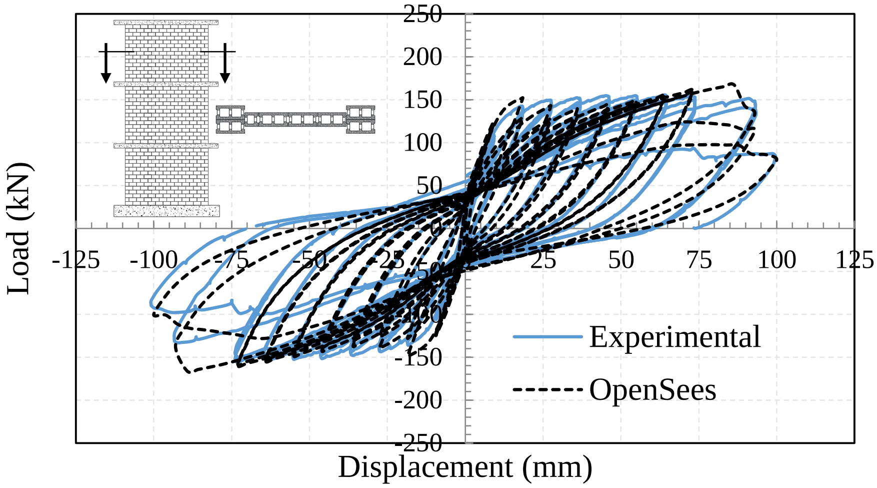

(d)

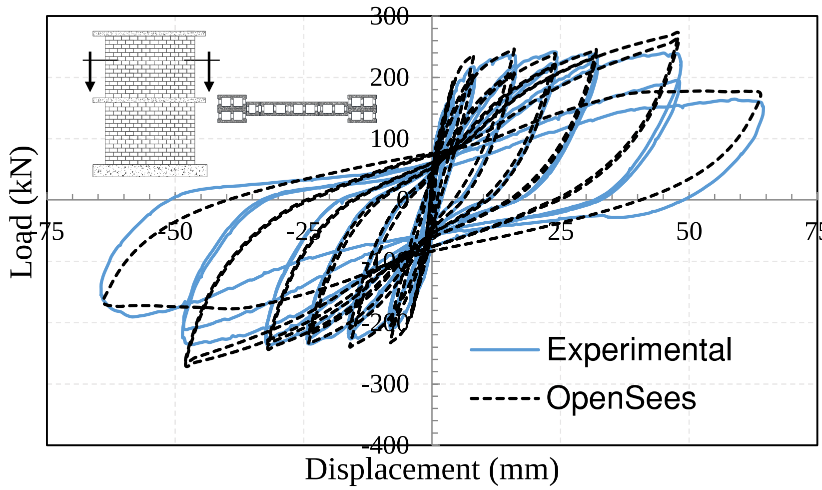

Fig. 2.5 (cont.): Experimental and numerical hysteresis loops:

(c) Wall-W3 (Shedid et al.2010); (d) Wall-W1 (Banting and El-Dakhakhni 2014).

(a)

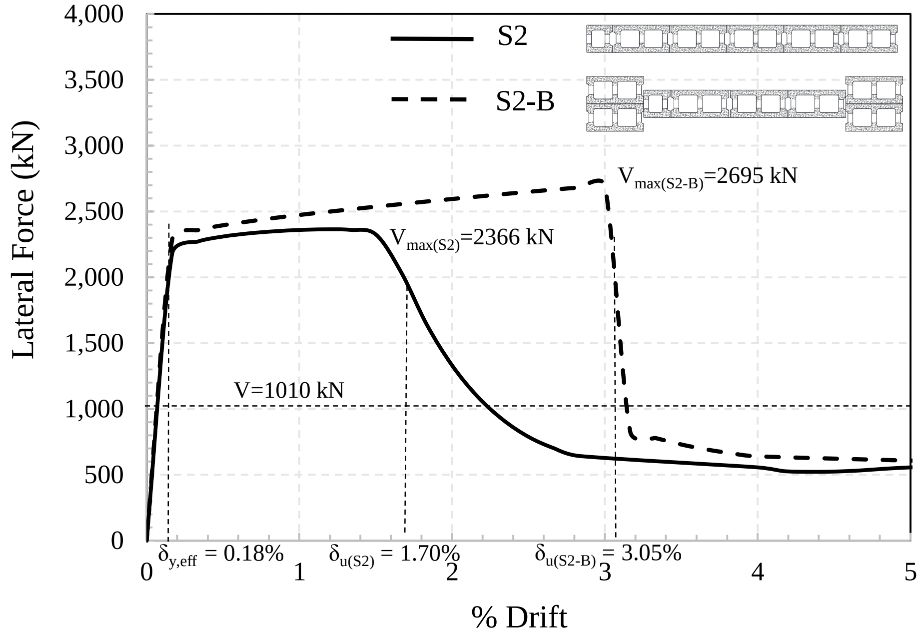

(b)

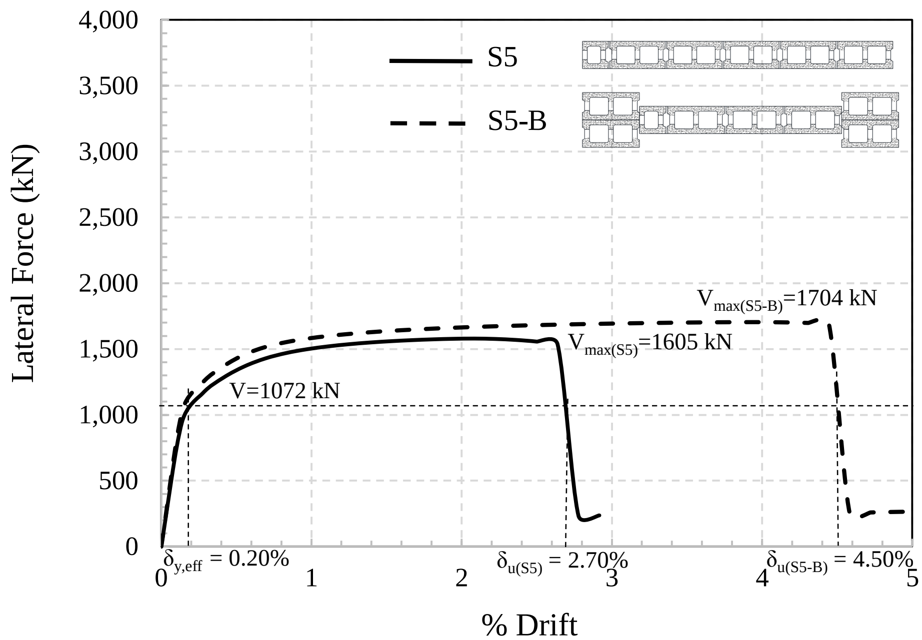

Fig. 2.6: Pushover curves:

(a) Archetype S2 (2 stories, high gravity loads); (b) Archetype S5 (12, stories, high gravity loads);

.

(c)

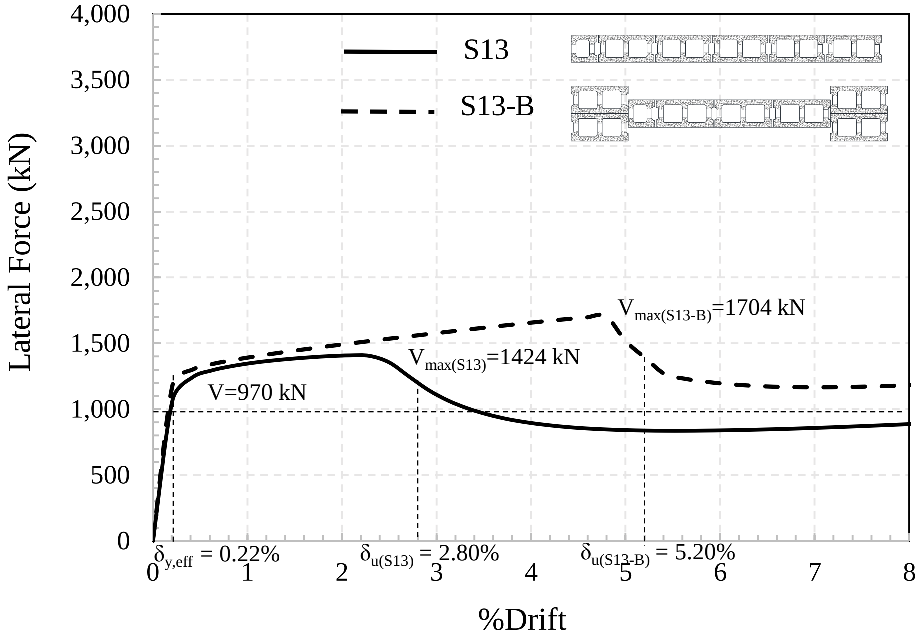

(d)

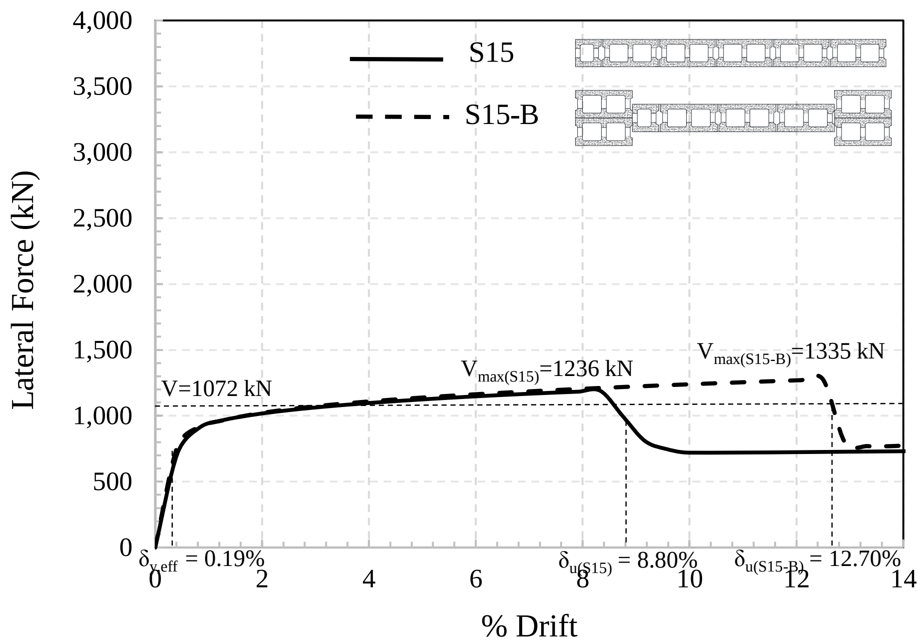

Fig. 2.6 (cont.): Pushover curves:

(c) Archetype S13 (4 stories, low axial loads); (d) Archetype S15 (12 stories, low axial loads).

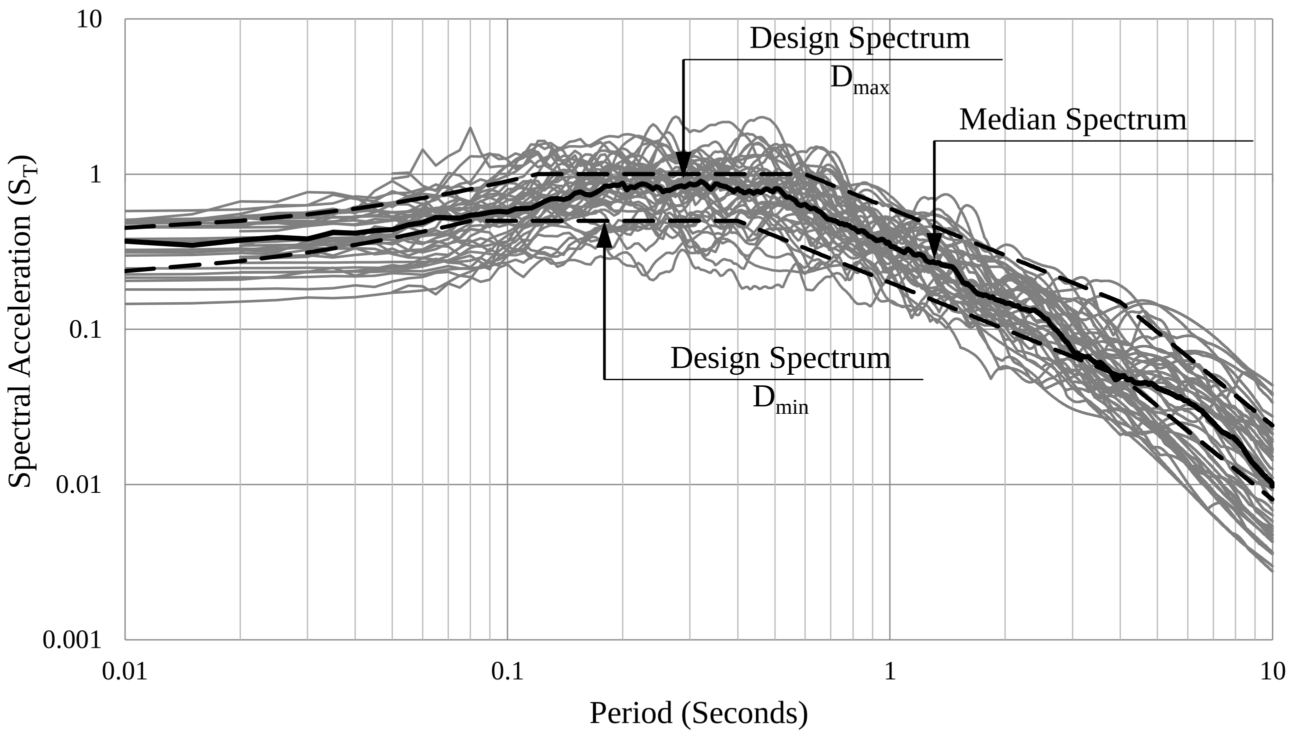

Fig. 2.7: Response spectra of the forty-four individual components of the normalized record set, median response spectrum of the total record set, design spectrum for SDC D_{max} and design spectrum for SDC D_{min} .

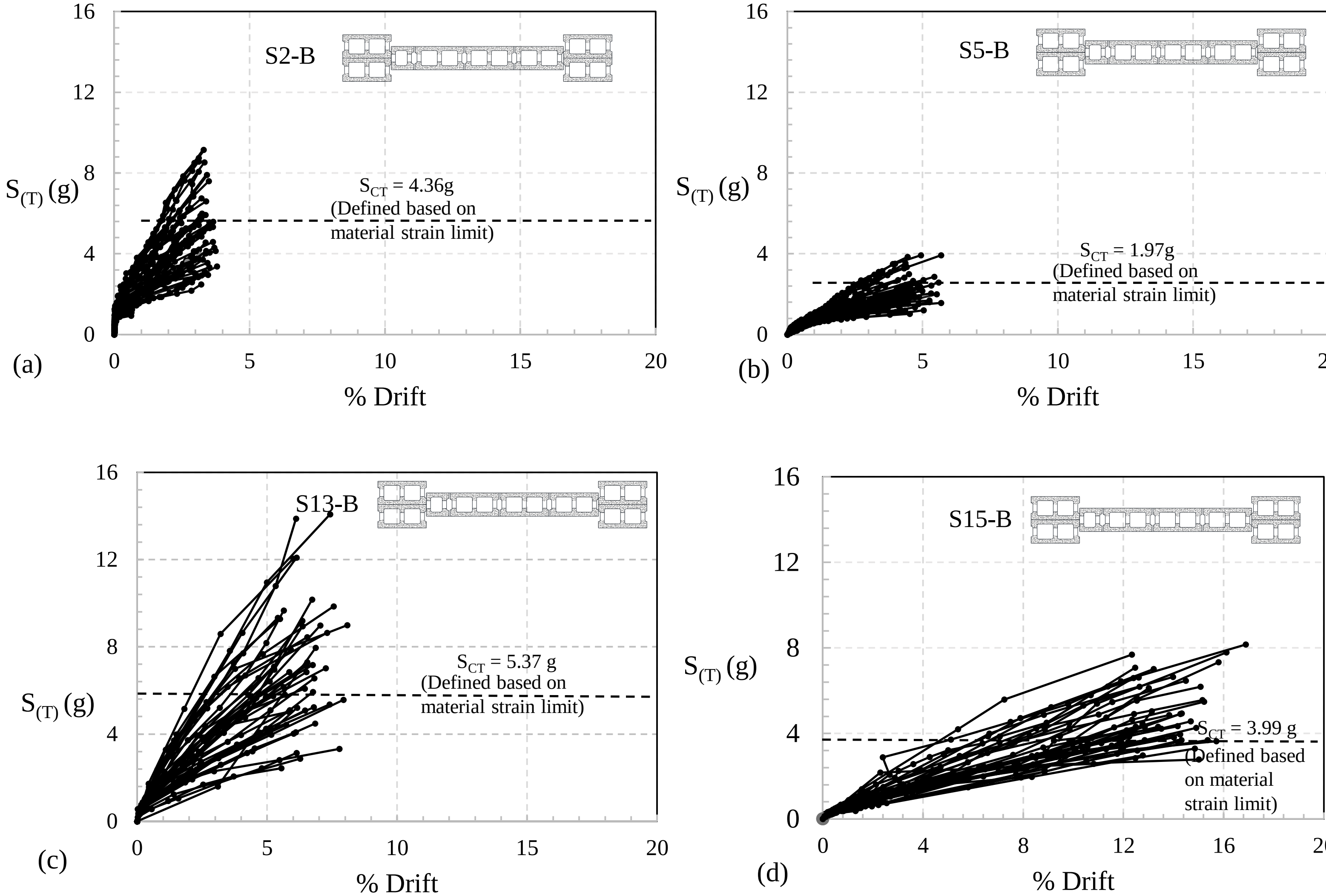

Fig. 2.8: Incremental Dynamic Analysis (IDA) response plot of spectral acceleration versus maximum story drift ratio: (a) Archetype S2 (2 stories, high gravity loads); (b) Archetype S5 (12 stories, high gravity loads); (c) Archetype S13 (4 stories, low axial loads); (d) Archetype S15 (12 stories, low axial loads).

(a)

(b)

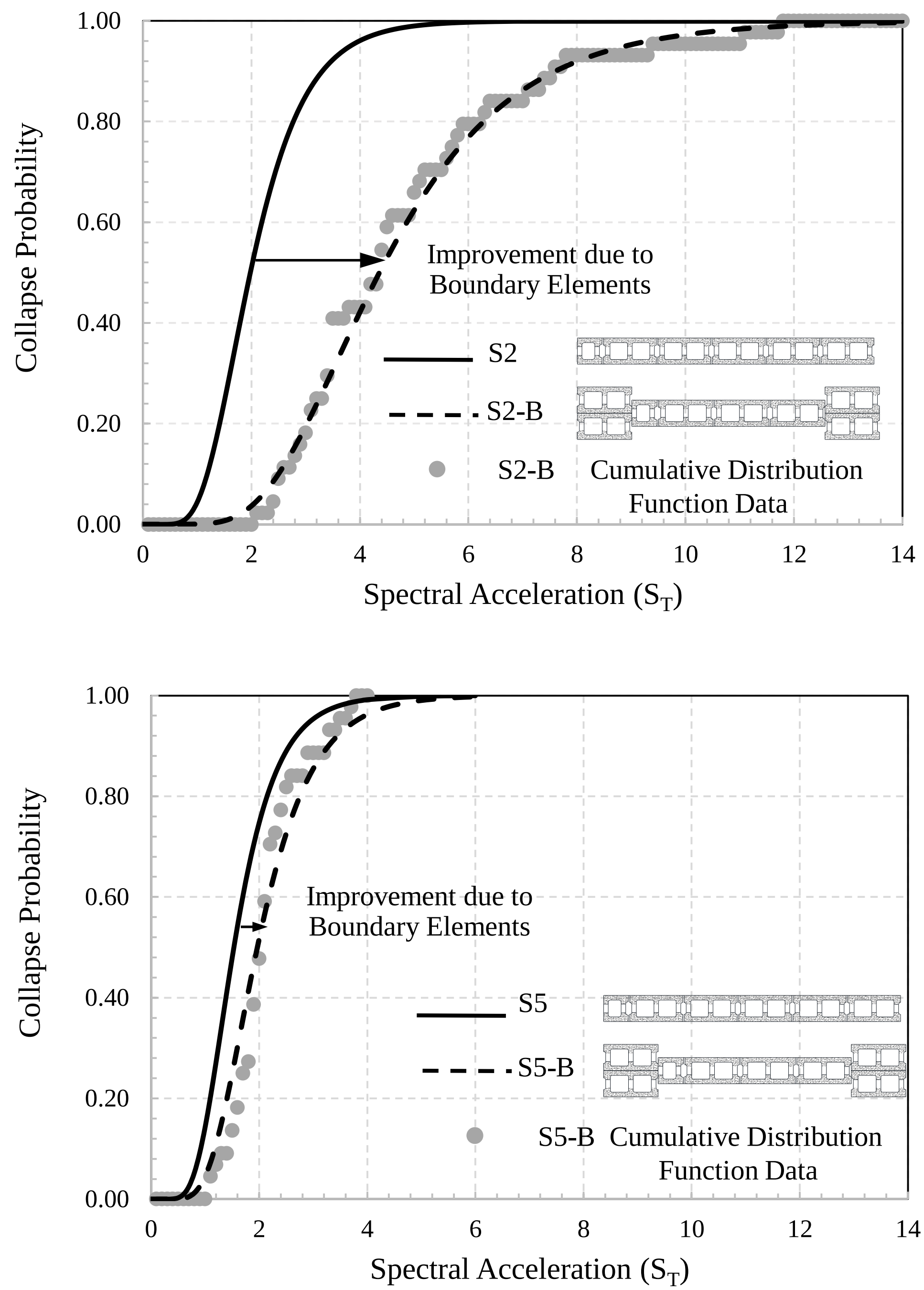

Fig. 2.9: Collapse fragility curves:

(a) Archetype S2 (2 stories, high gravity loads); (b) Archetype S5 (12 stories, high gravity loads).

(c)

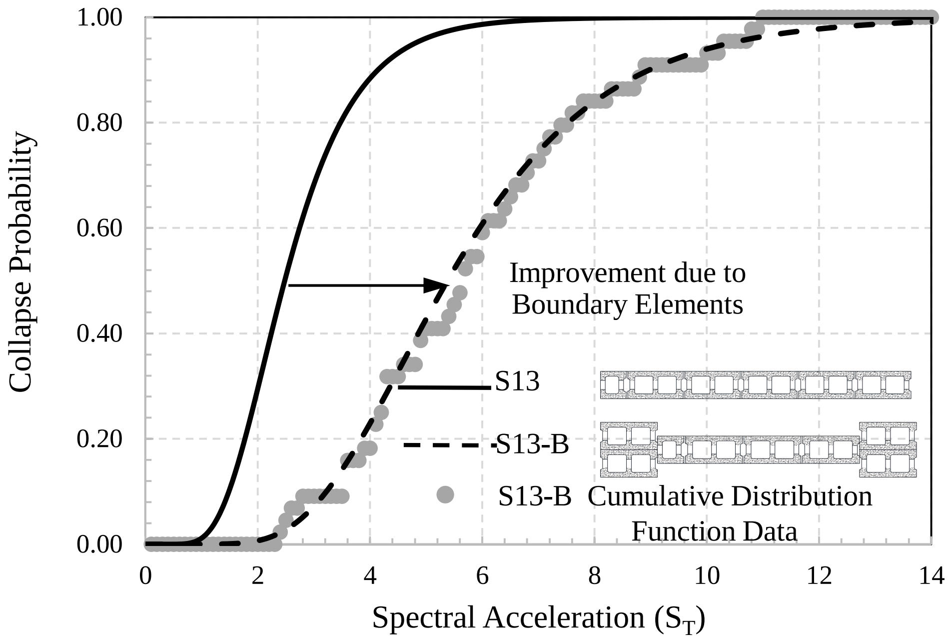

(d)

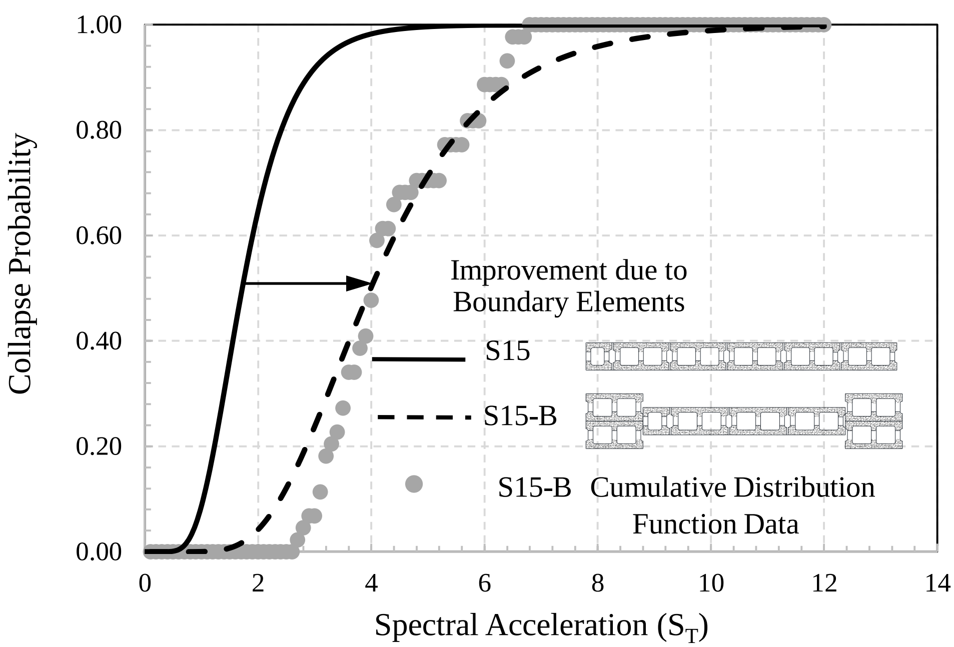

Fig. 2.9 (cont.): Collapse fragility curves:

(c) Archetype S13 (4 stories, low axial loads); (d) Archetype S15 (12 stories, low axial loads).

CHAPTER 3
EXPERIMENTAL ASSESSMENT OF THE SYSTEM-LEVEL SEISMIC PERFORMANCE OF AN ASYMMETRICAL REINFORCED CONCRETE BLOCK WALL BUILDING WITH BOUNDARY ELEMENTS

3.1 ABSTRACT

Using boundary elements in Reinforced Masonry (RM) walls allows closed ties to be used and multiple layers of vertical bars to be accommodated, thus providing a confining reinforcement cage. This enhances the overall performance of the RM wall relative to conventional rectangular RM wall systems, which typically have single-leg horizontal reinforcement and a single layer of vertical reinforcement. In addition, with the expected shift of design code developers' focus from the component- to the system-level assessment of Seismic Force Resisting System (SFRS), there is a need to experimentally quantify the system-level performance of RM buildings. To address this, an experimental asymmetrical two story reduced-scale RM shear wall building with boundary elements, referred to as *Building IV*, was tested to failure under reversed cyclic loading that simulates seismic demands. *Building IV* was designed to have the same lateral resistance as a previously tested RM shear wall building with conventional rectangular configuration (without boundary elements), referred to as *Building III*, to allow for direct comparison. Therefore, after a brief summary of the experimental program, the focus of this chapter is to compare the damage sequence and the load-displacement hysteretic behavior between the two buildings. The results

show that higher levels of ductility accompanied by relatively smaller strength degradation were achieved by *Building IV* compared to that of *Building III*. This study enlarges the database of system-level experimental results that will facilitate the adoption of RM shear walls with boundary elements as a SFRS within the next editions of the Masonry Standards Joint Committee and the Canadian masonry design code.

3.2 INTRODUCTION

Reinforced Masonry (RM) shear walls with conventional rectangular cross section are usually constructed with single-leg horizontal reinforcement and a single layer of vertical reinforcement because of practical limitations associated with masonry unit configuration that use standard two-cell 190-mm (8 inch) block. As such, little or no confinement is usually available at the critical wall compression zones. Such a reinforcing arrangement may lead to instability at the wall toes under high inelastic strains in the vertical bars during reversed seismic loading (Shedid et al. 2010). Conversely, boundary elements allow closed ties to replace the conventional 180° hook formed by the horizontal shear reinforcement, and they also accommodate multiple layers of vertical bars, thus providing a confining reinforcing cage within a RM shear wall (Banting and El-Dakhakhni 2012). This in turn reduces the possibility of the vertical wall reinforcement buckling as well as crushing of the grout core. As a result, face shell spalling within the compression toes does not cause an abrupt drop in resistance, thus enhancing the overall performance of the RM shear wall Seismic Force Resisting System (SFRS). In addition, the behavior of RM walls with boundary elements is characterized by a reduced depth of neutral axis relative to RM shear walls with conventional rectangular cross section, which decreases the wall cross section's curvature at yield and increases its ultimate curvature. Together, these two effects significantly increase the curvature ductility, and thus the wall displacement ductility (Banting and El-Dakhakhni 2014).

Very little research has been carried out on the performance of RM walls with boundary elements under lateral load because early methods of confining masonry did not diverge from a conventional wall layout of a rectangular cross-section, with a single layer of vertical reinforcement. Instead, research was focused on alternative materials that could be placed within the masonry units to provide confining effects (Priestley and Bridgeman 1974; Mayes et al. 1976; Priestley and Elder 1982; Hart et al. 1989). Different types of confinement were proposed (e.g. closed wire mesh, seismic combs and steel plates) to improve the post-peak behavior of RM walls. For example, stainless steel plates were placed on the mortar bed on the face shell and web of the units to confine masonry (Priestley and Bridgeman 1974 and Priestley and Elder 1982). This technique had the effect of increasing the ultimate compressive strain in the confined masonry and thus increasing the overall displacement ductility of the wall. More recent work focused on the confinement of unreinforced grouted concrete block using two types of welded wire mesh (Dhanasekar and Shrive 2002) to confine the grouted cells in unreinforced concrete block prisms. The wire mesh proved to be an effective means of increasing the peak compressive strength. The previous methods have the benefit of increasing the compressive strain capacity of the masonry, but they do not offer any enhancement of the stability for a single row of vertical reinforcement. Conversely, the use of masonry boundary elements detailed as confined columns presents an opportunity for practical application and formalized prescriptive design code requirements (Shedid et al. 2010 and Banting and El-Dakhakhni 2012).

With an expected shift of design code developers' focus from component- to system-level assessment of SFRS, there is a need to experimentally quantify the performance of whole RM buildings. However, very limited experimental studies have been conducted on RM walls at the system-level (Abrams 1986; Seible et al. 1993, 1994; Tomaževič and Weiss 1994; Zonta et al. 2001; Cohen et al. 2004; Stavridis et al. 2011; Heerema et al. 2015; Ashour et al. 2016), when compared to those on individual RM components (Priestley 1976; Brunner 1994; Ibrahim and Sutter 1999; Voon and Ingham 2006; Shedid et al. 2008 and 2010; Banting and El-Dakhakhni 2012; Ahmadi et al. 2014; Siyam et al. 2015). Many researchers argued that there are some system-level aspects (e.g. slab's in-plane and out-of-plane rigidity) that cannot be evaluated or assessed through component-level studies. For example, Ashour et al. (2016) reported that slab flexural coupling was an important system-level aspect that affected the overall RM building performance. This included the building stiffness, lateral resistance capacity, and trend of stiffness degradation, which in turn would significantly change the overall building response under seismic loading.

All the experimental studies to date have been performed for conventional rectangular RM wall systems, whereas RM wall systems with boundary elements are a newly proposed structural system. The Masonry Standards Joint Committee has not yet established requirements for longitudinal and transverse reinforcement of RM walls with boundary elements and has recommended in the commentary to *Clause 9.3.6.5.5* that more testing is needed to facilitate the development of prescriptive design requirements (MSJC 2013). As such, no experimental investigation is reported for RM wall systems with boundary elements to date.

The current study represents a part of a larger research program that was initiated at McMaster University to facilitate a better understanding of the system-level seismic response of RM shear walls buildings without and with boundary elements. *Phase I* was reported by Siyam et al. (2015), where the experimental program focused on the flexural response of six reduced-scale two-story fully grouted RM shear walls under a displacement-controlled quasi-static cyclic fully-reversed loading. This test program was designed to assess the component-level performance of RM walls with different configurations and aspect ratios. *Phase II* was focused on testing identical walls to those studied in *Phase I*, but within a scaled two-story asymmetrical RM shear wall building (Heerema et al. 2015). In *Phase II,* the level of coupling between walls during the test was minimized in order to isolate and quantify the torsional response of the building. This was done by detailing the building with hinge lines along the two floor slabs, in order to prevent coupling and to facilitate in-plane diaphragm rotation and subsequent building twist. In *Phase III*, the building reported by Ashour et al. (2016), referred to as *Building III* hereafter, was identical to that studied in *Phase II*, but without hinge lines in order to investigate the effects of wall coupling on the building and wall response. All walls in *Phases I*, *II* and *III* had conventional rectangular cross sections.

The objective of this chapter is to present the test results of the building tested within *Phase IV* (referred to as *Building IV* hereafter). The RM shear walls in *Building IV* were designed to have the same lateral resistance as their corresponding in *Building III* to allow for direct comparison. However, the RM shear walls located along the main direction of loading in *Building III* were replaced by RM shear walls with confined boundary elements. *Building IV* was also tested under an identical loading scheme to that adopted in *Phase III*. In this respect, the chapter first presents a description of the experimental program, test setup and instrumentation, and provides information about the properties of the materials used in *Building IV* construction. Following the experimental program description, the chapter focuses on comparing the damage sequence and the load-displacement hysteretic behavior between *Building III* and *Building IV*. Finally, the twist response is evaluated through quantitative comparison between *Buildings III* and *IV*, by comparing the twist angles of the two buildings corresponding to different drift levels throughout the tests.

3.3 EXPERIMENTAL PROGRAM

3.3.1 Building Layout and Wall Design Criteria

The experimental program was designed to evaluate the system-level performance of a two-story one-third scale RM building with boundary elements, shown in Fig. 3.1(a) from the South direction and in Fig. 3.1(b) from the East direction. The building was composed of four shear walls with boundary elements aligned along the loading direction, and four other orthogonal conventional rectangular shear walls. The overall height of the building was 2,160 mm, comprised of two floors, each 1,000 mm in height, corresponding to 3,000 mm in full-scale, with two 80 mm thick reinforced concrete (RC) floor diaphragms, each 2,400 mm × 2,400 mm in plan. The building was fixed to the laboratory structural floor by 16 prestressed anchors through a square RC foundation (3,000 mm × 3,000 mm) with a thickness of 250 mm.

The individual walls in *Building IV* were designed to have the same lateral resistance as those within *Building III* to allow for direct comparison. Therefore, both buildings had almost the same strength eccentricity, and thus the torsional response was not considered during the design of the walls. The confinement technique used in this study was similar to that adopted in Shedid et al. (2010), in which two standard blocks were used to form the boundary elements with a single bar in each cell. This technique was chosen because it can be easily adopted using conventional RM construction materials and technique. The main difference between the two buildings is that the conventional shear walls ($W1_{III}$, $W2_{III}$, $W5_{III}$ and $W8_{III}$) along the direction of loading in *Building III* were replaced by shear walls with confined boundary elements ($W1_{IV}$, $W2_{IV}$, $W5_{IV}$ and $W8_{IV}$) in *Building IV*, as shown in Figs. 3.2 (a and b). The wall configuration in plan was originally selected during *Phase II*, in order to produce an eccentricity between the building floor Center of Mass, C_M, and the building Center of Rigidity, C_R, at the roof level, so as to engage the torsional response of the building under the applied lateral loads (Heerema et al. 2015). Therefore, Wall $W8_{IV}$ was placed on the West side of the building and the two Walls $W1_{IV}$ and $W2_{IV}$ were placed on the East side of the building in addition to Wall $W5_{III}$ along the North-South direction, as shown in Fig. 3.2(c). The four orthogonal walls, Walls $W3_{IV}$ and $W4_{IV}$, located at the South side, and Walls $W6_{IV}$ and $W7_{IV}$, located at the North side, were identically placed to those in *Building III* to enhance the building's torsional response.

Flexural strength predictions were carried out by using cross-sectional analysis (Priestley and Elder 1982; Shedid et al. 2010). For the yield strength, Q_y, a linear strain profile, with a yield strain of the outermost steel reinforcement set to 0.0025, was used. The ultimate masonry strain was taken as 0.003, as specified by CSA S304-14 (CSA 2014a), when calculating the wall ultimate flexural capacity, Q_u. The shear strength, V_u, was also calculated following CSA S304-14

(CSA 2014a) within the plastic hinge region, where the Canadian code accounts for 50% reduction in masonry shear strength. The sliding strength, V_s, was also calculated at the foundation level following CSA S304-14 (CSA 2014a). Table 3.1 summarizes the RM wall dimensions, vertical and horizontal reinforcement details and aspect ratios for all walls within *Building IV*, while Table 3.2 shows the yield strengths, ultimate flexural strengths, shear strengths and sliding strengths for the same walls. To meet the design criteria, the walls in *Building IV* had a range of vertical reinforcement ratios that ranged from 0.40% to 0.60%, which was only about 90% of the amount used in the walls for *Building III*.

3.3.2 Material Properties and Construction

A one-third scale version of the standard two-cell 190-mm hollow concrete masonry unit (190 × 190 × 390 mm) commonly used in North America was used for the building's wall construction. The reduced-scale concrete blocks were 130 mm in length, 63 mm in width and 63 mm in height. Several mixes were studied and compared to represent the properties (i.e. absorption, mix design, etc.) of their corresponding full-scale prototypes using the one-third scale ones (Hughes 2010). The third-scale blocks were randomly selected and tested in accordance with ASTM C140-08 (ASTM 2008a) and CSA A165-14 (CSA 2014b) using hard capping, and the average compressive strengths for the blocks, based on net area of 4,320 mm^2, were 21.1 MPa (coefficient of variation (c.o.v.) = 13.7%) and 20.2 MPa (c.o.v. = 12.5%), for the stretcher and half units, respectively. Wall construction was conducted using approximately 3 mm thick mortar joints to resemble the scaled version of the common 10 mm joints in full-scale masonry construction. Type S mortar was used in wall construction with proportions of portland cement: lime: dry sand: water of 1.0: 0.2: 3.5: 0.85, and having an average flow of 124%. Forty-eight mortar cubes, six taken from each batch during construction, were tested in compression according to CSA A179-14 (CSA 2014c) and resulted in an average compressive strength of 23.3 MPa (c.o.v. = 8.7%). Premixed fine grout with weight proportions 1.0:0.04:3.9:0.85 (portland cement: lime: dry sand: water) was used to achieve a slump of 250 mm. The average grout compressive strength was 19.7 MPa (c.o.v. = 15.7%) based on testing 30 grout cylinders complying with ASTM CI019-08 (ASTM 2008b) and CSA A179-14 (CSA 2014c). Twenty-four fully grouted masonry prisms that were four blocks high by one block long (264.0 mm high × 126.6 mm long × 63.3 mm thick) were constructed and grouted during each construction stage. These prisms were later tested, in accordance with CSA S304-14 (CSA 2014a) and the specified masonry strength, f'_m and average compressive strength for the prisms, f_{av}, were 11.1 MPa and 17.0 MPa, respectively (c.o.v. =21.1%). These values were multiplied by a correction factor of 0.95 to account for the height-to-thickness ratio of the prisms, as specified in CSA S304-14 (CSA 2014a).

Tension tests were carried out, according to CSA G30.18-09 (CSA 2014d), on the scaled reinforcement bars D7 (used as vertical wall reinforcement), D4 (used in the slabs), and W1.7 (used as horizontal wall reinforcement) to determine their yield and ultimate strengths. The average yield strength of the D7 bars (45 mm^2) was 457 MPa (c.o.v. = 6.5%), whereas the average yield strengths of the D4 bars (26 mm^2) and W1.7 bars (11 mm^2) were 487 MPa (c.o.v. = 3.5%) and 675 MPa (c.o.v. = 12.2%), respectively. Heerema et al. (2015) provide more details about the model reinforcement and concrete masonry unit properties, while Harris and Sabnis (1999) present guidelines pertaining to the use of scaled bars and scaled concrete masonry units in RM test models.

All of the building walls were constructed by an experienced mason in a running bond pattern with face shell mortar bedding following common North American practice. The webs of the masonry units were saw cut to a depth of 10 mm to generate notches to accommodate the horizontal wall reinforcement. This construction detail ensured full grout encasement of the horizontal reinforcement along the entire length of all of the walls and throughout their courses.

The boundary elements at the wall ends ($W1_{IV}$, $W2_{IV}$, $W5_{IV}$, and $W8_{IV}$) were 130 mm in both of the wall's in-plane and out-of-plane directions. These dimensions were based on using two reduced-scale concrete blocks to form the boundary elements. As can be seen in Fig. 3.2(d), four vertical reinforcement bars were placed in two layers and confined with steel reinforcement stirrups in every course through the thickened wall ends. Stirrups were made with W1.7 bars and were located at the same level as the horizontal reinforcement of the walls for ease of construction. As such, stirrups had a spacing that ranged from $8.3\phi_v$ in Walls $W5_{IV}$ and $W8_{IV}$ to 11.2 ϕ_v in Walls $W1_{IV}$ and $W2_{IV}$, where ϕ_v is the vertical reinforcement bar diameter in each wall. This was considered acceptable based on the range of stirrup spacings that have been identified by previous researchers as enhancing the maximum strength, ultimate strain, and gradual strain softening behavior (Shedid et al. 2010; Banting 2013; El Ezz et al. 2015). Conversely, the horizontal reinforcement in the rectangular orthogonal walls ($W3_{IV}$, $W4_{IV}$, $W6_{IV}$, and $W7_{IV}$) formed 180° hooks around the outermost vertical reinforcement, with a 150-mm return leg that extended to the third last cell to provide an adequate development length, as shown in Fig. 3.2(e). Horizontal reinforcement was placed in every course in the first story and in every other course in the second story of the structure in all walls.

The construction was started first by installing the formwork for the square RC foundation with a thickness of 250 mm and placing the lower and upper reinforcement mesh. To avoid lap splices, the wall's vertical bars were tied under the bottom reinforcement mesh of the RC foundation and extended over the full building height (3,000 mm). Following the foundation pouring, the next step was the construction and grouting of the first seven courses (15 courses per story) of all walls of the first story. The remaining eight courses of all walls were then constructed and fully grouted. Once all walls in the first story were completed, a temporary formwork for the RC slab of the first story was set in place and a reinforcement mesh consisting of D4 bar every 150 mm was installed. The same steps were followed during the construction of the second story walls and the roof floor.

3.3.3 Test Setup, Instrumentation and Loading Protocol

The lateral cyclic displacement was applied at the second floor slab using a hydraulic actuator, with a capacity of 500 kN and a maximum cyclic stroke of 250 mm in both directions. Although it would have been desirable to apply this lateral displacement at the first and second floor slabs to simulate the seismic inertial forces, this would not only have complicated the test setup and loading control, but it also would not have facilitated direct comparison between *Building III* and *Building IV*, which is one of the main objectives of this chapter. The building rotation is permitted by the two swivel ends of the main actuator which was supported on a reaction steel frame as shown in Fig. 3.3. The effect of the main actuator on the slab out-of-plane rotation was minimized by using a secondary vertical actuator to support the weight of the main loading actuator. To ensure that the building slab was always under bearing when loading in either the push or the pull direction through the test, the actuator was attached to a stiff steel loading beam at the North side of the building (Beam A), shown in Fig. 3.3, which transferred the push lateral load when loading was in the positive direction. In addition, four high strength steel rods attached to another stiff steel beam (Beam B) at the South side of the building were used to transfer the pull lateral load from the actuator when loading was in the negative direction. Although these steel rods induced in-plane axial load on the second floor slab throughout the test, the same loading system was used for this test as in *Phase III* to allow for a direct comparison between both building responses.

Figure 3.4 shows the typical external and internal instrumentation used in the test setup to monitor the in-plane and out-of-plane wall displacements and strains during the test. The individual walls were instrumented with displacement potentiometers (label V) to monitor vertical wall deformations. In addition, the overall building displacements and rotations at the two floor slab levels were recorded using lateral displacement potentiometers (labels PA and PB). These measurements also facilitated determining the displacement demands of the different walls in the building throughout the loading history. As can be seen in Fig. 3.4, strain gauges (label S) were also used to monitor the initiation and extent of yielding of the outermost reinforcement.

To allow for a direct comparison between *Building III* (reported by Ashour et al. 2016) and *Building IV*, an identical loading scheme was followed in this study. Figure 3.5 shows the cyclic loading sequence that was adopted for the test, in which the building was subjected to 21 quasi-static fully-reversed cycles in total. Testing started by performing only one cycle at each displacement level up to *Cycle* 5, followed by repeating each cycle twice starting from *Cycle* 6 in order to capture any degradation in stiffness and/or strength at the same displacement level.

3.4 EXPERIMENTAL RESULTS

3.4.1 Load Displacement and Hysteretic Behavior

One of the objectives during the test program design stage was that *Building III* and *Building IV* would have approximately the same lateral load capacity. This was an important design criterion to facilitate quantifying the effect of the boundary elements on the overall building response when rectangular walls were directly replaced by end-confined walls and subjected to identical displacement demands. Figure 3.6 shows the lateral load-drift ratio relationship for *Building III* and *Building IV*. As can be seen in Fig. 3.6, the ultimate strength of *Building III*, $Q_{u\,III}$, was reached at 0.9% drift and was equal to 384 kN in the positive direction and 372 kN in the negative direction (Ashour et al. 2016), while *Building IV* reached a maximum lateral load capacity, $Q_{u\,IV}$, of 346 kN and 340 kN at 0.9% top drift during loading in the positive and negative directions, respectively. The small difference (less than 10% in either push or pull direction) in the ultimate strength between both buildings can be mainly attributed to the material variability associated with the construction during each building. Specifically, the average yield strengths for the main vertical reinforcement bars were 500 MPa versus 457 MPa ($\approx 10\%$) for *Building III* and *Building IV*, respectively.

Figure 3.6 also shows that the overall ultimate strength of *Building IV*, $Q_{u\,IV}$, is approximately 55% higher than the summation of the ultimate strength values of the walls aligned along the loading direction (i.e. $W1_{IV}$, $W2_{IV}$, $W5_{IV}$ and $W8_{IV}$), shown in Table 3.2. This indicates that these walls were no longer responding as ideal cantilevers as originally designed. This is mainly attributed to the influence of the diaphragm coupling on the system-level behavior, which restrained the wall in-plane rotations at the diaphragm levels and therefore increased the overall lateral load capacity of *Building IV*. Similar observations were reported for *Building III* by Ashour and El-Dakhakhni (2016). These observations highlight that neglecting the diaphragm coupling (MSJC 2013; CSA 2014a) may result possibly in undesirable failure modes. More specifically, the enhancement to the building strength was also accompanied by increased flexure/shear/sliding demands on the walls that were not accounted for during the wall design and reinforcement detailing according to the current codes and standards.

As can be seen in Fig. 3.6, the hysteretic loops for both buildings showed an almost symmetrical loading response in both directions, with thin loops indicating almost elastic response at initial stages of loading (up to 0.25%) and wider loops indicating more significant energy dissipation associated with the inelastic response at high drift ratio levels (up to 2.5%). The two buildings had very similar performance up to reaching the ultimate strength (at 0.9%). Beyond 0.9% drift, both buildings started to exhibit a combined stiffness and strength degradation. However, *Building IV* (with boundary elements) attained higher energy dissipation and less strength degradation, as shown in Fig. 3.6 and discussed in more detail subsequently.

3.4.2 Damage Sequence and Failure Modes

The test results, including failure modes and extent of building damage, are presented in this section. In total, 21 fully reversed loading cycles were applied to the building up to failure. For both buildings at the early loading stages (up to 0.60% drift), the orthogonal walls *W6* and *W7* showed horizontal bed joint cracks along the wall length at the first and second stories during loading in the positive direction and similar cracks were also observed in Walls *W3* and *W4* during loading in the negative direction. These cracks indicated that the orthogonal walls may have been acting as tension members for the walls aligned along the loading direction. At later stages of loading (from 0.90% drift), the orthogonal walls of both buildings started to experience diagonal shear cracks that might be attributed to the engagement of these walls to provide torsional resistance, especially after the yielding of the walls that were aligned along the loading direction. The main test observations, failure modes, and extent of damage associated with the walls aligned along the loading direction (Walls *W1, W2, W5,* and *W8*) during seven key cycles are presented in Table 3.3. This section discusses the similarities and discrepancies between the behavior of those walls in both buildings for comparison purposes.

Table 3.3 indicates that both buildings showed similar superficial cracks during *Cycle 1* (0.10%). In addition, neither *Building III* nor *Building IV* showed shear cracks in any of the walls by the end of this cycle. However, the first shear crack was observed by the end of *Cycle 2* (0.15%) in the first story of *Building IV*. As shown in Table 3.3, both buildings reached the yield strain of the outermost bars in both ends of Walls *W1, W2* and *W5* at the same drift demand (0.25%)

according to the strain gauge measurements. Table 3.3 also shows that the displacement demands within *Cycle 10* (1.50%) resulted in buckling and fracturing of *Building III* end bars. As such, *Building III* reached the failure criterion (degradation to less than 80% of strength) at this drift level. However, the boundary elements prevented the vertical wall reinforcement from fracturing, and also delayed crushing of the grout core, allowing *Building IV* to maintain a lateral resistance within 85% of its maximum ultimate strength, $Q_{u\,IV}$, at the same drift level. Later, by the end of *Cycle 12* (1.90%), the outermost reinforcement bars of *Building IV* experienced fracture, and the web crushed in the first story of Wall $W5_{IV}$, reducing *Building IV's* strength to 72% of $Q_{u\,IV}$.

At the end of *Cycle 14* (2.20%), *Building III* experienced complete face shell and grout spalling within the toes of Walls $W1_{III}$, $W2_{III}$, $W5_{III}$, and $W8_{III}$, followed by buckling of the outermost reinforcement bars and their eventual fracture as shown in Figs. 3.7(a, b, c, and d). As such, *Building III* experienced degradation to approximately 40% of its ultimate strength at 2.20% drift level. Walls $W1_{IV}$, $W2_{IV}$ and $W8_{IV}$ were able to maintain approximately 60% of the overall lateral capacity of *Building IV* at the same drift level, despite the evidence of extensive web crushing in the first story of Wall $W5_{IV}$, as shown in Fig. 3.7(e). This web crushing might be attributed to out-of-plane buckling instability of the vertical bars due to the absence of the ties at the web relative to those at the boundary elements (Maier and Thürlimann 1985). Moreover, the boundary element confinement prevented the two bars near the web from fracturing, so the face shells of these walls were not completely spalled-off from both ends as they had been in *Building III*, as shown in Figs. 3.7 (f, g and h). However, under increased displacement demands, these walls experienced crushing of the toes and completely spalling of the face shells, which was accompanied by sliding until the end of the test.

3.5 EFFECT OF BOUNDARY ELEMENTS ON THE BUILDING RESPONSE

3.5.1 Lateral Load Capacity and Displacement Characteristics

The envelopes of normalized load-drift ratio relationships for *Building III* and *Building IV* are presented in Fig. 3.8. The enhancement in displacement capabilities achieved by the boundary element walls is clear. For example, *Building III* (without boundary elements) reached 50% strength degradation at about 1.92% and 2.05% drift ratios during loading in the positive and negative directions, respectively (Ashour et al. 2016). Conversely, *Building IV* (with boundary elements) delayed 50% strength degradation to drift ratios of 2.55% in the positive direction and 2.70% in the negative direction. The small difference in the response between the push and the pull direction (less than 10% in either direction) might possibly be attributed to minor variability in material, workmanship and cumulative damage due to the cyclic loading, which is to be expected for such complex system.

3.5.2 Displacement Ductility

Displacement ductility quantification is key to comparing the RM walls' inelastic deformation capacities. In this study, the idealized displacement ductility, $\mu^{ep}{}_{\Delta 0.8u}$, is defined as the ratio of the displacement associated with a degradation to 80% of the maximum strength to the effective yield displacement of an equivalent elastic-perfectly-plastic system that provides equal energy under the idealized curve as the actual data up to 80% strength degradation (Tomaževič 1998). The initial stiffness for individual walls can be calculated as the secant stiffness at the first major crack that usually taken as the onset of yielding (Tomaževič 1998). However, in the case of a building composed of different walls, this procedure is more complex. Therefore, the variation of the stiffness along the ascending branch of the envelope of the building's inelastic load-displacement relationship was adopted to study the system-level ductility. Specifically, the point at which significant variation in stiffness was first recorded was considered to represent the yield point or the major crack point of the building as suggested by Tomaževič (1998). The stiffness of both buildings varied significantly at two loading points along the ascending branch. These two points were by the end of *Cycle 3* and *Cycle 4*, at which the stiffnesses of both buildings were approximately 76% and 69%, respectively, of the stiffnesses that were measured during the previous loading cycle. As such, two approaches were chosen in this chapter to define the point of major crack. *Approach 1* considered *Cycle 3*, while *Cycle 4* was used in *Approach 2*. *Approach 1* and *Approach 2* were used to calculate the idealized displacement ductility, $\mu^{ep1}{}_{\Delta 0.8u}$ and $\mu^{ep2}{}_{\Delta 0.8u}$, respectively. In addition, idealized displacement ductility values corresponding to

50% strength degradation, $\mu^{ep}{}_{\Delta 0.5u}$, were also calculated for both buildings to facilitate comparison, and the results of the two approaches are summarized in Table 3.4 and shown in Fig. 3.9 for *approach 1* only. As can be seen in Fig. 3.9 and Table 3.4, increases of 20% and 40% in $\mu^{ep}{}_{\Delta 0.8u}$ and $\mu^{ep}{}_{\Delta 0.5u}$, respectively, were achieved by *Building IV* with respect to *Building III*, regardless the approach that was used. This indicates the effect of boundary elements in increasing the inelastic deformation capacity of *Building IV* when compared to that of *Building III*, thereby increasing the energy dissipation and leading to enhanced overall seismic performance. Although the structural walls with boundary elements in *Building IV* were constructed with the same prescriptive detailing requirements as were adopted by Shedid et al. (2010), the enhancement in the system-level performance of *Building IV* is not as great as the enhancement in component-level performance that was reported by Shedid et al. (2010). This is attributed in part to the fact that *Building IV* had walls with different aspect ratios ranged from 1.4 to 3.6. In addition, the building twist effects amplified the demand variations in the displacement, and thus the ductility, of the different wall components within the building throughout the loading history and thus the full ductility capacities of the walls were not mobilized. Thus, although the system-level building ductility capacity was influenced by the component-level wall ductility capacity, the two ductility capacities were not equivalent. This difference between component- and system-level ductility is expected for a building where all walls do not reach their ductility capacity simultaneously (Heerema et al. 2015). This indicates the importance of system-level studies conducted in this study since there will always be variations in component-level performances versus system-level performances comprising of the same components.

3.5.3 Effective Stiffness Degradation

The elastic or equivalent cracked stiffness is normally used to estimate the fundamental period of a structure for force-based design. However, an effective secant stiffness, determined from the load-displacement response of the inelastic structure at the desired level of top displacement, has also been used for displacement-based design (Priestley et al. 2007). Therefore, to assess the stiffness degradation of the two buildings as the displacement increases, the effective secant stiffness was calculated in both directions of loading as the ratio between the lateral resistance and the corresponding top lateral building displacement (ASCE 2013). Figure 3.10 presents the variation of the effective secant stiffness, in both loading directions, with respect to the top drift levels for both buildings.

As can be seen from Fig. 3.10, the initial stiffness of the two buildings is almost the same, where the difference is less than 5% in either positive or negative direction. This is mainly attributed to the lower reinforcement ratio used in the boundary element walls to maintain the same capacities of their rectangular counterparts, and also to the significant reduction in the compression zone depth leading to a lower cracked stiffness (Shedid et al. 2010). When a force-based design approach is adopted, the seismic elastic design force for a building is based on the elastic stiffness of the lateral load resisting elements. As such, having nearly the same stiffness for both buildings, and thus nearly the same fundamental period, implies that their design forces should also be nearly the same. However, buildings with boundary elements could potentially be designed for a reduced lateral force because of their higher displacement ductility (Miranda and Bertero 1994).

3.5.4 Energy Dissipation

Energy dissipation through hysteretic damping, E_d, is an important aspect in seismic design because it reduces the amplitude of the seismic response and, therefore, reduces the ductility and strength demands of the structure. In addition, FEMA P440A (FEMA 2009) highlighted the importance of the hysteretic energy demand imposed on the system at different performance levels, whereas hysteretic models that incorporate stiffness and strength degradation (e.g. Park et al. 1987; Mostaghel 1999; Sivaselvan and Reinhorn 2000; Ibarra et al. 2005) typically specify the reduction in stiffness and strength as a function of the total energy dissipation. Moreover, ASCE 41-13 recommends more investigation to determine the seismic performance characteristics of structural systems until the Collapse Prevention performance level. As such, reporting the seismic parameters, including the energy dissipation, at the post peak stage (even for more than 50% strength degradation) would be beneficial to provide guidelines about the seismic design of such new systems. The energy dissipation, E_d, in this study is represented as the area enclosed by the load-displacement curve passing through the envelope values, as suggested by Hose and Seible (1999).

Figure 3.11 shows the energy dissipation with respect to the roof drift levels for both buildings. The figure illustrates that the energy dissipation was low for both buildings during the loading stages before significant inelastic deformation in the masonry and reinforcement took place. The energy dissipation at the onset of reinforcement bar yielding, E_y, was very similar for both buildings. At higher drift levels, the energy dissipation increased significantly compared to early stages of loading. The figure shows that the energy dissipation values at 2.20% and 3.50% drift were 17% and 25% higher for *Building IV*, respectively, than those for *Building III*. The results clearly show that significantly more energy dissipation is to be expected from RM buildings with boundary elements compared to those without, resulting in reduced seismic demands due to the increased damping after yield.

3.5.5 Building Twist Response

Building III and *Building IV* each had four walls aligned with the loading direction, placed asymmetrically to result in an eccentricity between the center of rigidity, C_R, and the center of mass, C_M, at the roof level. This eccentricity was approximately 20% and 15% of the building width for *Buildings III* and *IV*, respectively, evaluated based on elastic analysis. In addition, both buildings contained four other orthogonal walls placed symmetrically around the building floor center of mass, C_M, to enhance the torsional response by engaging at higher building twist levels to provide torsional resistance, especially after yielding within the walls located along the main direction of loading. However, Figure 3.12 shows that twist angle of *Building IV*, θ_{IV}, was much lower than that of *Building III*, θ_{III}, at the same loading level during testing. For example, the twist angles of *Building IV*, at 0.90% drift ratio, were 47% and 54% lower than those of *Building III* in the positive and negative directions of loading, respectively. To explain this, the initial torsional stiffness was calculated for both buildings according to Priestley et al. (2007), showing that *Building IV* had 29% higher torsional stiffness than *Building III* because of the higher stiffness of the walls with boundary elements ($W1_{IV}$, $W2_{IV}$, and $W5_{IV}$) compared to the rectangular walls ($W1_{III}$, $W2_{III}$, and $W5_{III}$), together with the slightly higher stiffness of the C-shaped wall ($W8_{III}$) compared to the wall with boundary elements ($W8_{IV}$). For the same reasons, the eccentricity of *Building IV* was 22% lower than for *Building III*. The combined effect is that the twist angle of *Building IV* would be expected to be approximately 60% of that of *Building III* based on the initial stiffnesses. As can be seen in Fig. 3.13, the ratio of the twist angle of *Building IV*, θ_{IV}, to that of *Building III*, θ_{III}, was indeed 60% or less not only initially, but also after the walls yielded.

3.6 CONCLUSIONS

This chapter evaluated the experimental results of the fourth phase of a multi-phase research program that focuses on the system-level response of RM buildings with boundary elements under simulated seismic loading. In this respect, *Building IV* was designed within this study to have the same lateral resistance as *Building III*, which is a previously tested building with RM shear walls, to allow for direct comparison. However, the conventional RM shear walls located along the main direction of loading in *Building III* were replaced by RM shear walls with confined boundary elements. The individual walls in *Building IV* were designed to have the same flexural strength as those within *Building III*. *Building IV* was then tested under quasi-static cyclic displacement-controlled loading up to failure. The damage sequence, hysteretic behavior, displacement ductility, stiffness degradation, energy dissipation and torsional resistance of the two buildings were presented to assess the effect of boundary elements on the building performance.

The response of both buildings was almost symmetrical for both directions of loading, as was evident from the load-displacement relationship. The test results also showed that the two buildings had almost the same capacity and the same elastic stiffness as each other. In addition, as the walls within each building did not behave as cantilevers (as they had originally been designed), the diaphragm-wall coupling resulted in increasing the lateral capacity of both buildings. Enhancements in ultimate displacements and ductility were attained.

For example, the idealized ductilities of *Building IV* were at least 20% and 40% higher than those of *Building III* at a post-peak resistance equal to 80% and 50% of the maximum capacity, respectively. Moreover, the two buildings showed a similar initial stiffness and therefore their design forces should also be nearly the same, when force-based design approach is adopted. The results also showed that *Building IV* dissipated more energy than *Building III*: the energy dissipated by *Building IV* was 17% and 25% higher than that by *Building III* at 2.20% and 3.50% drift levels, respectively. This is expected to lead to reduced seismic demands on buildings with boundary elements.

RM shear walls with boundary elements can be easily achieved in construction and possibly without requiring major changes to architectural practices. Moreover, the reported test results illustrate the higher ductility and energy dissipation capacities of RM shear walls with boundary elements relative to conventional RM shear walls, as well as the delayed strength degradation. However, the experimental results in this chapter were limited to RM shear wall buildings with a specific configuration of boundary elements subjected to reversed cycles of applied top displacement. Additional experimental tests, considering several loading patterns and protocols, are still needed to develop a better understanding of the behavior of RM buildings with boundary elements that will, subsequently, facilitate adoption of this new system within the next editions of the Masonry Standards Joint Committee and the Canadian Standards Association masonry design codes.

3.7 ACKNOWLEDGMENTS

The financial support for this project was provided through the Natural Sciences and Engineering Research Council (NSERC) of Canada. Support was also provided by the McMaster University Centre for Effective Design of Structures (CEDS), funded through the Ontario Research and Development Challenge Fund (ORDCF) of the Ministry of Research and Innovation (MRI). Provision of mason time by the Ontario Masonry Contractors Association (OMCA) and the Canada Masonry Design Centre (CMDC) is appreciated. The provision of the scaled blocks through a grant from the Canadian Concrete Masonry Producers Association (CCMPA) is gratefully acknowledged.

3.8 NOTATION

The following symbols are used in this chapter:

A_g	=	Gross cross-sectional area;
C_M	=	Building floor center of mass;
C_R	=	Building center of rigidity;
E_d	=	Energy dissipation;
E_m	=	Masonry Young's modulus;
E_y	=	Energy dissipation at yield;
f_{av}	=	Average compressive strength of prisms;
f'_m	=	Specified masonry strength;
h	=	Wall height;
I_g	=	Gross cross section moment of inertia;
K	=	Cross section gross stiffness;
Q_u	=	Ultimate strength;
Qu_{III}	=	Ultimate strength of *Building III*;
Qu_{IV}	=	Ultimate strength of *Building IV*;
Q_y	=	Yield strength;
V_s	=	Sliding strength;
V_u	=	Shear strength;
$\mu^{ep}_{\Delta 0.8u}$	=	Idealized displacement ductility at 80% strength degradation;
$\mu^{ep}_{\Delta 0.5u}$	=	Idealized displacement ductility at 50% strength degradation;
ρ_{h1}	=	Horizontal steel reinforcement ratio in the first story;
ρ_{h2}	=	Horizontal steel reinforcement ratio in the second story;
ρ_v	=	Vertical steel reinforcement ratio;
ϕ_h	=	Horizontal reinforcement nominal bar diameter;
ϕ_v	=	Vertical reinforcement nominal bar diameter;
δ	=	Roof drift ratio at building center of mass;
θ_{III}	=	Twist angle of *Building III*;
θ_{IV}	=	Twist angle of *Building IV*.

3.9 REFERENCES

Abrams, D. (1986). “Measured hysteresis in a masonry building system.” *Proc., 3rd U.S. Conference on Earthquake Engineering*, Charleston, SC.

Ahmadi, F., Hernandez, J., Sherman, J., Kapoi, C., Klingner, R., and McLean, D. (2014). "Seismic performance of cantilever-reinforced concrete masonry shear walls." *J. of Struct. Eng.*, 10.1061/ (ASCE) ST.1943-541X.0000941, 04014051.

ASCE 41-13 (2013). “Seismic Rehabilitation of Existing Buildings.” *American Society of Civil Engineers*, Reston, Virginia.

Ashour, A., and El-Dakhakhni, W. (2016). “Influence of floor diaphragm–wall coupling on the system-level seismic performance of an asymmetrical reinforced concrete block building.” *J. of Struct. Eng.*, 04016071.

Ashour, A., El-Dakhakhni, W., and Shedid, M. (2016). “Experimental evaluation of the system-level seismic performance and robustness of an asymmetrical reinforced concrete block building.” *J. of Struct. Eng.*, 04016072.

ASTM C140-08 (2008a). “Standard test methods for sampling and testing concrete masonry units and related units.” West Conshohocken, PA.

ASTM CI019-08 (2008b). “Standard test method for sampling and testing grout.” West Conshohocken, PA.

Banting, B. R. (2013). “Seismic performance quantification of concrete block masonry structural walls with confined boundary elements and development of the normal strain-adjusted shear strength expression (NSSSE).” Ph.D.

thesis, McMaster Univ., Hamilton, Canada

Banting, B. and El-Dakhakhni, W. (2012). ”Force-and displacement-based seismic performance parameters for reinforced masonry structural walls with boundary elements.” *J. Struct. Eng*., 10.1061/(ASCE)ST.1943-541X.0000572, 1477–1491.

Banting, B. and El-Dakhakhni, W. (2014). ”Seismic performance quantification of reinforced masonry structural walls with boundary elements.” *J. Struct. Eng*., 10.1061/(ASCE) ST.1943-541X.0000895, 04014001.

Brunner, J.D. (1994). “Shear strength of reinforced masonry walls.” M.Sc. thesis, Department of Civil, Environmental, and Architectural Engineering, University of Colorado, Boulder, CO.

Canadian Standards Association (CSA). (2014a) “Design of masonry structures.” CSA S304-14, Mississauga, Canada.

Canadian Standards Association (CSA). (2014b). “CSA Standards on concrete masonry units.” CSA A165-14, Mississauga, Ontario, Canada.

Canadian Standards Association (CSA). (2014c). “Mortar and grout for unit masonry.” CSA A179-14, Mississauga, Canada.

Canadian Standards Association (CSA). (2014d). “Carbon steel bars for concrete reinforcement.” CSA G30.18-09, Mississauga, ON, Canada.

Cohen, G. L., Klinger, R. L., Hayes Jr., J. R., and Sweeny, S. C. (2004). “Seismic evaluation of low-rise reinforced masonry buildings with flexible diaphragms I. Seismic and quasi-static testing.” *Earthquake Spectra*, 20(3), 779-801.

Dhanasekar, M., and Shrive, N., G. (2002). “Strength and deformation of confined and unconfined grouted masonry.” *ACI Struct. J.*, 99(6), 819-826.

El Ezz, A. A., Seif Eldin, H. M., and Galal, K. (2015). “Influence of confinement reinforcement on the compression stress–strain of grouted reinforced concrete block masonry boundary elements”. *Structures*, 2, 32-43, Elsevier.

FEMA. (2009). “Effect of strength and stiffness degradation on seismic response.” *FEMA P440A*, Washington, DC.

Harris, H., and Sabnis, G. (1999). *Structural modeling and experimental techniques*, 2nd Ed., CRC Press, London.

Hart, G. C., Sajjad, N., Kingsley, G. R., and Noland, J. L. (1989). “Analytical stress-strain curves for grouted concrete masonry.” *The Masonry Society Journal*, 8(1), 21-34.

Heerema, P., Shedid, M., Konstantinidis, D., and El-Dakhakhni, W. (2015). “System-level seismic performance assessment of an asymmetrical reinforced concrete block shear wall building.” *J. of Struct. Eng.*, 141(12), 04015047.

Hose, Y. and Seible, F. (1999), "Performance evaluation database for concrete bridge components, and systems under simulated seismic loads." PEER report 1999/11, *Pacific Earthquake Engineering Research Center*, College of Engineering, University of California, Berkley, U.S.A.

Hughes, K. J. (2010). “Behaviour of reduced-scale reinforced concrete masonry shear walls and components." M.Sc. thesis, McMaster Univ., Hamilton, Canada.

Ibarra, L. F., Medina, R. A., and Krawinkler, H. (2005). "Hysteretic models that incorporate strength and stiffness deterioration." *Earthquake engineering and structural dynamics*, 34(12), 1489-1511.

Ibrahim, K.S and Sutter, G.T. (1999), "Ductility of concrete masonry shear walls subjected to cyclic loading." *Proc., of the 8th North American Masonry Conference*, Austin, TX.

Maier, J., and Thürlimann, B. (1985). Bruchversuche an Stahlbetonscheiben. *Bericht / Institut für Baustatik und Konstruktion*, ETH Zürich, Nr. 8003-1.

Masonry Standards Joint Committee. (MSJC). (2013). "Building code requirements and specifications for masonry structures." *TMS 402-13/ ACI 530-13/ASCE 5-13*, the Masonry Society, American Society of Civil Engineers, Boulder, New York/American Concrete Institute, and Detroit, USA.

Mayes, R. L., Omote, Y. and Clough, R. W. (1976). *Cyclic shear tests of masonry piers Volume 1: Test Results*. Report No. UCB/EERC-76-8, Earthquake Engineering Research Center, University of California Berkeley, USA.

Miranda, E., and Bertero, V. (1994). "Evaluation of strength-reduction factors for earthquake-resistant design." *Earthquake Spectra*, 10(2), 357-379.

Mostaghel, N. (1999). "Analytical description of pinching, degrading hysteretic systems." *J. Eng. Mech.*, 125(2), 216-224.

Park, Y. J., Reinhorn, A.M., and Kunnath, S.K. (1987). *IDARC: inelastic damage analysis of reinforced concrete frame, shear-wall, structures*, Tech. Rep. NCEER-87-0008, State University of New York at Buffalo, Buffalo, New York.

Priestley, M., J., N. (1976). *Cyclic testing of heavily reinforced concrete masonry shear walls*. Research Report 76-12, University of Canterbury, Christchurch, New Zealand.

Priestley, M., J., N. and Bridgeman, D., O. (1974). "Seismic resistance of brick masonry walls." *Bulletin of the New Zealand National Society for Earthquake Enginee*ring, 7(4), 167-187.

Priestley, M. J. N., and Elder, D. M. (1982). "Cyclic loading tests of slender concrete masonry shear walls." *Bulletin of the New Zealand National Society for Earthquake Engineering*, 15(1), 3-21.

Priestley, M., J., N., and Elder, D., M. (1982). *Seismic Behaviour of Slender Concrete Masonry Shear Walls*. Research Report, University of Canterbury, Christchurch, New Zealand.

Priestley, N., Calvi, G., and Kowalsky, M. (2007). *Displacement-based seismic design of structures*, IUSS, Pavia, Italy.

Seible, F., Hegemier, G., Priestley, M. J. N., Kingsley, G., Igarashi, A., and Kurkchubasche A. (1993). "Preliminary results from the TCCMAR 5-story full scale reinforced masonry research building test." *Masonry Society Journal*, 12(1), 53-60.

Seible, F., Priestley, M. J. N., Kingsley, G., and Kurkchubasche A. (1994). “Seismic response of full scale five story reinforced masonry building.” *J. Struct. Eng.*, (120)3, 925-946.

Shedid, M., Drysdale, R., and El-Dakhakhni, W. (2008). “Behaviour of fully grouted reinforced concrete masonry shear walls failing in flexure: Experimental results.” *J. Struct. Eng*., 134(11), 1754–1767.

Shedid, M. T., El-Dakhakhni, W. W., and Drysdale, R. G. (2010). “Alternative strategies to enhance the seismic performance of reinforced concrete-block shear wall systems.” *J. Struct. Eng*., 136(6), 676-689.

Sivaselvan, M. V., and Reinhorn, A. M. (2000). “Hysteretic models for deteriorating inelastic structures.” *J. Eng. Mech.*, 126(6), 633-640.

Siyam, M., El-Dakhakhni, W., Shedid, M., and Drysdale, R. (2015). "Seismic response evaluation of ductile reinforced concrete block structural walls. I: experimental results and force-based design parameters." *J. Perform. Constr. Facil.* , 10.1061/(ASCE)CF.1943-5509.0000794, 04015066.

Stavridis, A., Ahmadi F., Mavros M., Koutromanos I., Hernández J., Rodríguez J., Shing P. B., and Klingner R. E. (2011). “Shake-table tests of a 3-story, full-scale masonry wall system.” Proc., *ACI Masonry Seminar*, Dallas, TX.

Tomaževič, M., and Weiss, P. (1994). “Seismic behavior of plain- and reinforced-masonry buildings.” *J. Struct. Eng*., 120(2), 323-338.

Tomaževič, M. (1998). "Earthquake-Resistant Design of Masonry Buildings." *Imperial College Press*, London, UK.

Voon, K.C. and Ingham, J.M. (2006), "Experimental in-plane shear strength investigation of reinforced concrete masonry walls." *J. Struct. Eng*., 132(3), 400-408.

Zonta, D., Zanardo, G., and Modena, C. (2001). "Experimental evaluation of the ductility of a reduced-scale reinforced masonry building." *Materials and Structures,* 34, 636-644.

Table 3.1 Wall Details and Configurations

<table>
<tr><th rowspan="2">Wall</th><th rowspan="2">Alignment relative to loading direction</th><th rowspan="2">Type</th><th rowspan="2">Height (mm)</th><th rowspan="2">Length (mm)</th><th colspan="2">Vertical reinforcement</th><th colspan="3">Horizontal reinforcement</th><th rowspan="2">Aspect ratio</th></tr>
<tr><th>Φ_v (mm)</th><th>ρ_v (%)</th><th>Φ_h (mm)</th><th>ρ_{h1} (%)</th><th>ρ_{h2} (%)</th></tr>
<tr><td>$W1_{IV}$ and $W2_{IV}$</td><td rowspan="3">Aligned</td><td rowspan="3">Boundary elements</td><td rowspan="4">2160</td><td>598</td><td>5.6</td><td>0.40</td><td>3.8</td><td rowspan="4">0.26</td><td rowspan="4">0.14</td><td>3.6</td></tr>
<tr><td>$W5_{IV}$</td><td rowspan="2">1533</td><td>7.6</td><td>0.44</td><td>3.8</td><td rowspan="2">1.4</td></tr>
<tr><td>$W8_{IV}$</td><td>7.6</td><td>0.59</td><td>3.8</td></tr>
<tr><td>$W3_{IV}$, $W4_{IV}$, $W6_{IV}$ and $W7_{IV}$</td><td>Orthogonal</td><td>Rectangular</td><td>465</td><td>7.6</td><td>0.60</td><td>3.8</td><td>4.7</td></tr>
</table>

Table 3.2 Summary of Walls Lateral Load Strengths

<table>
<tr><th rowspan="2">Wall</th><th rowspan="2">Alignment relative to loading direction</th><th rowspan="2">Type</th><th colspan="2">Flexural Strength</th><th>Shear Strength</th><th>Sliding Strength</th></tr>
<tr><th>Q_y (kN)</th><th>Q_u (kN)</th><th>Vu (kN)</th><th>Vs (kN)</th></tr>
<tr><td>$W1_{IV}$ and $W2_{IV}$</td><td rowspan="3">Aligned</td><td rowspan="3">Boundary elements</td><td>11.6</td><td>14.4</td><td>43.2</td><td>110.2</td></tr>
<tr><td>$W5_{IV}$</td><td>72.2</td><td>83.7</td><td>110.7</td><td>244.8</td></tr>
<tr><td>$W8_{IV}$</td><td>85.5</td><td>106.1</td><td>111.1</td><td>318.3</td></tr>
<tr><td>$W3_{IV}$, $W4_{IV}$, $W6_{IV}$ and $W7_{IV}$</td><td>Orthogonal</td><td>Rectangular</td><td>5.2</td><td>7.8</td><td>33.5</td><td>84.1</td></tr>
</table>

Table 3.3 Damage Sequence of *Building III* and *Building IV*

Cycle number and drift level	***Building III****	***Building IV***
Cycle 1 (0.10% Drift)	Horizontal hair cracks at the interface between the foundation and the walls aligned along the loading direction (Walls *W1*, *W2*, *W5* and *W8*).	
Cycle 2 (0.15% Drift)	Horizontal flexural cracks in the first story (Walls $W1_{III}$, $W2_{III}$, $W5_{III}$, and $W8_{III}$)	• Horizontal flexural cracks in the first story (Walls $W1_{IV}$, $W2_{IV}$, $W5_{IV}$, and $W8_{IV}$) • Diagonal shear crack in the first story (Wall $W5_{IV}$)
Cycle 3 (0.25% Drift)	• Yielding of the outermost bar in both ends (Walls $W1_{III}$, $W2_{III}$, *and* $W5_{III}$) • Diagonal shear crack in the first story (Walls $W1_{III}$, $W2_{III}$, $W5_{III}$, and $W8_{III}$)	• Yielding of the outermost bar in both ends (Walls $W1_{IV}$, $W2_{IV}$, and $W5_{IV}$) • Diagonal shear crack in the first story (Walls $W1_{IV}$, $W2_{IV}$ *and* $W8_{IV}$) • Diagonal shear crack in the second story (Wall $W5_{IV}$)
Cycle 6 (0.90% Drift)	Diagonal shear crack in the second story (Wall $W8_{III}$)	Extensive diagonal shear cracks in the first and second story (Wall $W5_{IV}$)
Cycle 10 (1.50% Drift)	• Buckling and fracturing of the outermost bars (Walls $W1_{III}$, $W2_{III}$, $W5_{III}$ and $W8_{III}$) • Spalling-off the first course (Wall $W5_{III}$)	Extensive flexural cracks in the first story (Walls $W1_{IV}$, $W2_{IV}$ *and* $W8_{IV}$)
Cycle 12 (1.90% Drift)	Spalling-off the first course (Walls $W1_{III}$, $W2_{III}$ and $W8_{III}$)	• Buckling and fracturing of the outermost bars (Walls $W1_{IV}$ *and* $W2_{IV}$) • Spalling-off the first course (Walls $W1_{IV}$ and $W2_{IV}$) • Web crushing in the first story (Wall $W5_{IV}$)
Cycle 14 (2.20% Drift)	Complete face shell and grout spalling (Walls $W1_{III}$, $W2_{III}$, $W5_{III}$ and $W8_{III}$)	Partial face shell and grout spalling (Walls $W1_{IV}$, $W2_{IV}$ and $W8_{IV}$)

*Based on data from Ashour et al. (2016)

Table 3.4 Summary of Displacement Ductilities

Building	Direction	Degradation to 80% of the Strength					Degradation to 50% of the Strength				
		Δ_{ye1} (%)	Δ_{ye2} (%)	$\Delta^{e}_{0.8u}$ (%)	$\mu^{ep1}_{\Delta 0.8u}$	$\mu^{ep2}_{\Delta 0.8u}$	Δ_{ye1} (%)	Δ_{ye2} (%)	$\Delta^{e}_{0.5u}$ (%)	$\mu^{ep1}_{\Delta 0.5u}$	$\mu^{ep2}_{\Delta 0.5u}$
Building III	Push	0.32	0.49	1.40	4.37	2.85	0.29	0.44	1.89	6.51	4.29
	Pull	0.31	0.48	1.43	4.61	2.98	0.28	0.42	2.05	7.32	4.88
Building IV	Push	0.30	0.46	1.59	5.30	3.45	0.26	0.38	2.37	9.11	6.24
	Pull	0.30	0.46	1.66	5.54	3.61	0.24	0.36	2.50	10.41	6.94

a)

b)

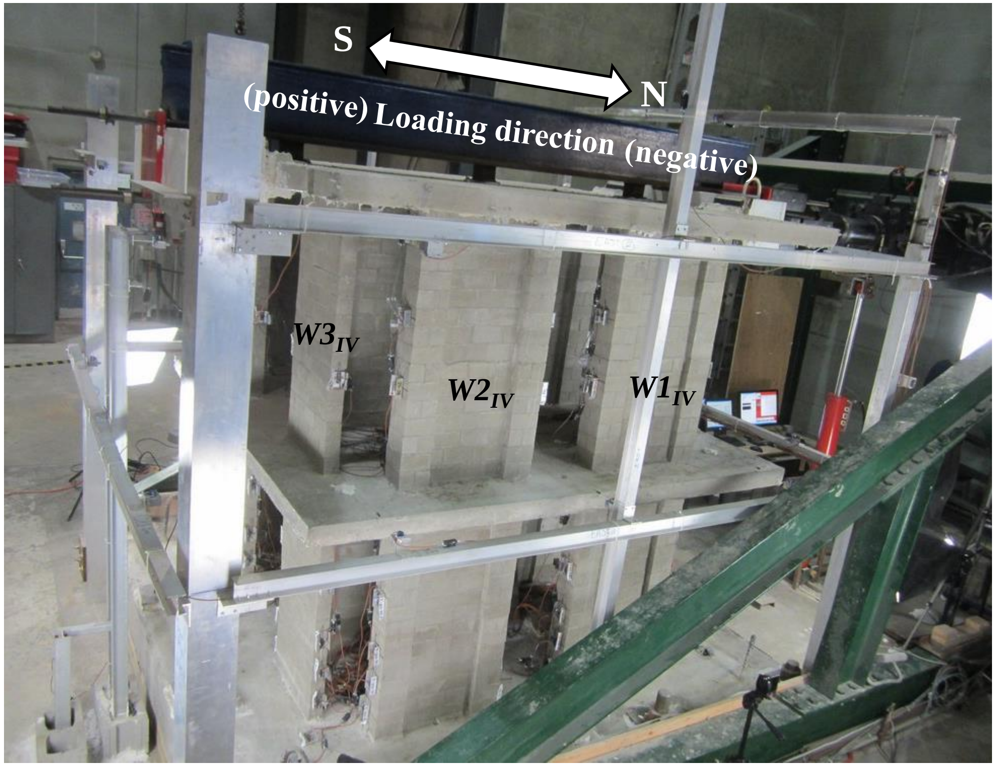

Fig. 3.1: Building IV configuration; a) 3-D view from South direction; b) 3-D view from East direction.

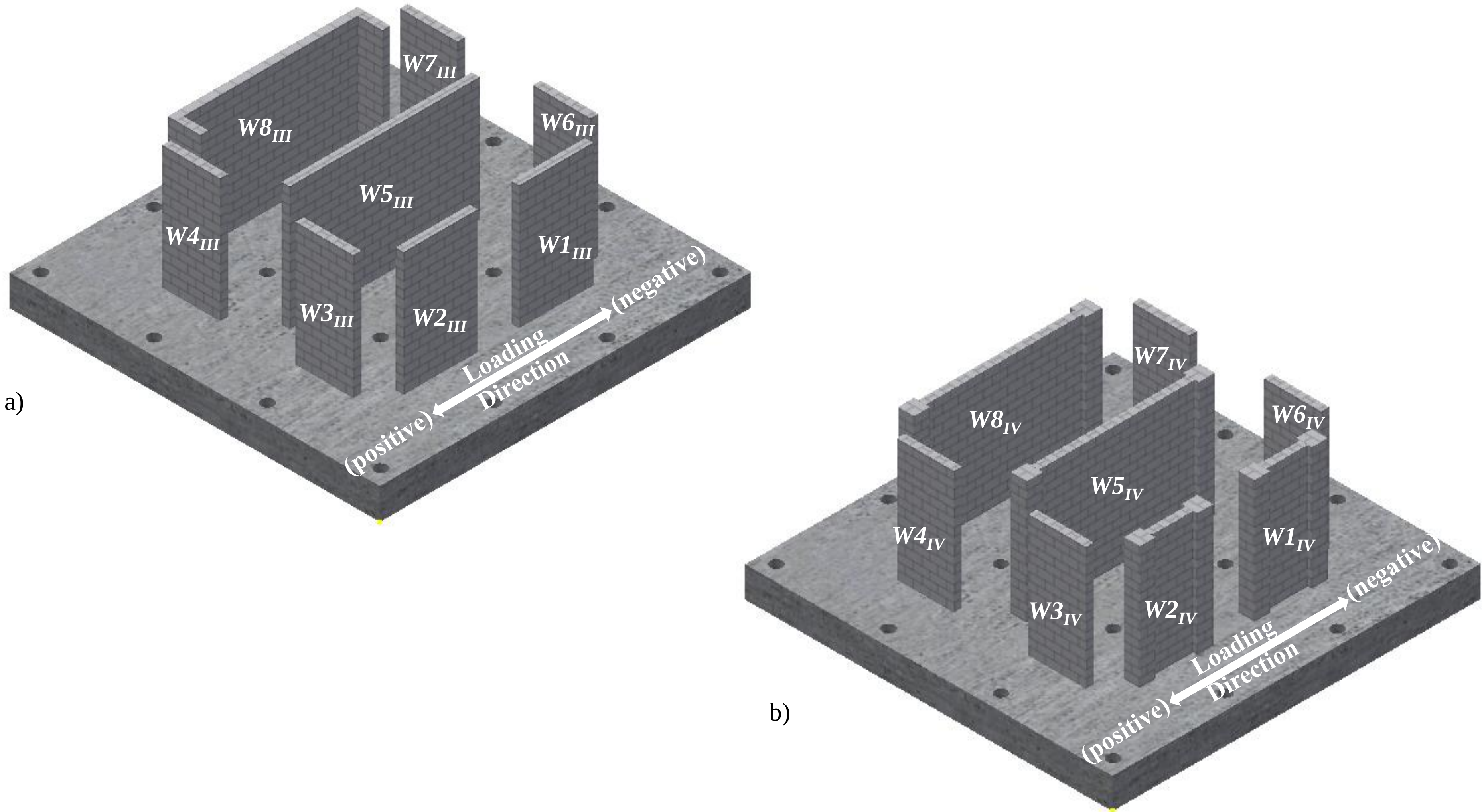

Fig. 3.2: Building configuration;

a) 3-D view for 1st story (*Building III*); b) 3-D view for 1st story (*Building IV*).

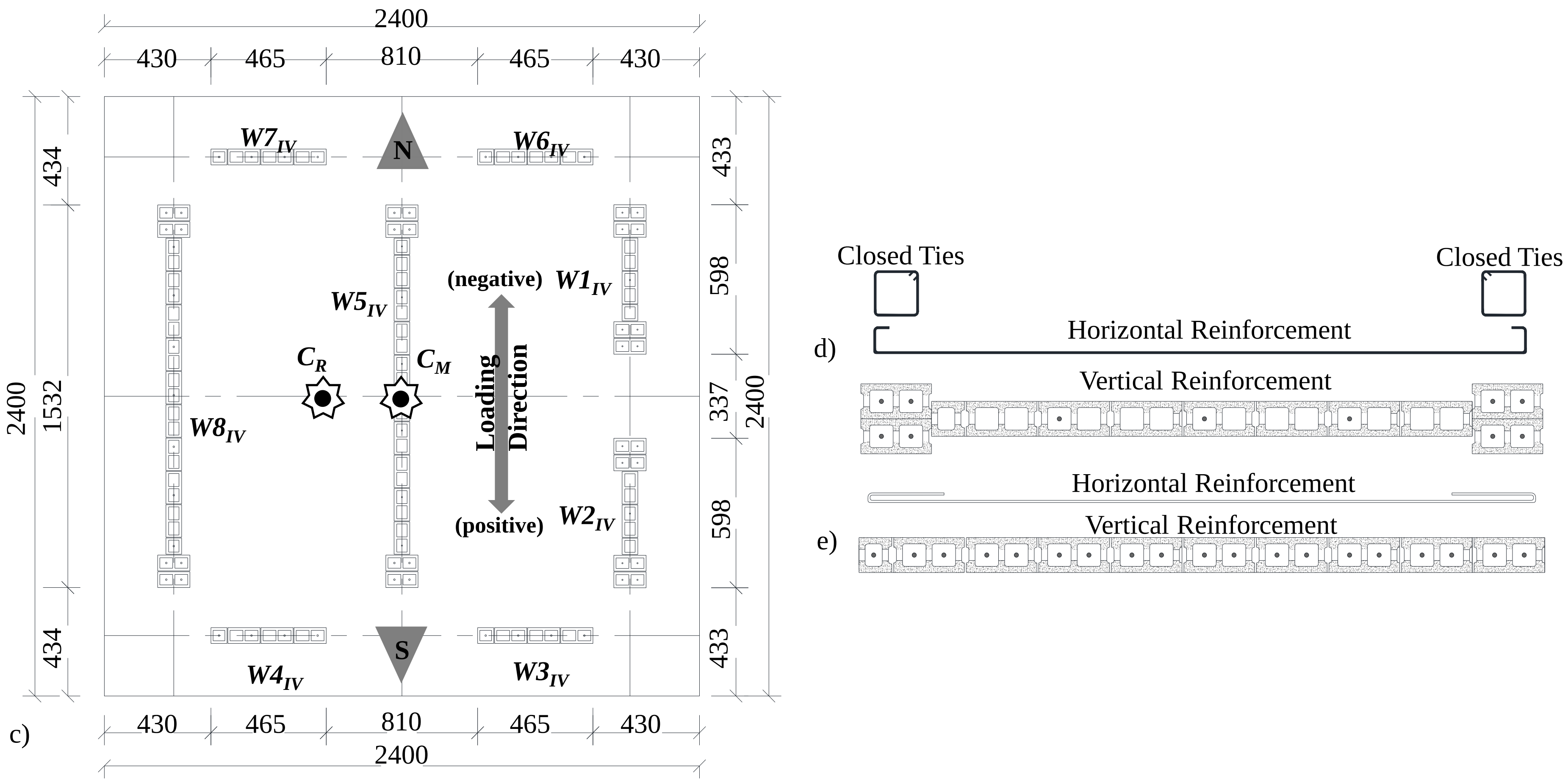

Fig. 3.2 (cont.): Building configuration; c) Typical plan (*Building IV*), all dimensions are in (mm);

d) Wall with boundary elements; e) Rectangular wall.

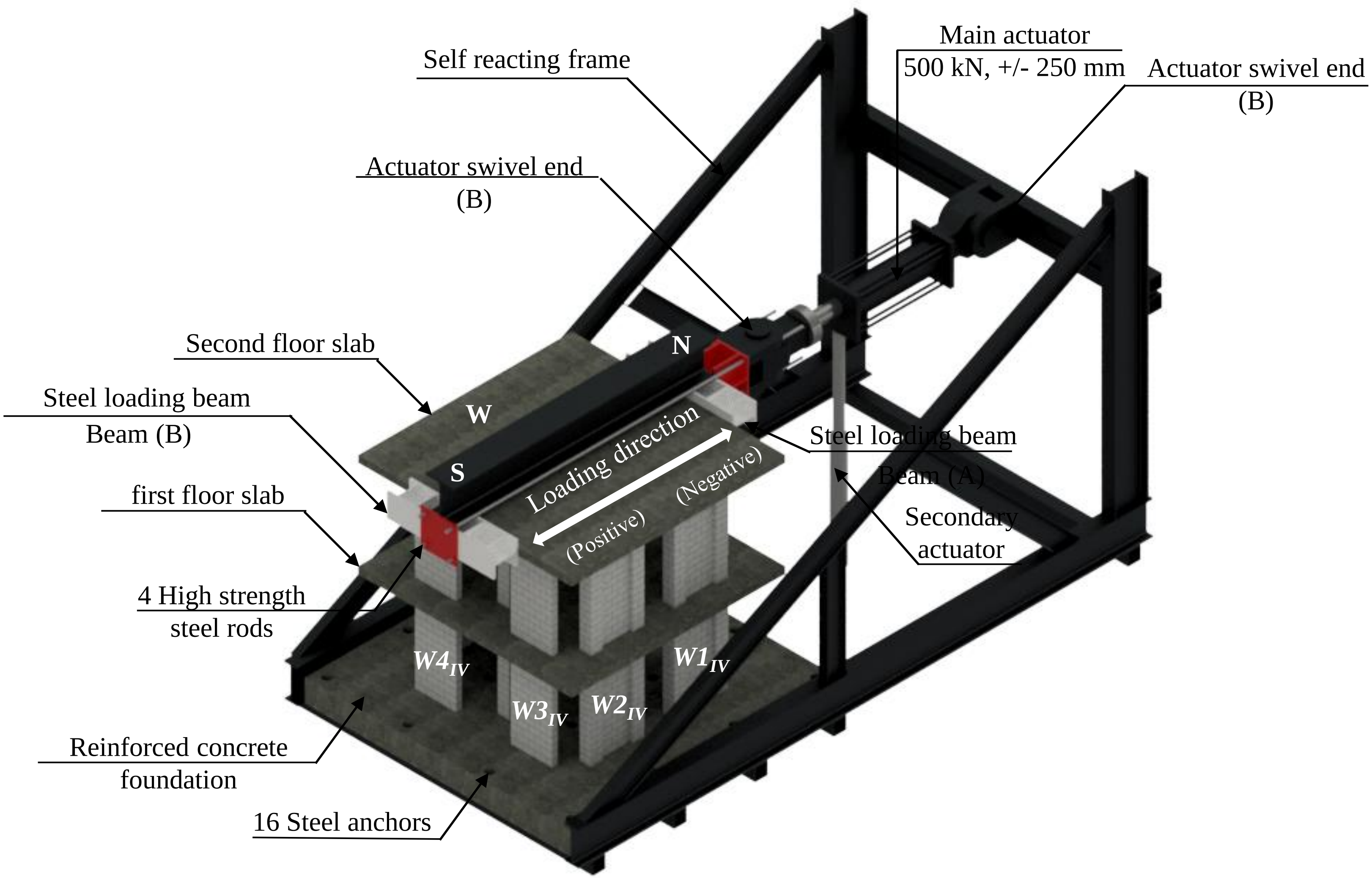

Fig. 3.3: Test Setup, building loading technique, and fixation to the structural laboratory floor.

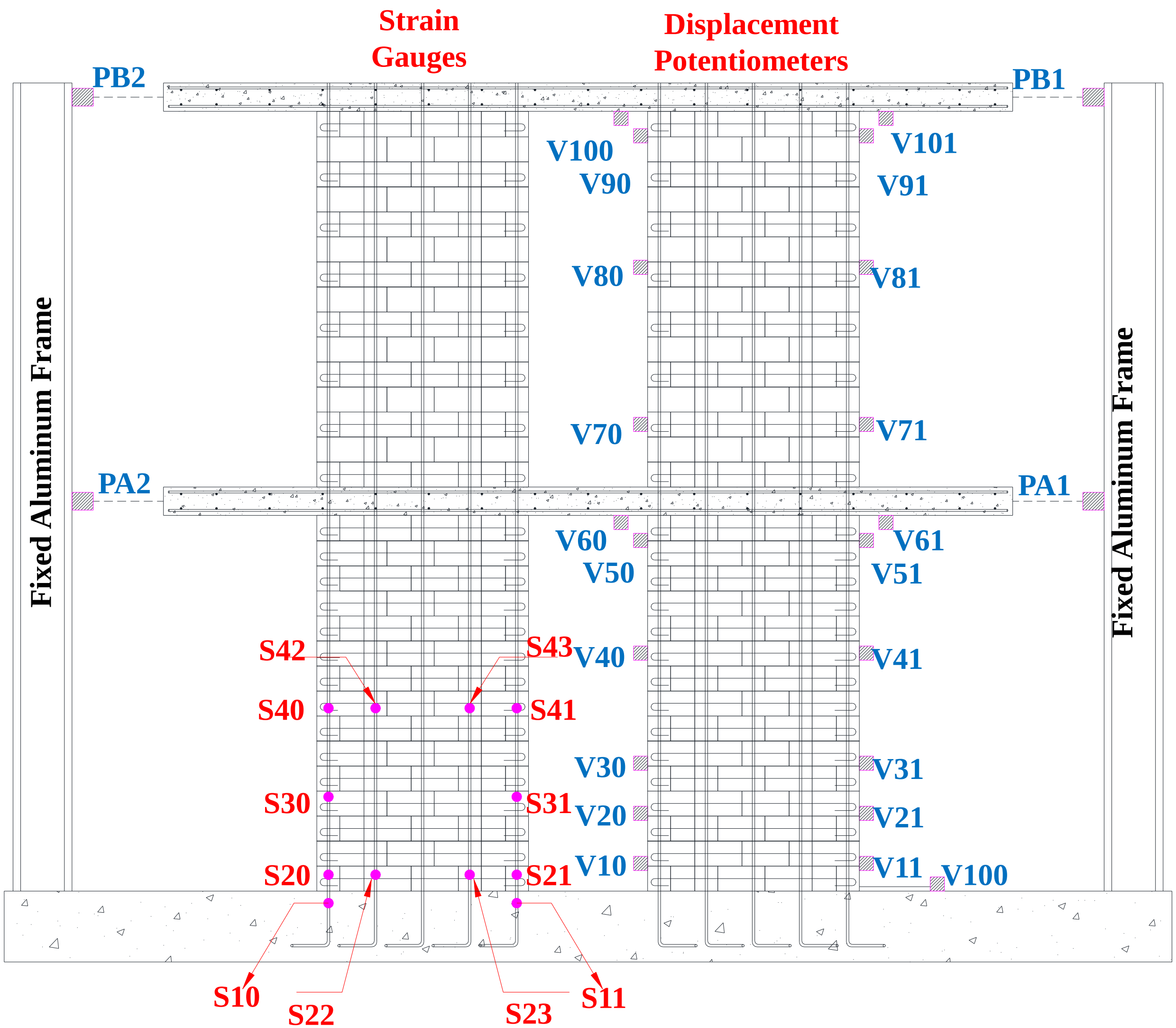

Fig. 3.4: Typical walls instrumentation.

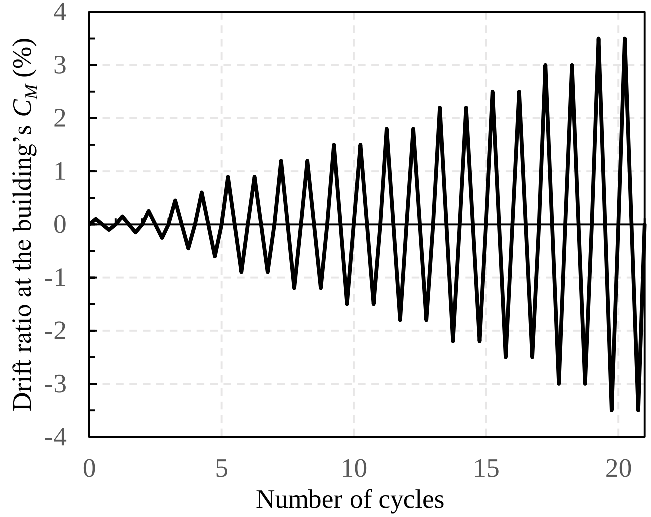

Fig. 3.5: Loading protocol.

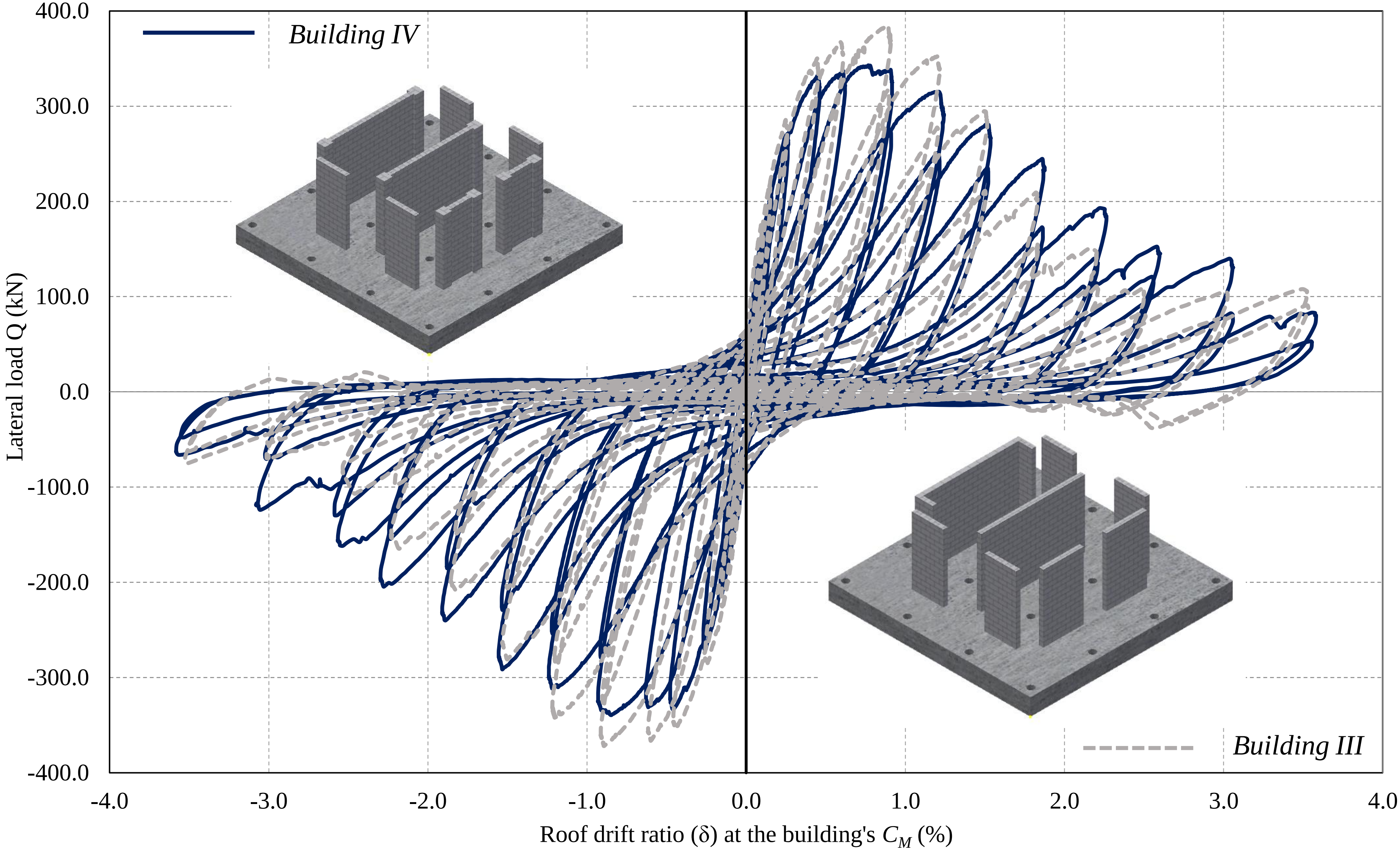

Fig. 3.6: Load-drift ratio hysteresis relationship of *Building III* and *Building IV*.

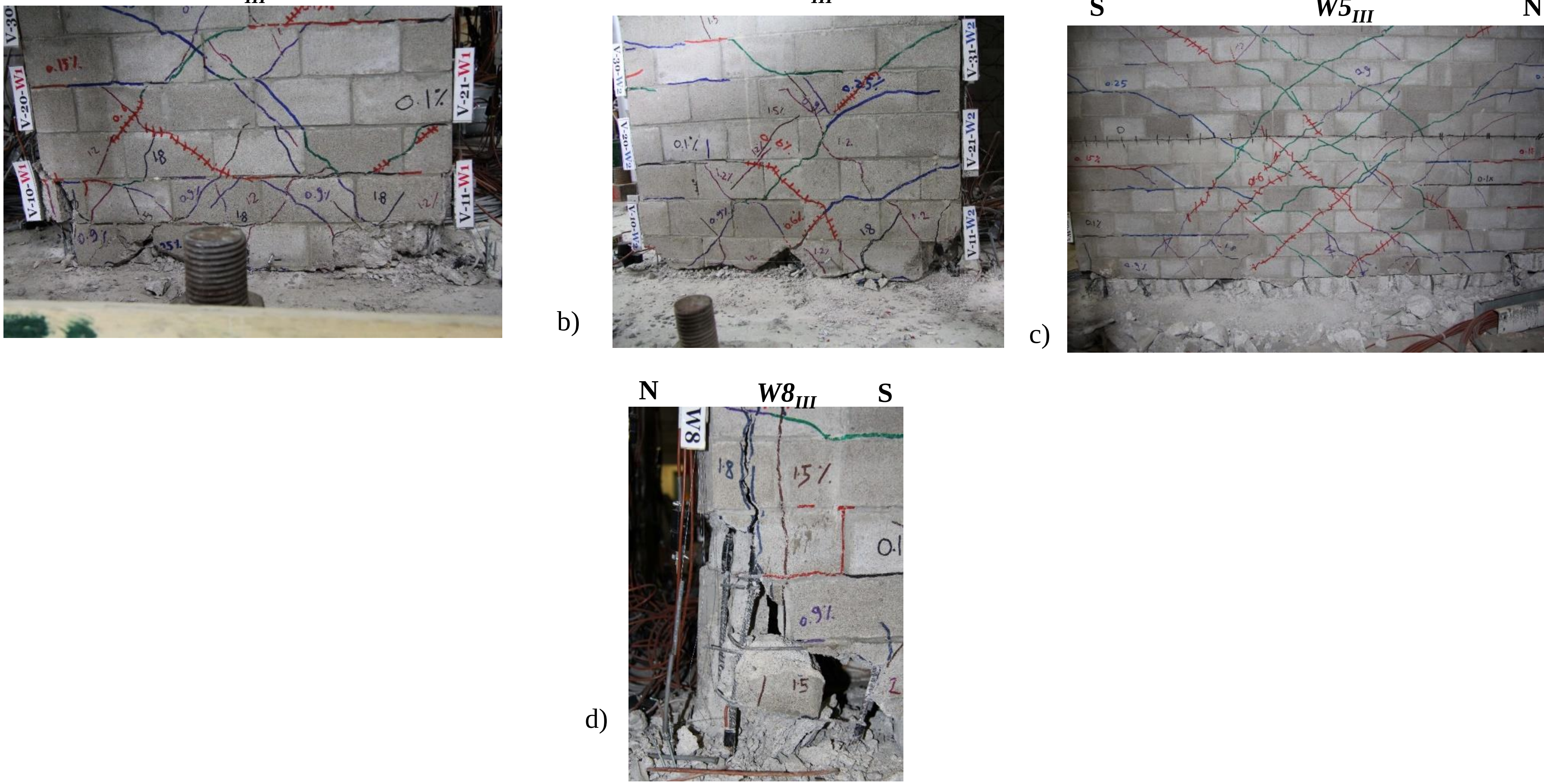

Fig. 3.7: Cracks at 2.2% drift ratio at building C_M of *Building III* and *Building IV*;

a)*W1$_{III}$* (Ashour et al.2016); b)*W2$_{III}$* (Ashour et al.2016); c)*W5$_{III}$* (Ashour et al.2016); d)*W8$_{III}$* (Ashour et al.2016).

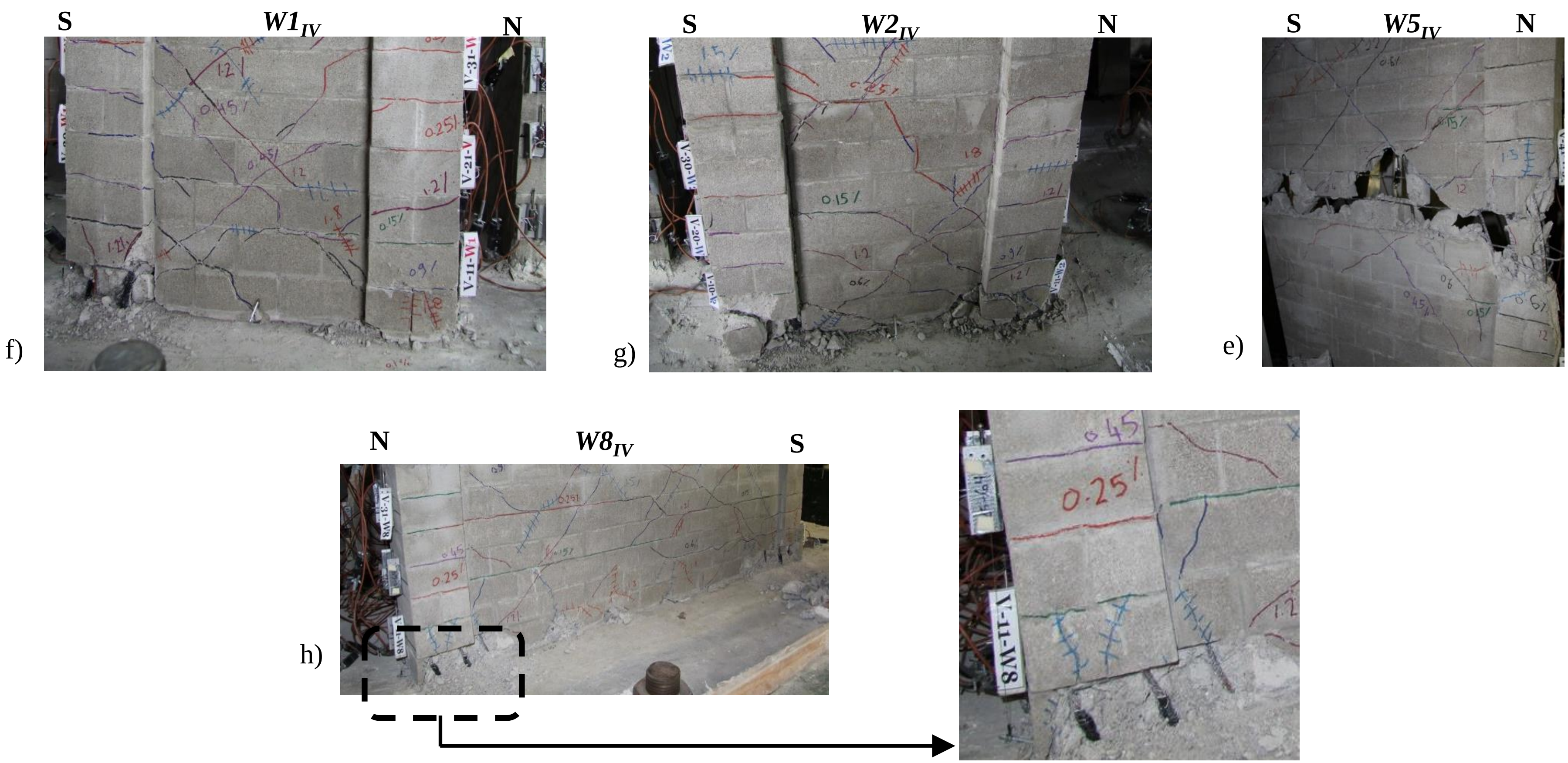

Fig. 3.7 (cont.): Cracks at 2.2% drift ratio at building C_M of *Building III* and *Building IV*;

e)$W5_{IV}$; f)$W1_{IV}$; g)$W2_{IV}$; h)$W8_{IV}$.

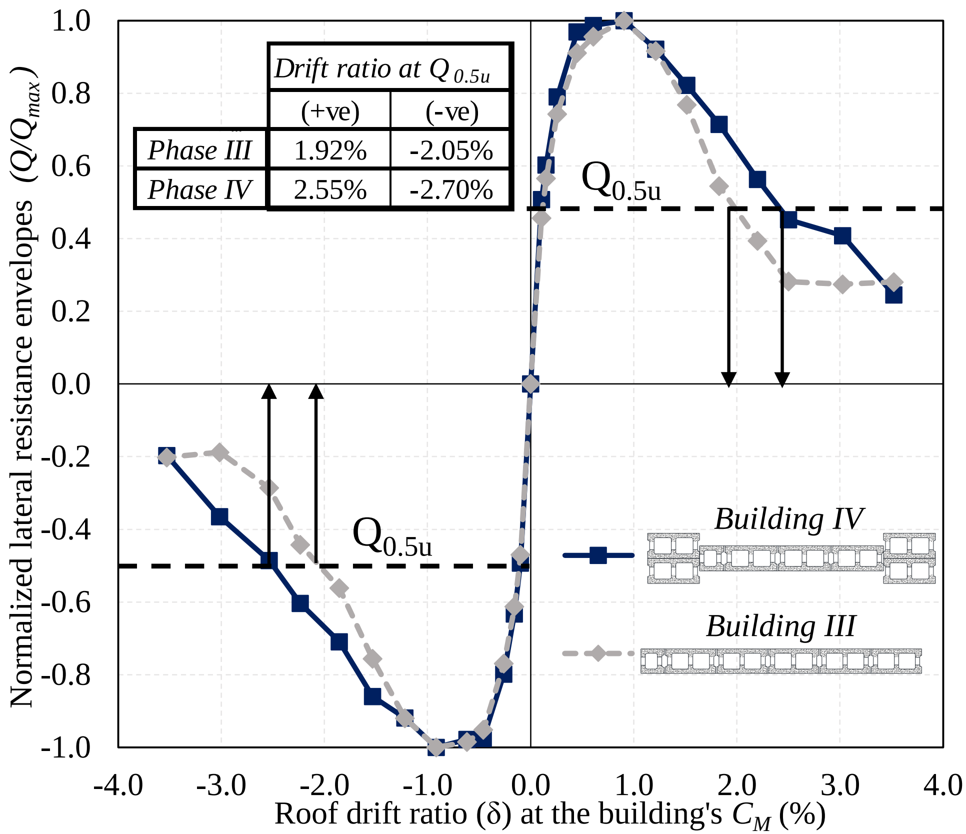

Fig. 3.8: Normalized lateral resistance envelopes versus roof drift ratio of *Building III* and *Building IV*.

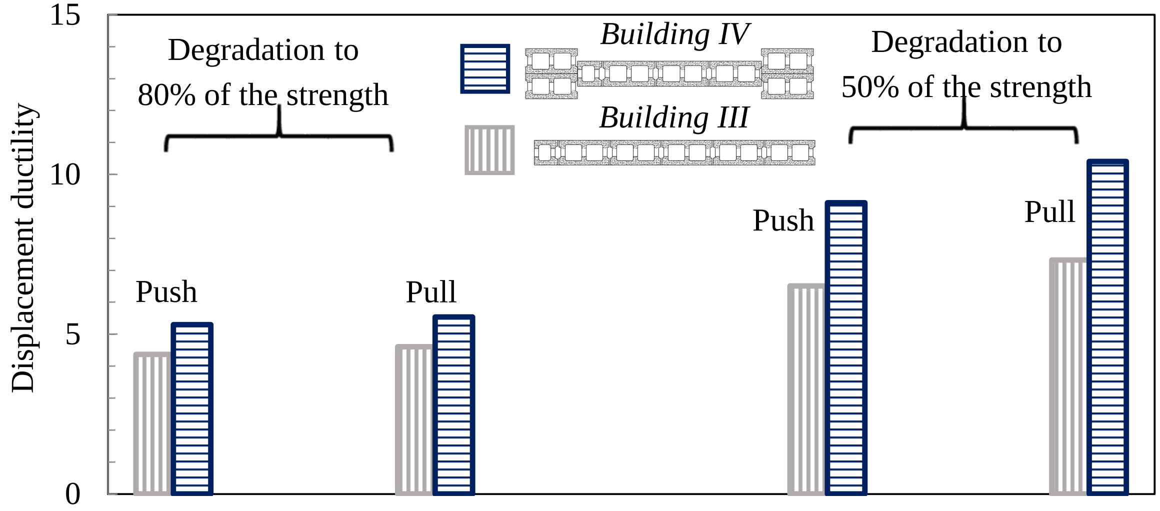

Fig. 3.9: Idealized displacement ductility capacities of *Building III* and *Building IV* following *Approach 1*.

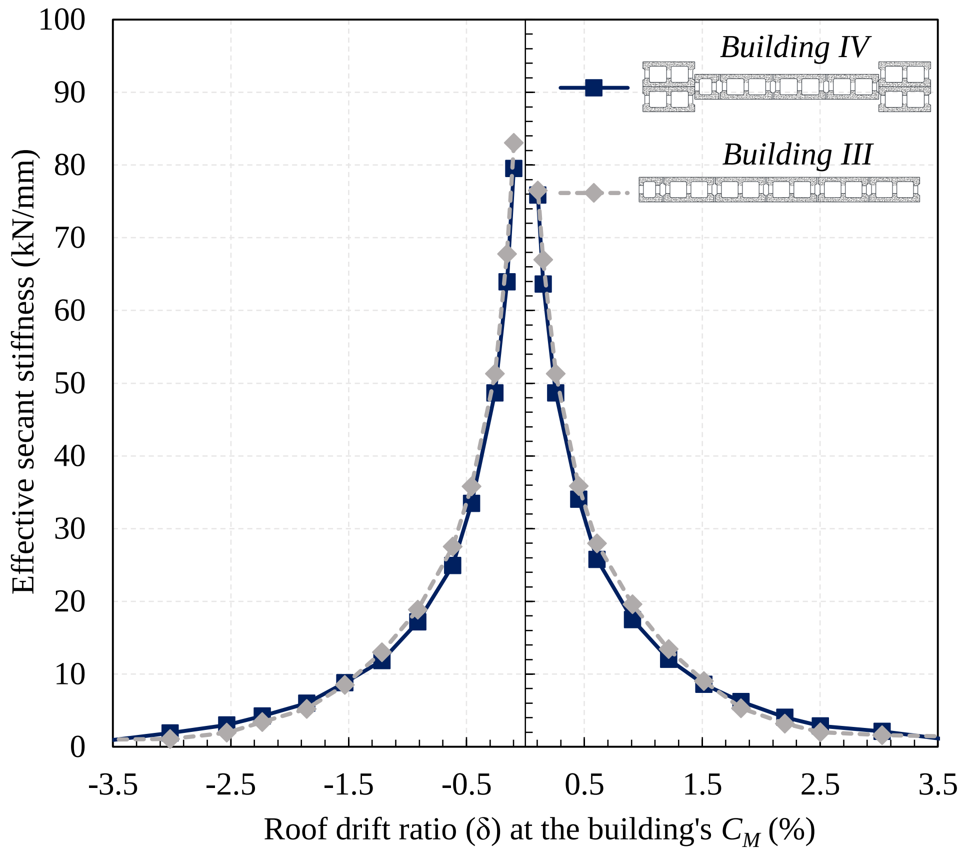

Fig. 3.10: Variation of effective secant stiffness versus roof drift ratio of *Building III* and *Building IV*.

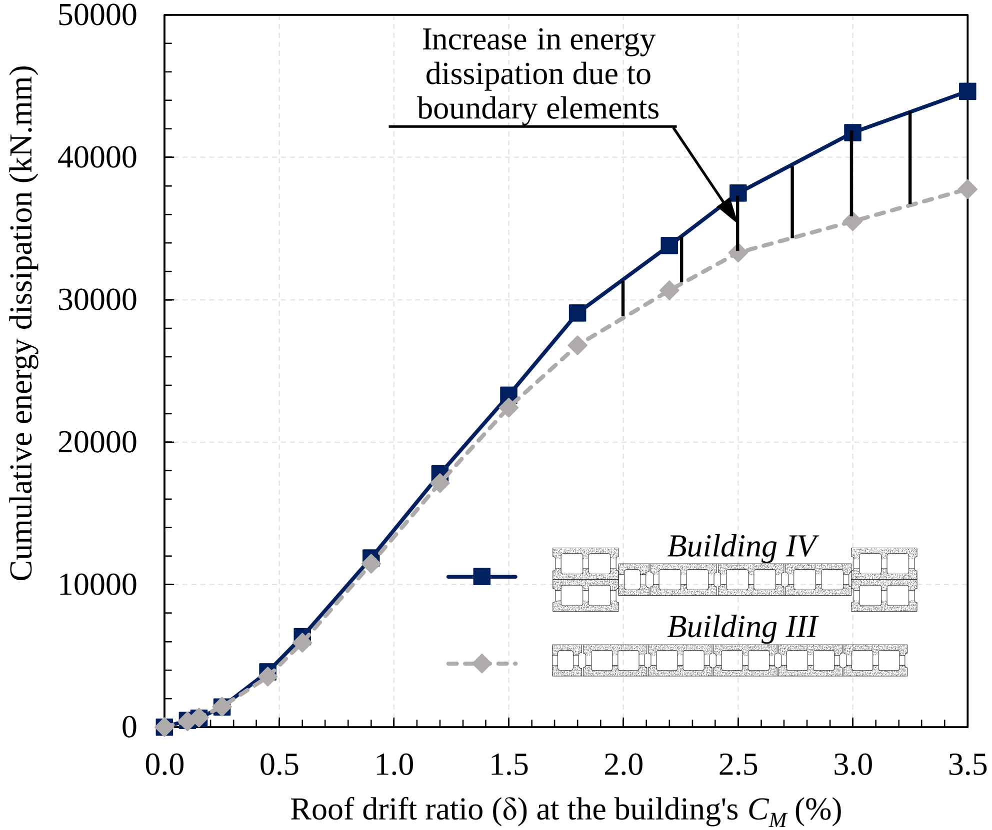

Fig. 3.11: Energy dissipation versus roof drift ratio of *Building III* and *Building IV*.

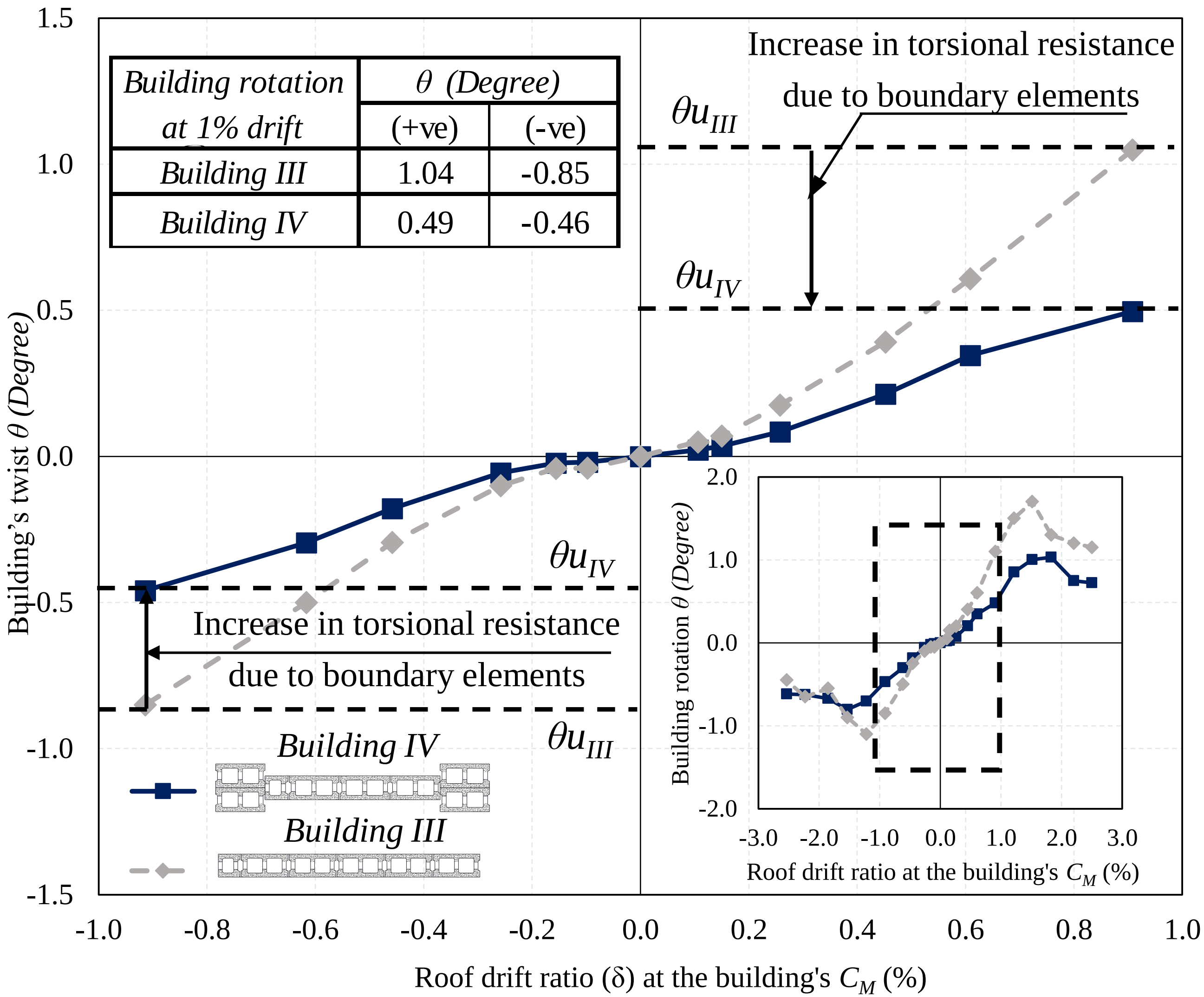

Fig. 3.12: Building's twist angle calculated at the roof level versus the roof drift ratio of *Building III* and *Building IV* .

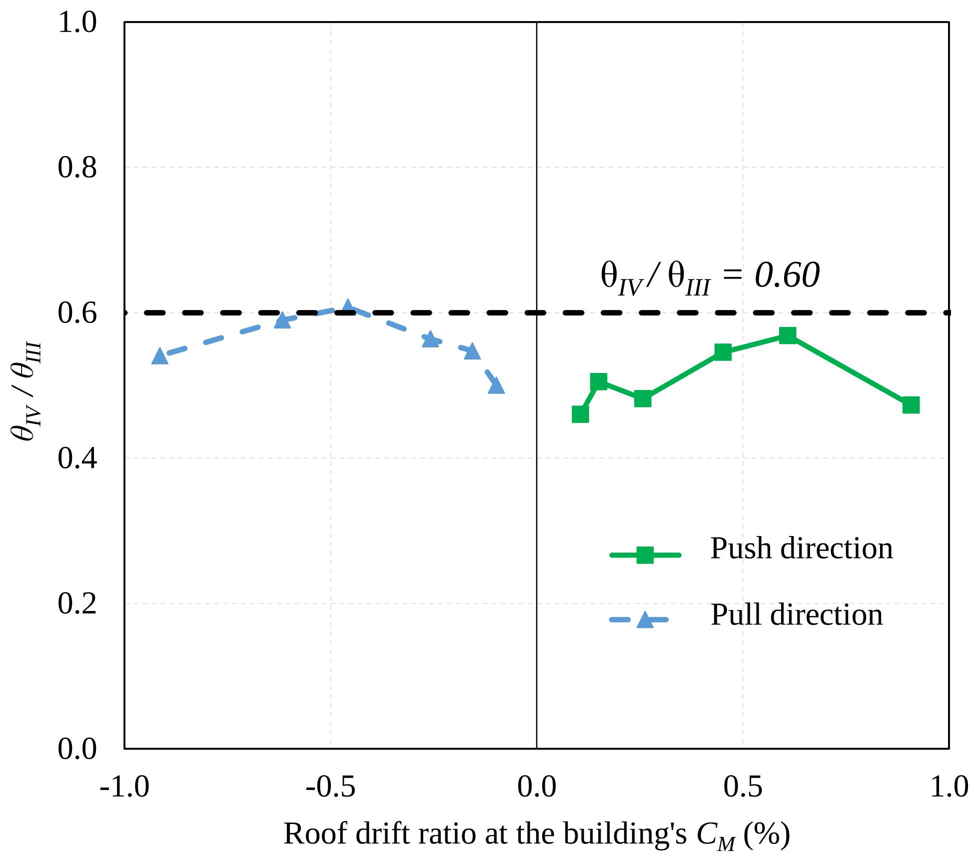

Fig. 3.13: Twist angle of *Building III* to that of *Building IV* calculated at the roof level versus the roof drift ratio.

CHAPTER 4
SYSTEM-LEVEL SEISMIC RISK ASSESSMENT METHODOLOGY: APPLICATION TO REINFORCED MASONRY BUILDINGS WITH BOUNDARY ELEMENTS

4.1 ABSTRACT

The development of system-level seismic fragility curves, which describe the probability of a building *systems* reaching different damage states under a given ground motion intensity level, is an essential step in pre- and post-earthquake risk assessment and resilience quantification. Nonetheless, current methodologies for generating fragility curves do not provide clear directions as to how to integrate the fragility of different building *components* within the overall building seismic risk assessment. However, several recent studies demonstrate that neglecting some of these components' contributions may lead to an erroneous seismic risk prediction of the overall building system. Recent research has also emphasized the need to develop alternative techniques to evaluate the system-level fragility to be adopted within the next generation of seismic assessment standards (e.g. ASCE 41). To address these issues, this chapter presents a new methodology that adopts two approaches, based on either component-level seismic losses or component strengths, in order to evaluate the overall system-level fragility. To demonstrate its practical application, the methodology is used to generate fragility curves for a reinforced masonry shear wall building with boundary elements. In this respect, OpenSees is utilized to develop a three-dimensional model of the building and subsequently conduct incremental dynamic analyses (IDA) using a suite of 44

ground motion records. Based on the IDA results, component-level damage states are identified and used to generate component- and, subsequently, system-level fragility curves. The analysis results show that the two proposed approaches yield consistent results, for the studied building configuration, that fall between a lower and an upper bound fragility estimate of the individual building components.

4.2 INTRODUCTION

Fragility curves are a useful tool for the seismic risk assessment and subsequently the seismic resilience quantification of buildings. A fragility curve gives the conditional probability that a building or component will reach or exceed a specific level of damage at a given ground motion intensity measure (e.g. spectral acceleration at the fundamental period). This damage is usually related to the building functionality level and repair cost. Fragility curves have been used as a tool for pre-earthquake planning and post-design verification (Nielson and Bowers 2007). Fragility curves can be also used in post-earthquake assessment to prioritize retrofit and estimate losses, thus reducing the duration of the assessment stage of recovery after an earthquake (Ranf et al. 2007). To attempt to quantify building resilience, fragility curves for different seismic force resisting systems (SFRS) should first be available to engineers and decision makers.

For many SFRS, including masonry structures, several approaches have been used to develop fragility curves. These approaches are divided into three main categories: empirical, expert and analytical methods. (1) *Empirical* methods are based on post-earthquake evaluations of actual damage. For instance, fragility curves for some of the more common building types (e.g. reinforced masonry, reinforced concrete and steel frames) were developed based on a survey of 70,000 buildings subjected to 13 different earthquakes (Spence et al. 1992). A following work used data from 50,000 damaged buildings in Italy (Sabetta et al. 1998) to develop empirical fragility curves for the Italian building typologies. Although *Empirical* methods have the advantage of being based on real observed data, they are strictly applicable only to structures and site conditions (e.g. soil properties and earthquake parameters) that are similar to the database used for calibration, and thus the use of these curves in different areas is sometimes not appropriate. (2) *Expert* methods are based on expert opinion and experience in providing the loss or the probability of damage of a given element or structure at risk under seismic loading. Such methods have been used to develop fragility curves, concentrating on the distinctive features of European cites with regard to current and historical masonry buildings (Lagomarsino and Giovinazzi 2006). Although these methods have the advantage of being less affected by the lack of extensive damage data compared to the *Empirical* method, they rely heavily on the experts' seismic performance experience with the buildings under consideration (Rossetto et al. 2013). (3) *Analytical* methods are based on the estimation of the damage distributions through the simulation of the building response subjected to different levels of seismic demand. The seismic demand can be represented by nonlinear static analysis (Oropeza et al. 2010; Pagnini et al. 2011; Lagomarsino and Cattari

2013) or by nonlinear time history analysis (Erberik 2008; Gehl et al. 2013). *Analytical* methods result in a reduced bias and increased reliability of the vulnerability estimates for different structures compared to the *Empirical* and *Expert* methods, and thus they present a more efficient approach to generate the required data (Pitilakis et al. 2014). *Analytical* methods have become widely adopted because they are more readily applied to different structural systems and geographical areas where damage records are insufficient.

All fragility studies published to date that have focused on reinforced masonry (RM) buildings have considered only walls with rectangular cross sections, whereas RM buildings with boundary elements are a newly proposed structural system within the North American codes (MSJC 2013; CSA 2014). The use of boundary elements in RM walls allows closed ties to be used and multiple layers of vertical bars to be accommodated, thus providing a confining reinforcement cage. This enhances the overall performance of the RM buildings with boundary elements relative to traditional RM buildings (Shedid et al. 2010; Banting and El-Dakhakhni 2012; Ezzeldin et al. 2016a). As such, the analyses in this chapter are performed on RM buildings with boundary elements to facilitate the development of prescriptive design requirements, as recommended by the Masonry Standard Joint Committee (MSJC 2013).

Similar to other SFRS, most of the fragility studies on RM to date have considered only the fragility of individual components (Murcia-Delso and Shing 2012; Banting and El-Dakhakhni 2014; Siyam et al. 2015) rather than combining their contributions to the overall building response. Considering only individual components may cause the entire building to be deemed a collapse hazard (by analysis) even though all the other components throughout the building are within their acceptance criteria. This simplified assumption may be appropriate for *Series* type systems (e.g. water networks and nuclear facilities), where a failure of one of the components constitutes a failure of the system. However, real building systems usually have redundancy, defined as the capacity of structural systems to continue to carry loads following the failure of one or more of their components, as long as this failure does not result in a loss of the gravity-load carrying capacity or overall stability (Melchers 1999). Subsequently, many studies have shown that neglecting the contribution of any significant component may lead to a misrepresentation of the overall systems' fragility (Choi et al. 2004; Nielson and DesRoches 2007). As such, an improved methodology is needed to develop system-level fragility curves based on the individual RM component fragilities in order to improve the reliability and effectiveness of seismic risk assessment tools and maximize the future of the system-resilience evaluation.

The current chapter presents a new system-level fragility quantification methodology that can be extended not only to other RM building systems but to any SFRS. In this respect, a simplified three-dimensional numerical model of RM shear wall buildings is developed and validated using data from experimental test programs. Following the model validation, fragility curves are developed at different damage states for the components of an archetype building by performing nonlinear time history analyses on the building using a suite of 44 ground motion records. Finally, these individual component fragilities are combined using two different proposed approaches to generate the overall system-level fragility curves.

4.3 SUMMARY OF THE EXPERIMENTAL PROGRAMS

In this chapter, the numerical models of RM shear wall buildings are validated against the experimental results of Heerema et al. (2015) and Ezzeldin et al. (2016b). These previous experimental programs were selected because they include walls with different levels of slab coupling and different wall configurations with a range of aspect ratios, from 1.5 to 4.6. More details regarding the experimental programs are given in this section.

4.3.1 Building Layouts

Heerema et al. (2015) tested a one-third scaled two-story asymmetrical RM shear wall building (referred to as *Building II*) under displacement-controlled quasi-static cyclic fully-reversed loading. *Building II* was composed of four shear walls with rectangular cross sections aligned along the loading direction, and four other walls with rectangular cross sections aligned orthogonally, as shown in Fig. 4.1(a). However, the level of coupling between walls during the test was minimized by detailing the two floor slabs with hinge lines, where the slab thickness was reduced at specific locations, as shown in Fig. 4.1(b). The overall height of the building was 2,160 mm, comprising two floors, each 1,000 mm in height, corresponding to 3,000 mm in full-scale, with slotted 80 mm thick reinforced concrete (RC) floors, each 2,400 mm × 2,400 mm in plan. The building was fixed to the laboratory strong structural floor by 16 prestressed anchors through a square RC foundation (3,000 mm × 3,000 mm) with a thickness of 250 mm.

Ezzeldin et al. (2016b) tested a building with the same nominal strength (referred to as *Building IV*), but without hinge lines, in order to investigate the effects of wall coupling on the building and wall response. In addition, the RM shear walls with rectangular cross sections located along the loading direction in *Building II* were replaced with confined RM shear walls with boundary elements in *Building IV*, as shown in Fig. 4.2(a). The boundary elements were adopted in *Building IV* because they allow closed ties to be used and multiple layers of vertical bars to be accommodated, thus providing a confining reinforcement cage, as shown in Fig. 4.2(b). Full details of the experimental programs and test results can be found in Heerema et al. (2015) and Ezzeldin et al. (2016b) for *Buildings II* and *IV*, respectively.

4.3.2 Materials and Test Protocol

A one-third scale version of the standard two-cell 190-mm hollow concrete masonry unit (190×190×390 mm) commonly used in North America was used for the walls in both buildings. The reduced-scale concrete blocks were 130 mm in length, 63 mm in width and 63 mm in height. Table 4.1 summarizes the average compressive strength of the 2-block high prisms, f'_m, and the average yield strengths of the vertical and the horizontal bars, f_{yv} and f_{yh}, respectively, within *Buildings II* and *IV*.

The cyclic loading scheme for both buildings consisted of a series of displacement-controlled loading cycles to assess the strength and the stiffness degradation. The lateral cyclic displacement was applied using a hydraulic actuator with a capacity of 500 kN and a maximum stroke of 250 mm in each direction. To obtain the post-peak behavior, the displacements were increased beyond the point where the building had reached its maximum lateral load resistance, until the building resistance reduced to approximately 80% of its maximum capacity.

4.4 NUMERICAL MODEL

4.4.1 Selection of Elements

A three-dimensional (3D) model was developed using OpenSees (McKenna et al. 2013) to simulate the inelastic behavior of *Buildings II* and *IV* under cyclic loading. Displacement-based beam-column elements were adopted to model the walls of both buildings. These elements follow standard finite element formulation, in which the element displacement field is derived from nodal displacements. The formulation of this element assumes a linear curvature distribution and a constant axial strain. The beam-column elements were assigned fiber sections that discretely modelled the reinforcement and masonry regions. The choice of element length is a very important aspect when displacement-based beam-column elements are used with distributed plasticity and strain-softening material laws. This is attributed to strain localization, in which the plastic deformation tends to concentrate in the first element above the base of the wall, while the adjacent elements remain elastic (Calabrese 2008). Because of strain localization, the numerical results are very sensitive to the length of the first element above the base, which should be equal to the plastic hinge length. The formula proposed by Bohl and Adebar (2011) was found to give a good estimate of the plastic hinge length for RM shear walls with and without boundary elements (Ezzeldin et al. 2016a). Full details of the modelling technique used for the RM walls within the 3D model for both buildings, including the distribution of nodes and elements, can be found in Ezzeldin et al. (2016a).

The two RC floor slabs of *Building II* were detailed with hinge lines to minimize the coupling between the RM walls, so they were modelled considering the diaphragm to have no out-of-plane stiffness, while being rigid in plane. In *Building IV*, the slabs were not detailed with hinge lines, so they were simulated using multi-layer shell elements (ShellMITC4 in OpenSees). The multi-layer shell element is made up of a number of layers with specified thicknesses and material properties and is based on the principles of composite material mechanics. During analysis, the strains and curvatures of the middle layer of the shell element are obtained first, and the strains in other layers are then determined based on the plane-section assumption. Subsequently, the stresses are calculated according to the constitutive model of the corresponding layer, and the internal forces are finally determined using the standard numerical integration method (Lu et al. 2015). The slab reinforcement was modelled using 4 layers to represent the upper and lower rebars in the two directions.

4.4.2 Material Models

Chang and Mander's model for concrete in OpenSees (Concrete07) was used to model the masonry based on the measured compressive strength, f'_m, the strain at the maximum compressive strength, ε_m, the elastic modulus, E_m, and other parameters that define strength and stiffness degradation. The strength and stiffness degradation parameters were taken according to the formulae reported in Chang and Mander (1994). Unlike the RM shear walls with rectangular cross sections in *Building II*, the RM walls with boundary elements in *Building IV* have stirrups to confine the masonry and the vertical reinforcement near the extreme compression fiber. This confinement significantly enhances both the strength and the strain capacity of the compressed masonry zone (boundary element region). This aspect was taken into consideration by assigning different material properties for the masonry inside the closed ties at the boundary element area. The model by Mander et al. (1988) was used to calculate the compressive strength, f'_{mc}, and the strain at maximum compressive strength, ε_{mc}, within the boundary element confined area. The reinforcement steel was modelled using a Giuffre-Menegotto-

Pinto model (Steel02). This model is defined by the yield strength, initial elastic modulus, post-yield tangent modulus and other constants that control the transition from elastic to plastic zone. All of these properties and parameters were defined based on material characterization tests as shown in Table 4.1, without any need for calibration to the overall wall response. This approach has been validated against experimental results for individual walls previously by Ezzeldin et al. (2016a).

4.5 MODEL VALIDATION

Figure 4.3(a) compares the behavior of the numerical model with the experimental results for *Building II* tested by Heerema et al. (2015). To also verify the effectiveness of the developed 3D numerical model for buildings with both boundary elements and slab coupling, the numerical model results are compared with the experimental results from *Building IV* (Ezzeldin et al. 2016b) in Fig. 4.3(b). In addition, Table 4.2 summarizes the maximum error of the model predictions relative to the experimental data of both buildings in terms of the lateral load and the energy dissipation. As can be seen in Fig. 4.3 and Table 4.2, the model is capable of simulating most relevant characteristics of the cyclic response at different drift levels up to degradation of 20% of the ultimate strength. As shown in Table 4.2, the model predicts the peak lateral load of *Buildings II* and *IV* during each cycle to within a maximum error of 13% and 14%, respectively. In addition, the energy dissipation is captured closely for both buildings: Fig. 4.3 and Table 4.2 show a maximum error of less than 12% and 14% relative to the experimental results of *Buildings II* and *IV*, respectively, even though there is some difference in the level of hysteretic pinching at large displacements in *Building IV*. Overall, the differences between the experimental and numerical results are considered to be acceptable in terms of RM shear wall response predictions.

The results show that the slab modelling technique used in each building has a significant influence on the cyclic response throughout the test, influencing the building stiffness, lateral resistance capacity, and stiffness degradation. For instance, the lateral strength of *Building IV* is on average 45% higher than that of *Building II*, as shown in Fig. 4.3, despite the individual walls have been designed to have the same strength to within 5%. Overall, the comparison between the experimental and numerical results shows that the modelling technique used in this chapter is able to capture the response of RM shear wall buildings both with and without significant slab coupling.

4.6 PERFORMANCE AND DAMAGE LEVELS

Many experimental studies have been conducted to evaluate the failure modes and level of damage that can develop in RM shear walls subjected to in-plane seismic loading (Priestley 1976; Shing et al. 1991; Voon and Ingham 2006; Shedid et al. 2010; Banting and El-Dakhakhni 2012). In these studies, different damage states have been identified by the level of repair, expected downtime and corresponding cost. Three damage states were adopted within the current analysis scope following the criteria identified by the Applied Technology Council (ATC 2009). Although the ATC, 2009 document is focused on RM walls with rectangular cross sections, the boundary element construction practice is considered to be sufficiently similar to allow adoption of the same damage state criteria. In this respect, a *Slight* damage (DS1) is characterized by a few flexural and shear cracks, with small residual cracks and yielding of the extreme vertical reinforcement. However, neither spalling of masonry nor fracture of reinforcement should occur at this damage state. DS1 requires only cosmetic repair by patching the cracks and painting each side of the wall. DS1 is realized as the point when the wall approaches 80% of its peak resistance. *Moderate* damage (DS2) is characterized by many flexural and shear cracks, associated with some residual cracks. Vertical cracks or slight spalling may occur in the toe regions of the wall, but no fracture or buckling of reinforcement should exist in this damage state. A wall at DS2 can be repaired either by injecting the cracks using epoxy or by removing the loose masonry and using non-shrink grout if spalling has occurred. DS2 corresponds to the wall reaching its ultimate resistance. *Severe* damage (DS3) is characterized by extensive flexural and shear cracks, significant residual cracks, masonry spalling and fracture of the bars. At this damage state, repair or partial replacement of the wall may not be convenient, so the structure would be shored to replace the damaged component with a new one. A wall suffers DS3 either when it is loaded beyond its peak ultimate resistance and reaches a reduction of 20% of its peak resistance (flexural damage) or when the shear force reaches the wall nominal shear strength (shear damage) (ATC 2009) calculated based on the MSJC (2013) code formula (NIST 2010).

4.7 APPLICATION EXAMPLE

4.7.1 Archetype Building

An example is adopted in this chapter to assess the probability of exceedance for these three damage states based on the four-story building that the National Institute of Standards and Technology (NIST 2010) used to investigate the FEMA P695 (FEMA 2009) methodology. For this chapter, the walls in that building were redesigned with boundary elements using the same seismic performance factors, such as the response modification factor (R), the deflection amplification factor (C_d) and the system overstrength factor (Ω_0). In addition, all of the original walls (S3 in the North-South direction and S13 in the East-West direction) in NIST (2010) had the same length in each direction, whereas the walls in this chapter were redesigned using two different lengths in each direction, in order to investigate the contribution of each wall to the system fragility in that direction. As shown in Fig. 4.4, the SFRS consisted of eight RM shear walls with boundary elements in each direction, without any contribution from the shown gravity columns. All the walls were fully grouted with a total height of 12.20 m and lengths of 9.75 m (S3-L and S13-L) and 6.10 m (S3-S and S13-S). The boundary elements at the wall ends were formed using two standard concrete masonry units, making them 406.4 mm (16 inch) square. The floor and roof systems consisted of precast hollow core slab with a cast-in-place concrete topping slab.

4.7.2 Design Requirements

All of the walls were designed according to the seismic provisions of ASCE/SEI 7-10 (ASCE 2010) and the strength design requirements of the Masonry Standards Joint Committee (MSJC) code (MSJC 2013) for Seismic Design Category (SDC) D_{max} as defined in FEMA P695 (FEMA 2009). Following the previous study (NIST 2010), the unconfined masonry compressive strength, f'_m, was taken as 13.8 MPa in Walls S13-L and S13-S and 20.7 MPa in Walls S3-L and S3-S, while Grade 60 steel (414 MPa nominal yield strength) was chosen for the reinforcement in all the walls. Table 4.3 summarizes the RM wall dimensions, aspect ratios and reinforcement details at the first floor for all walls.

4.7.3 Archetype Modelling

A 3D numerical model was developed to simulate the seismic response of the archetype building using the modelling technique discussed above. Although torsional response was not considered in this chapter, the 3D model was chosen to account for the distribution of the walls in plan. Gravity columns were not included in the 3D model because they were assumed to carry gravity loads only without contributing to the SFRS. Since the floor and roof systems consisted of precast hollow-core slabs, they were modelled similar to *Building II* by considering the diaphragm to have no out-of-plane stiffness, while being rigid in plane. Gravity loads and seismic masses were assigned to the walls based on tributary area. Complete fixity was assumed at the base of each wall without consideration of soil-structure interaction effects.

4.8 NONLINEAR DYNAMIC RESPONSE ANALYSES

The seismic response of this building archetype was evaluated by performing full nonlinear time-history analyses following the concept of Incremental Dynamic Analyses (IDA) (Vamvatsikos and Cornell 2002).

4.8.1 Ground Motion Selection and Scaling

The archetype building was analyzed using the set of 44 far-field ground motion records (22 pairs of horizontal components) that was developed as part of the FEMA P695 methodology (FEMA 2009). Following that methodology, the ground motion records were normalized by their respective peak ground velocities to remove unwarranted variability. The records were then scaled so that the median spectrum value matches the Maximum Considered Earthquake (MCE) response spectrum acceleration for SDC D_{max} at the code fundamental period (T = 0.45s), as shown in Fig. 4.5. The code fundamental period, T, was calculated in this study as the product of the coefficient for the upper limit on the calculated period (C_u =1.40), and the approximate fundamental period (T_a =0.32s), as recommended by ASCE/SEI 7-10 (ASCE 2010).

4.8.2 Dynamic Analyses

The archetype building model was subjected to the 44 ground motions in the North-South direction and the East-West direction separately to evaluate the seismic response of Walls S3-L and S3-S and Walls S13-L and S13-S, respectively. The record set did not include the vertical component of ground motions because the vertical direction of earthquake was not considered of primary importance for damage evaluation (FEMA 2009). Each ground motion was scaled to increasing intensities until all walls in the direction of interest reached the *Severe* damage state (i.e. degradation to 80% of the peak strength). Spectral acceleration (S_T), at the code fundamental period, T , was selected as the intensity measure because the vibration of the low-rise and mid-rise structures is dominated by the first mode (Vamvatsikos and Cornell 2002). Based on NIST (2010), initial stiffness-proportional Rayleigh damping of 5% was assigned at the periods of the first and third modes. During the analyses, key component responses (e.g. curvature, base shear, roof drift) were monitored and recorded, and were used afterwards to identify the damage state of the walls.

Figure 4.6 shows the IDA results for the four walls. Each point in each IDA curve represents a single nonlinear dynamic analysis of one wall when the building model was subjected to one ground motion record scaled to one intensity level in one direction (North-South or East-West). The differences in the response of each wall, when subjected to different ground motions with different frequency characteristics, are shown in Fig. 4.6 from the scatter of the wall curvatures at each intensity level. For each wall, the median spectral intensity at each damage state ($S_{Slight}, S_{Moderate}, S_{Severe}$) is given in Fig. 4.6.

4.9 COMPONENT FRAGILITY CURVES

Using the data from the IDA results, fragility curves can be defined through a cumulative distribution function (CDF) that relates the ground motion intensity to the probability of damage. Figure 4.7 shows the fragility curves for the four walls within the building archetype for the *Slight*, *Moderate* and *Severe* damage states. The maximum likelihood method was used to estimate the median spectral intensity and the dispersion at each damage state, which are required to fit the fragility data based on the IDA results for each wall (Baker 2015) into corresponding curves. For all of the damage states shown in Fig. 4.7, the longer walls (S3-L and S13-L) were more fragile than the shorter walls (S3-S and S13-S). For instance in the North-South direction, Wall S3-L had median spectral intensities of 0.62g, 2.34g and 3.29g at the *Slight*, *Moderate* and *Severe* damage states, respectively, while Wall S3-S reached the same damage states at 0.92g, 2.82g and 3.92g. This difference is mainly attributed to the variation in the yield displacement capacity, which is approximately inversely proportional to the wall length. Therefore, longer walls start yielding first, thus increasing their risk of damage under seismic loads in a system where all walls are subjected to the same displacement demands.

4.10 SYSTEM-LEVEL FRAGILITY BOUNDS

To evaluate the seismic resilience at the system level, it is necessary to first combine the individual component-level fragilities into an overall system-level fragility. This can be performed through direct integration over all the possible domains that describe the designated limit states. This integration approach will result in the probability of exceedance for that particular system at a given value of the intensity measure. However, depending on the details of the system and the number of possible failure modes, providing this integration in a closed form can be very complex. An alternative approach would be to combine the component fragility curves using bounding techniques to generate the system fragility curve. However, this requires information about the interdependency of failure modes between the different system components. Traditionally, systems have been idealized as belonging to two main types: *Series* systems and *Parallel* systems, as described below.

4.10.1 Series Systems

In *Series* systems (also called "weakest link" systems in Melchers (1999)) any one component that reaches a given damage state constitutes the whole system reaching the same damage state (Melchers 1999). Using first-order reliability theory, the lower bound on the system fragility is the maximum component fragility while the upper bound is a combination of the component fragilities (Cornell 1967). These bounds are given in Eq. (4.1):

$$\max_{i=1}^{m}[P(F_i)] \leq P(F) \leq 1 - \prod_{i=1}^{m}[1 - P(F_i)] \tag{4.1}$$

The bounds are in terms of the number of the components, m, the probability of damage of component i, $P(F_i)$, and the probability of damage of the system, $P(F)$. The lower bound represents the probability of damage for a system whose components are all fully dependent, while the upper bound assumes that the components are all independent. Although the lower and the upper bounds provide, respectively, un-conservative and conservative estimates of the system-level fragilities for *Series* systems, these bounds are sometimes not considered appropriate for structural applications (Grimmelt and Schuller 1983) because building systems typically include redundant components. This redundancy is defined as the capacity of structural systems to continue to carry loads following the failure of one or more of their components, which contradicts the definition of *Series* systems.

4.10.2 Parallel Systems

In *Parallel* systems, the components are connected in such a way that the reaching of a damage state in any one or more components does not necessarily mean that the whole system reaches the same damage state (Melchers 1999). Based on the uni-component probability, Boole (1854) derived the upper and lower bound fragility for *Parallel* systems as given in Eq. (4.2):

$$\max\left(0, \sum_{i=1}^{m} P(F)_i - (m-1)\right) \leq P(F) \leq \min_{i=1}^{m}[P(F_i)] \tag{4.2}$$

The upper bound assumes that the *Parallel* system can only reach a damage state when all its contributory components have reached the same damage state. Unfortunately, although buildings have some redundancy, a certain level of damage to a subset of components may still be sufficient to be considered a similar level of damage to the building as whole, especially if those components contribute significantly to the building's strength or stiffness prior to the damage. In other words, the building could lose its structural integrity in any stage between the failure of one component and when all the comprising components of the system reach their collapse limit state.

4.11 SYSTEM-LEVEL FRAGILITY BASED ON COMPONENT CONTRIBUTIONS

A typical building does not exactly follow the definitions of *Series* or *Parallel* given above, but no formulae are currently available for computing bounds on the fragility of such a system. Moreover, current procedures consider global demand parameters (e.g. inter-story drift) in their assessments of the system-level fragility. However, these parameters may not be appropriate for all components, in that some components may be able to sustain a higher level of demand before reaching a particular damage state when compared to other components, even when all components are made of the same material. As such, the National

Institute of Standards and Technology (NIST 2005) recommended that there is need for a methodology to estimate the system-level fragility that depends on the actual fragility of all components. In the following two sections, two approaches to combine the fragility of all contributing system components are proposed, based on using either the seismic loss or the strength of the individual components.

4.11.1 Component Seismic Losses Approach

The structural losses, L_S, for any building system can be evaluated in accordance with the methodology provided in HAZUS (FEMA 2003) using Eq. (4.3):

$$L_S = BRC \times \sum_{i=1}^{N} \left[P(F)_i \times RCS_i \right] \tag{4.3}$$

Where BRC is the building's SFRS replacement cost; $P(F)_i$ is the probability of the SFRS being at damage state *i* (but not in damage state *i+1*), and RCS_i is the ratio of the structural repair cost of the SFRS at damage state *i* to the *BRC*. It should be noted that although similar calculations are adopted in HAZUS (FEMA 2003) to evaluate the nonstructural losses, only the structural losses of the SFRS are evaluated within the scope of this chapter. For example, L_S can be calculated for the North-South direction of the building archetype at damage state *i* through the expansion of Eq. (4.3) as follows:

$$L_S = BRC \times \left(\frac{CRC_{S3-L}}{BRC} \times \sum_{i=1}^{N} \left(P(F_{S3-L})_i \times RCS_i \right) + \frac{CRC_{S3-S}}{BRC} \sum_{i=1}^{N} \left(P(F_{S3-S})_i \times RCS_i \right) \right)$$

(4.4)

Where CRC_{S3-L} and CRC_{S3-S} are the total component replacement costs of all Walls S3-L and S3-S, respectively, while $P(F_{S3-L})_i$ and $P(F_{S3-S})_i$ are the probabilities of damage of Wall S3-L and Wall S3-S at given S_T, respectively, determined from Fig. 4.7.

Structural replacement costs are based on the repair measures for each damage state, and include all the steps a contractor would implement to conduct a repair (FEMA 2012). Steps include, for example, demolition of wall finishes, grouting of walls, injection of epoxy and painting of walls sides. Repair costs provided within the FEMA P-58 methodology (FEMA 2012) were based on the damaged surface area of each wall. As such, Eq. 4.4 can be rewritten as:

$$L_S = BRC \times \left(\frac{A_{S3-L}}{A_T} \times \sum_{i=1}^{N} \left(P(F_{S3-L})_i \times RCS_i \right) + \frac{A_{S3-S}}{A_T} \sum_{i=1}^{N} \left(P(F_{S3-S})_i \times RCS_i \right) \right) \qquad (4.5)$$

Where, within the building floors expected to experience damage, A_{S3-L} and A_{S3-S} are the surface areas of Wall S3-L and Wall S3-S, respectively, while A_T is the total surface area of all SFRS walls. Assuming that RCS_i is the same for both walls, and defining the overall system fragility at damage state *i*, $P(F)_i$, as the probability of the overall system having that value of RCS_i, Eqs. 4.3 and 4.5 can be used to estimate the overall system fragility at each damage state as following:

$$P(F)_i = \frac{A_{S3-L}}{A_T} \times P(F_{S3-L})_i + \frac{A_{S3-S}}{A_T} \times P(F_{S3-S})_i \tag{4.6}$$

4.11.2 Component Strengths Approach

The demand on the structure can be quantified using a variety of parameters, including base shears, base moments and drifts. Cornell et al. (2002) suggested that for any of these engineering demand parameters, the median seismic demand, S_d, can be represented by a power model as:

$$S_d = a(IM)^b \tag{4.7}$$

Where IM is the seismic intensity measure of choice and both a and b are the regression coefficients. The regression used to estimate the parameters a and b is facilitated by taking the natural logarithm of both sides of Eq. (4.7), resulting in the linear form of Eq. (4.8):

$$\ln(S_d) = \ln(a) + b\ln(IM) \tag{4.8}$$

For each analysis, base shears were recorded and plotted versus the spectral acceleration, S_T, for that ground motion. Regression analyses of these data were then performed to determine a and b for each wall. The confidence level in this estimate increases as the number of simulations increases. In this chapter, 440 simulations (44 ground motions scaled 10 times each) were considered to be adequate to illustrate the methodology presented and to achieve the balance between the desired confidence level and the computational time

(Cornell et al. 2002). At each value of S_T, Fig. 4.8 shows the proportion of the building base shear that is carried by each wall type, and compares the values that were computed from time history analysis to those computed using Eq. (4.7) with the coefficients from Table 4.4. As can be seen in Fig. 4.8 and Table 4.4, R^2 values for all walls show how well the curves fit the data. As such, the system-level fragility, $P(F)_i$, can be estimated for the building archetype in the North-South direction, for example, as a function of the base shears, V_{S3-L} and V_{S3-S} of Wall S3-L and Wall S3-S, respectively:

$$P(F)_i = \frac{V_{S3-L}}{V_{S3-L} + V_{S3-S}} \times P(F_{S3-L})_i + \frac{V_{S3-S}}{V_{S3-L} + V_{S3-S}} \times P(F_{S3-S})_i \qquad (4.9)$$

4.11.3 Discussion of the System-Level Fragility Approaches

Figures 4.9 (a and b) compare the fragility curves of the RM components with the overall system-level fragility curves in the North-South and East-West directions, respectively, at the *Slight*, *Moderate* and *Severe* damage states. The system-level fragilities were calculated based on the seismic loss and the strength contribution approaches using Eqs. 4.6 and 4.9, respectively. The figures show the consistency between the two approaches for estimating the system-level fragility of the building archetype for all the damage states. For instance, the median values of spectral acceleration for the *Moderate* damage state using the seismic loss and the strength contribution in the East-West direction are 3.2g and 3.0g, respectively, a difference of only 7%. Moreover, the building as a system is neither more fragile than the most vulnerable individual component (i.e. lower bound of *Series* systems) nor less fragile than the least vulnerable individual component (i.e. upper bound of *Parallel* systems) for any of the damage states considered. For example, the median values for the *Severe* damage state of Wall S3-L and Wall S3-S in the North-South direction are 3.3g and 3.9g, respectively, whereas the corresponding value for the entire building system is 3.5g using the seismic loss contribution approach.

4.12 CONCLUSIONS

This chapter proposed a new methodology, based on two different approaches, for developing system-level seismic fragility curves. The contributions of individual/component walls were combined based on their seismic losses or their strengths to determine the building system fragility curves in each direction. Within the scope of the study, the methodology has been applied to RM shear wall buildings with boundary elements in an effort towards defining the seismic resilience of such building systems. In this respect, a RM building archetype was represented by a three-dimensional model developed using OpenSees, which was experimentally validated, showing the effectiveness of different slab modelling techniques to simulate the different levels of coupling that are available in RM construction practice. The model satisfies the FEMA P695 (FEMA 2009) methodology requirements in terms of simulating stiffness, strength, and inelastic deformation under reversed cyclic loading. Subsequently, the model was subjected to a suite of ground motions as recommended in the methodology and incremental dynamic analyses were performed to generate individual component fragilities at different damage states.

The results showed the good agreement between the methodology's two approaches in estimating the system-level fragility of the building archetype for all the damage states. For the building studied, the results of the two approaches were also consistent, where the maximum difference between the two approaches at any considered damage state was 7%. In addition, the results showed that the building as a system is neither more fragile than the most vulnerable individual component nor less fragile than the least vulnerable individual component. This indicates that considering the fragility of all the components would provide a more rational approach for subsequent system-resilience evaluation.

The analyses in this chapter focused on a four-story RM shear wall building with a specific configuration of boundary elements. More archetypes with different numbers of stories and configurations, as well as different SFRS, should be studied to verify the methodology presented in this chapter. Additional full scale experimental tests would also be useful in generating better numerical models and understanding the influence of damage on the overall seismic performance of the building.

4.13 ACKNOWLEDGMENTS

The financial support for this project was provided through the Natural Sciences and Engineering Research Council (NSERC) of Canada and the Canada Masonry Design Centre (CMDC). Support was also provided by the McMaster University Centre for Effective Design of Structures (CEDS), funded through the Ontario Research and Development Challenge Fund (ORDCF) of the Ministry of Research and Innovation (MRI) as well as the McMaster Institute for Multi-hazard Systemic Risk Studies (INTERFACE).

4.14 NOTATION

The following symbols are used in this chapter:

a	=	Regression coefficient;
A	=	Surface area of the wall;
b	=	Regression coefficient;
BRC	=	Seismic force resisting system replacement cost;
C_d	=	Deflection amplification factor;
CRC	=	Component replacement cost;
C_u	=	Coefficient for upper limit on calculated period;
D	=	Dead Load;
D_{max}	=	Maximum spectral acceleration intensity of SDC D;
E_m	=	Masonry modulus of elasticity;
f'_m	=	Unconfined masonry compressive strength;
f'_{mc}	=	Confined masonry compressive strength;
f_{yh}	=	Horizontal reinforcement yield strength;
f_{yv}	=	Vertical reinforcement yield strength;
g	=	Acceleration due to gravity;
h	=	Building height;
IM	=	Intensity measure of the ground motion;
L	=	Live load;
L_S	=	Structural losses;
m	=	Number of components;
N	=	Number of damage states;
$P(F)_i$	=	Probability of damage of the system;
R	=	Response modification factor;
R^2	=	Correlation coefficient;
RCS_i	=	Structural repair cost ratio at given damage state;
S_d	=	Median seismic demand;
S_{Slight}	=	Median spectral acceleration at *Slight* damage state;
$S_{Moderate}$	=	Median spectral acceleration at *Moderate* damage state;
S_{Severe}	=	Median spectral acceleration at *Severe* damage state;
S_T	=	Spectral Acceleration;
T	=	Code fundamental period;
T_a	=	Approximate fundamental period;
V	=	Base shear of wall;
ε_m	=	Strain at maximum compressive strength of unconfined masonry;
ε_{mc}	=	Strain at maximum compressive strength of confined masonry;
ρ_v	=	Vertical reinforcement ratio;
ρ_h	=	Horizontal reinforcement ratio; and
Ω_0	=	System overstrength factor.

4.15 REFERENCES

ASCE/SEI (Structural Engineering Institute). (2010). "Minimum design loads for buildings and other structures." *ASCE/SEI 7-10*, Reston, VA.

ATC. (2009). *Damage states and fragility curves for reinforced masonry shear walls: Background document*, FEMA 58-1/BD-3.8.10. Washington, DC.

Baker, J. W. (2015). "Efficient analytical fragility function fitting using dynamic structural analysis." *Earthquake Spectra*, 31(1), 579-599.

Banting, B. and El-Dakhakhni, W. (2012). "Force-and displacement-based seismic performance parameters for reinforced masonry structural walls with boundary elements." *J. Struct. Eng.*, 10.1061/(ASCE)ST.1943-541X.0000572, 1477–1491.

Banting, B. and El-Dakhakhni, W. (2014). "Seismic performance quantification of reinforced masonry structural walls with boundary elements." *J. Struct. Eng.*, 10.1061/(ASCE) ST.1943-541X.0000895, 04014001.

Bohl, A., and Adebar, P. (2011). "Plastic hinge lengths in high-rise concrete shear walls." *ACI Struct. J.*, 108(2), 148-157.

Boole, G. (1854). *An investigation of the laws of thought: on which are founded the mathematical theories of logic and probabilities*. Dover Publications, New York.

Calabrese, A. (2008). "Numerical issues in distributed inelasticity modelling of RC Frame elements for seismic analysis." Master thesis, Istituto Universitario di Studi Superiori di Pavia Università degli Studi di Pavia, Italy.

Canadian Standards Association (CSA). (2014) “Design of masonry structures.” CSA S304-14, Mississauga, Canada.

Chang, G.A. and Mander, J.B. (1994). “Seismic energy based fatigue damage analysis of bridge columns: Part 1 – evaluation of seismic capacity.” *NCEER Technical Report* No. NCEER-94-0006 State University of New York, Buffalo, N.Y.

Choi, E., DesRoches, R., and Nielson, B. (2004). “Seismic fragility of typical bridges in moderate seismic zones.” *Engineering Structures*, 26(2), 187-199.

Cornell, C. A. (1967). “Bounds on the reliability of structural systems.” *Journal of the Structural Division*, 93(1), 171-200.

Cornell, C. A., Jalayer, F., Hamburger, R. O., and Foutch, D. A. (2002). “Probabilistic basis for 2000 SAC federal emergency management agency steel moment frame guidelines.” *J. Struct. Eng.*, 128(4), 526-533.

Erberik, M. A. (2008). “Generation of fragility curves for Turkish masonry buildings considering in-plane failure modes.” *Earthquake Engineering and Structural Dynamics*, 37(3), 387-405.

Ezzeldin, M., Wiebe, L., and El-Dakhakhni, W. (2016a). “Seismic collapse risk assessment of reinforced masonry walls with boundary elements using the FEMA P695 methodology.” *J. Struct. Eng.*, 142(11), 04016108.

Ezzeldin, M., El-Dakhakhni, W., and Wiebe, L. (2016b). “Experimental

Assessment of the System-Level Seismic Performance of an Asymmetrical Reinforced Concrete Block Wall Building with Boundary Elements." *J. Struct. Eng*., 10.1061/(ASCE)ST.1943-541X.0001790.

FEMA. (2003). *Multi-hazard loss estimation methodology, earthquake model*, HAZUS-MR4, *technical manual*, Washington, DC.

FEMA. (2009). "*Quantification of building seismic performance factors*." *FEMA P695*, Washington, DC.

FEMA. (2012). "*Seismic performance assessment of buildings.*" *FEMA P58-1*, Washington, DC.

Gehl, P., Seyedi, D. M., and Douglas, J. (2013). "Vector-valued fragility functions for seismic risk evaluation." *Bulletin of Earthquake Engineering*, 11(2), 365-384.

Grimmelt, M. J., and Schuëller, G. I. (1983). "Benchmark study on methods to determine collapse failure probabilities of redundant structures." *Structural Safety*, 1(2), 93-106.

Heerema, P., Shedid, M., Konstantinidis, D., and El-Dakhakhni, W. (2015). "System-level seismic performance assessment of an asymmetrical reinforced concrete block shear wall building." *J. Struct. Eng*., 141(12), 04015047.

Lagomarsino, S., and Cattari, S. (2013). "Seismic vulnerability of existing buildings." *Seismic Vulnerability of Structures*, 1-62.

Lagomarsino, S., and Giovinazzi, S. (2006). "Macroseismic and mechanical models for the vulnerability and damage assessment of current buildings." *Bulletin of Earthquake Engineering*, 4(4), 415-443.

Lu, X., Xie, L., Guan, H., Huang, Y., and Lu, X. (2015). "A shear wall element for nonlinear seismic analysis of super-tall buildings using OpenSees." *Finite Elements in Analysis and Design*, 98, 14-25.

Mander, J. B., Priestley, M. J. N. and Park, R. (1988). "Theoretical stress-strain model for confined concrete." *J. Struct. Eng*., 114(8), 1804–1826.

Masonry Standards Joint Committee. (MSJC). (2013). "Building code requirements and specifications for masonry structures." *TMS 402-13/ ACI 530-13/ASCE 5-13*, the Masonry Society, American Society of Civil Engineers, Boulder, New York/American Concrete Institute, and Detroit, USA.

McKenna, F., Fenves, GL., and Scott, MH. (2013). "Open System for Earthquake Engineering Simulation." University of California, Berkeley, CA, 2000. Available from: *http://opensees.berkeley.edu*, Version 2.4.3.

Melchers, R.E. (1999). *Structural reliability analysis and prediction*. John Wiley & Son Ltd.

Murcia-Delso, J., and Shing, P. B. (2012). "Fragility analysis of reinforced masonry shear walls." *Earthquake Spectra*, 28(4), 1523-1547.

Nielson, B. G., and Bowers, M. E. (2007). Seismic Bridge Fragilities for Post-Design Verification. *In 1st US-Italy Seismic Bridge Workshop*.

Nielson, B. G., and DesRoches, R. (2007). "Seismic fragility methodology for highway bridges using a component level approach." *Earthquake Engineering and Structural Dynamics*, 36(6), 823-839.

NIST. (2005). "Development of NIST measurement science R&D roadmap: earthquake risk reduction in buildings." *NIST GCR 13-917-23*, Gaithersburg, MD.

NIST. (2010). "Evaluation of the FEMA P695 methodology for quantification of building seismic performance factors." *NIST GCR 10-917-8*, Gaithersburg, MD.

Oropeza, M., Michel, C., and Lestuzzi, P. (2010). "A simplified analytical methodology for fragility curves estimation in existing buildings." *14th European Conf. of Earthquake Engineering*, Ohrid, Macedonia.

Pagnini, L. C., Vicente, R., Lagomarsino, S., and Varum, H. (2011). "A mechanical model for the seismic vulnerability assessment of old masonry buildings." *Earthquakes and structures*, 2(1), 25-42.

Pitilakis, K., Crowley, H., and Kaynia, A. (2014). "SYNER-G: typology definition and fragility functions for physical elements at seismic risk." *Geotechnical, Geological and Earthquake Engineering*, 27.

Priestley, M. J. N. (1976). "Cyclic Testing of Heavily Reinforced Concrete Masonry Shear Walls." *Research Report 76-12*, University of Canterbury, Christchurch, New Zealand.

Ranf, R. T., Eberhard, M. O., and Malone, S. (2007). "Post-earthquake prioritization of bridge inspections." *Earthquake Spectra*, 23(1), 131-146.

Rossetto, T., Ioannou, I., and Grant, D. N. (2013). “Existing empirical fragility and vulnerability relationships: compendium and guide for selection.” *GEM Foundation*, Pavia, Italy.

Sabetta, F., Goretti, A., and Lucantoni, A. (1998). “Empirical fragility curves from damage surveys and estimated strong ground motion.” *11th European conf. on earthquake engineering*, Paris, France.

Shedid, M. T., El-Dakhakhni, W. W. and Drysdale, R. G. (2010). “Alternative strategies to enhance the seismic performance of reinforced concrete-block shear wall systems.” *J. Struct. Eng*., 136(6), 676-689.

Shing, P. B., Noland, J. L., Spaeh, H. P., Klamerus, E. W., and Schuller, M. P., (1991). “Response of Single-Story Reinforced Masonry Shear Walls to In-Plane Lateral Loads.” *Report No. 3.1(a)-2,* US-Japan Coordinated Program for Masonry Building Research, University of Colorado at Boulder, Boulder.

Siyam, M., El-Dakhakhni, W., Shedid, M., and Drysdale, R. (2015). "Seismic response evaluation of ductile reinforced concrete block structural walls. I: experimental results and force-based design parameters." *J. Perform. Constr. Facil.* , 10.1061/(ASCE)CF.1943-5509.0000794, 04015066.

Spence, R. J. S., Coburn, A. W., Pomonis, A., and Sakai, S. (1992). “Correlation of ground motion with building damage: the definition of a new damage-based seismic intensity scale.” *10th World Conf. on Earthquake Engineering*, Madrid, Spain.

Vamvatsikos, D., and Cornell, A. (2002). "Incremental dynamic analysis." *Earthq. Eng. Struct. Dyn.*, 31(3), 491–514.

Voon, K. C., and Ingham, J. M. (2006). "Experimental in-plane shear strength investigation of reinforced concrete masonry walls." *J. Struct. Eng*., 132(3), 400-408.

Table 4.1 Summary of Material Properties within *Building II* and *Building IV*.

Building	f'_m (MPa)	f_{yv} (MPa)	f_{yh} (MPa)
Building II[a]	20.9	489	498
Building IV[b]	20.5	457	487

[a] Based on data from Heerema et al. (2015)

[b] Based on data from Ezzeldin et al. (2016b)

Table 4.2 Maximum Error for the Predicted Values of Peak Lateral Load and Energy Dissipation during one Cycle using the Numerical Model versus the Experimental Data.

Building	Maximum Error	
	Lateral Load	Energy Dissipation
Building II[a]	13%	12%
Building IV[b]	14%	14%

[a] Based on data from Heerema et al. (2015)

[b] Based on data from Ezzeldin et al. (2016b)

Table 4.3 Dimensions and Reinforcement Details of RM Walls with Boundary Elements.

Wall ID Number	Height (m)	Length (m)	Vertical Reinforcement	ρ_v %	Horizontal Reinforcement	ρ_h %	Aspect Ratio
S3-L	12.20	9.75	8 # 6 + 8 # 6	0.216	# 5 @ 800 mm	0.127	1.25
S3-S	12.20	6.10	8 # 3 + 6 # 3	0.076	# 5 @ 800 mm	0.127	2.00
S13-L	12.20	9.75	8 # 8 + 8 # 8	0.387	# 6 @ 800 mm	0.180	1.25
S13-S	12.20	6.10	8 # 5 + 6 # 5	0.205	# 6 @ 800 mm	0.180	2.00

Table 4.4 Seismic Demand Regression Coefficients for Eq. 4.7

Wall ID Number	a	b	R^2
S3-L	3859	0.51	0.90
S3-S	1770	0.69	0.88
S13-L	3600	0.41	0.89
S13-S	1545	0.54	0.89

.

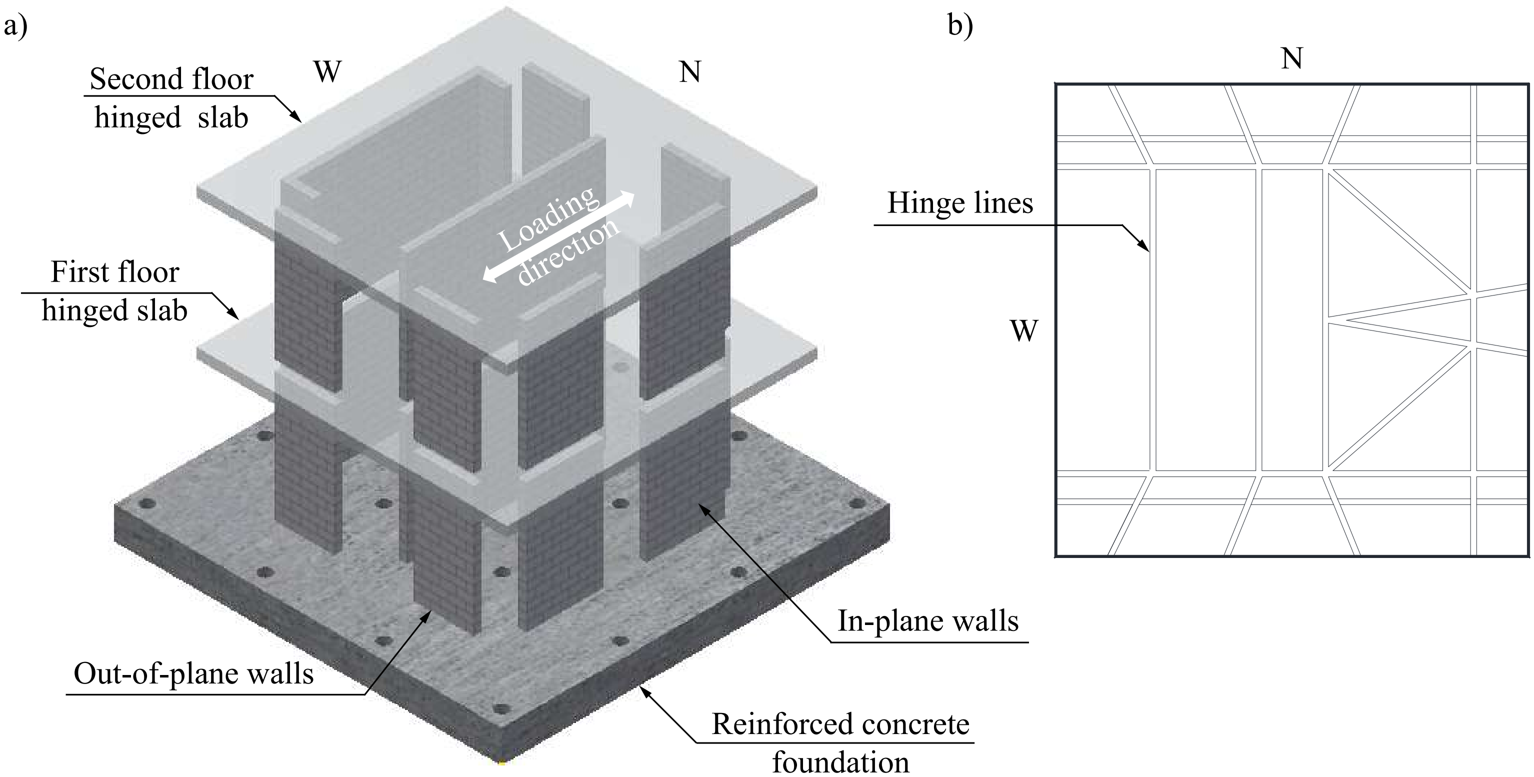

Fig. 4.1: *Building II* configuration; a) Isometric view from South-East direction; b) RC slab detailed with hinge lines.

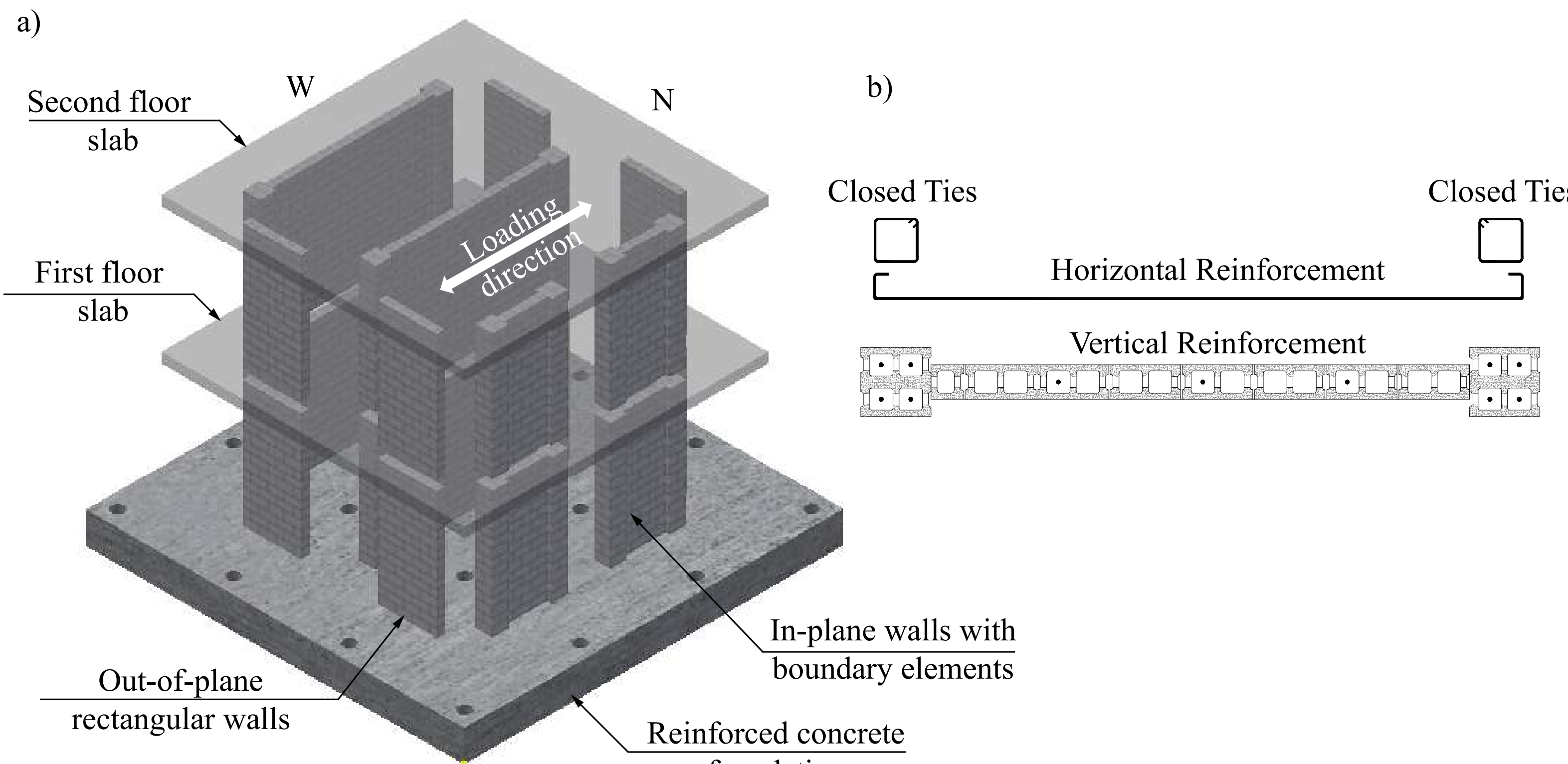

Fig. 4.2: *Building IV* configuration; a) Isometric view from South-East direction; b) Cross section of in-plane walls with boundary elements configuration.

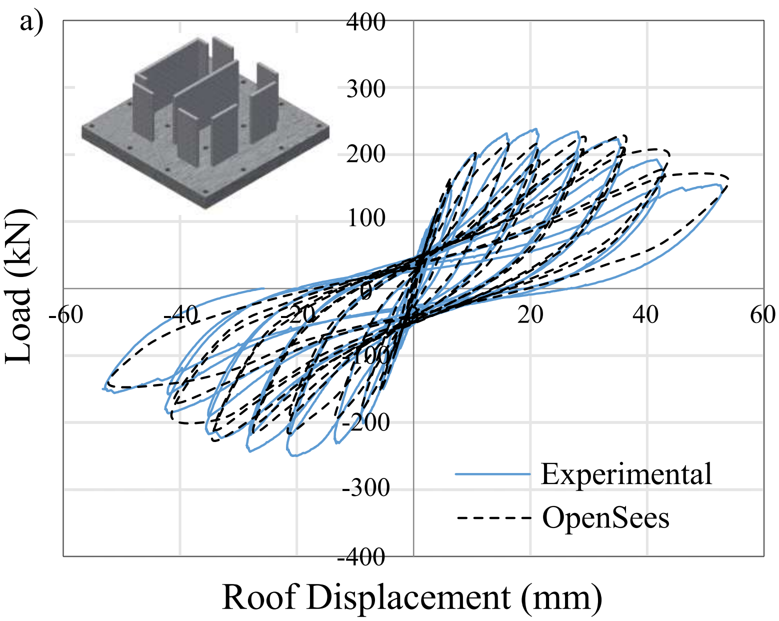

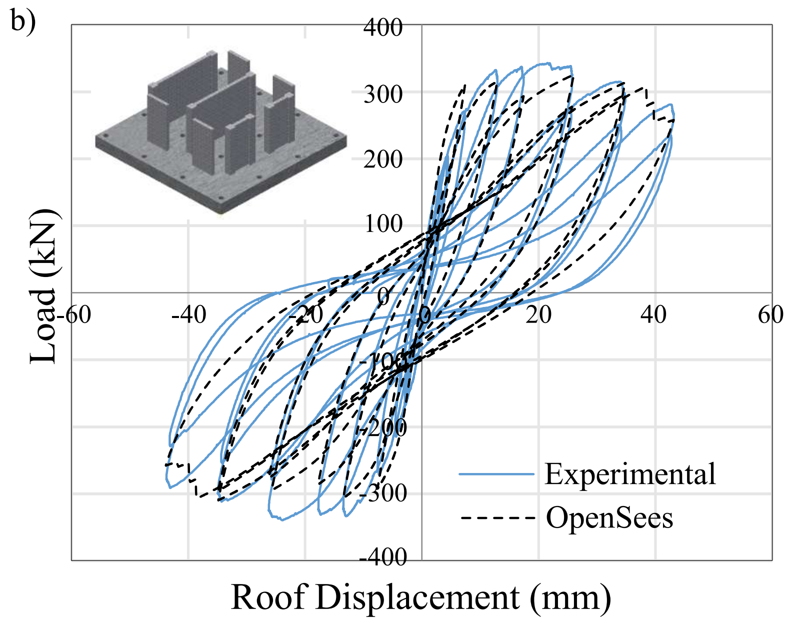

Fig. 4.3: Experimental and numerical hysteresis loops;
a) *Building II* (data from Heerema et al. 2015); b) *Building IV* (data from Ezzeldin et al. 2016b).

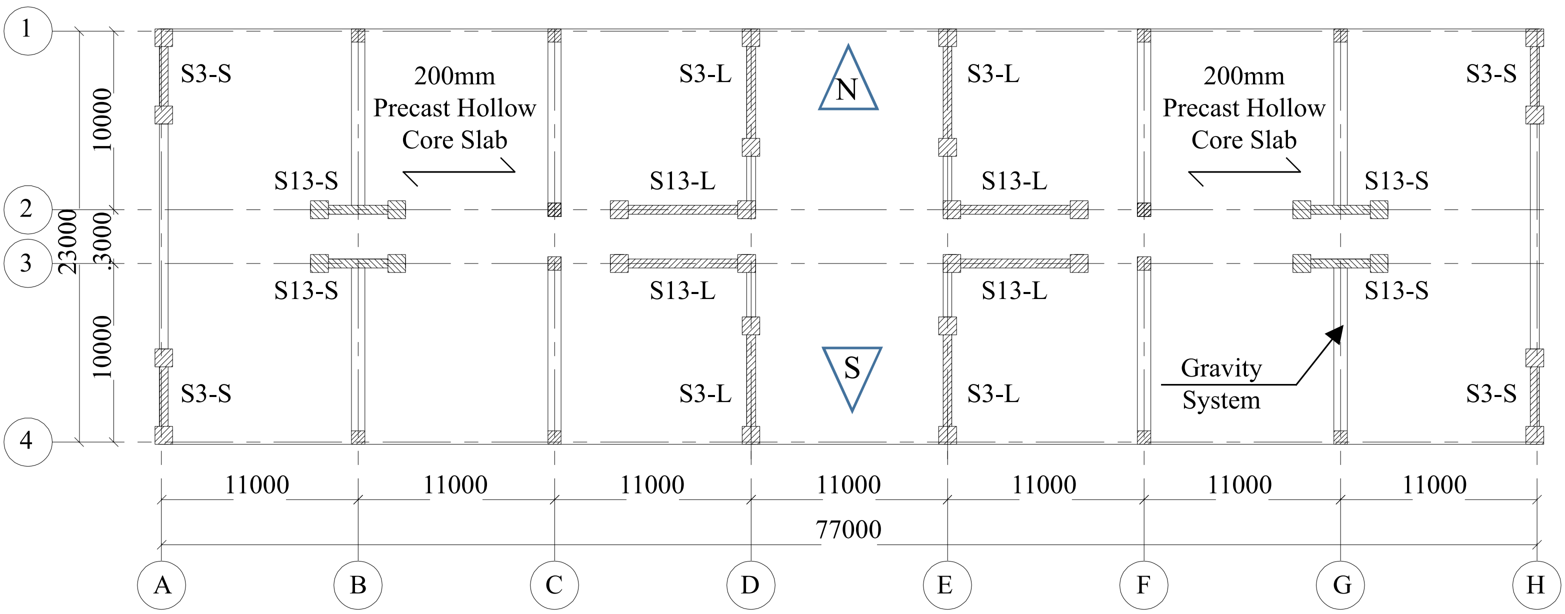

Fig. 4.4: Four-story reinforced masonry shear wall building archetype with boundary element configuration (SDC D_{max}).

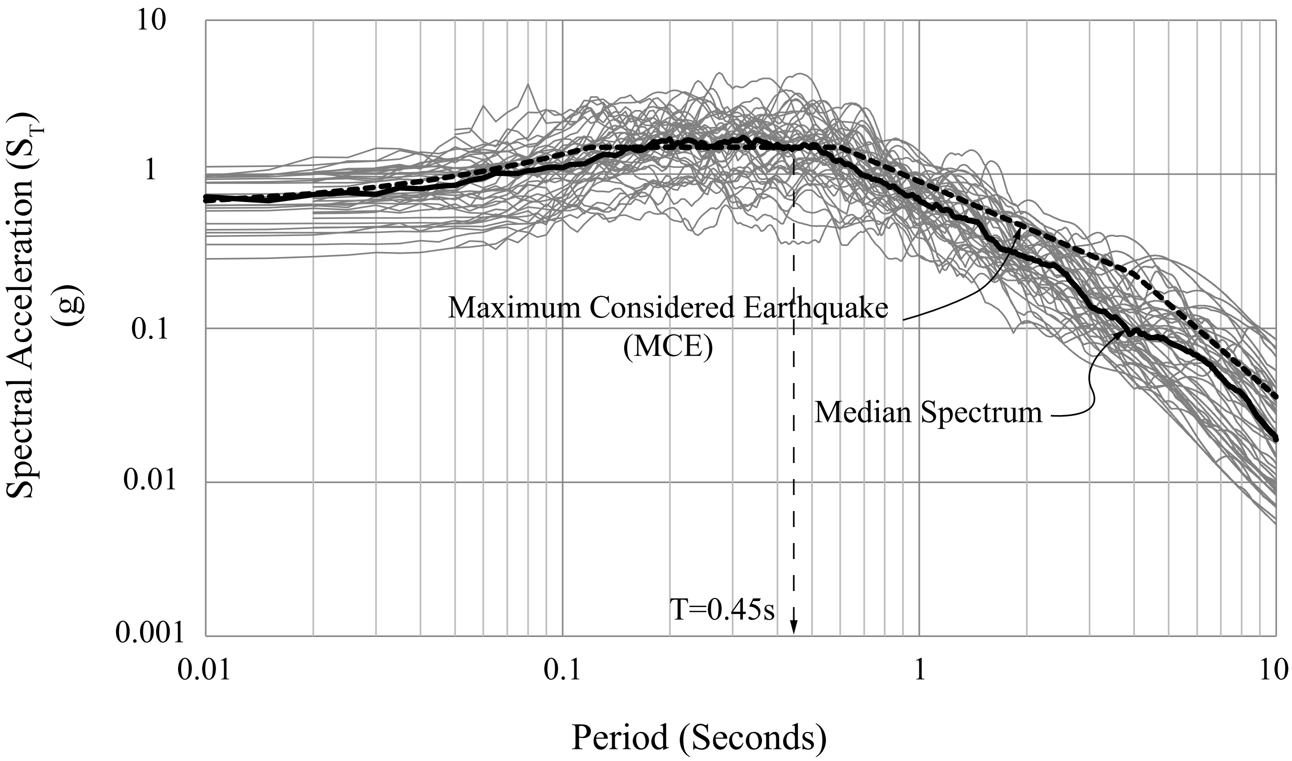

Fig. 4.5: Response spectra of the 44 individual components of the normalized record set, median response spectrum of the total record set and Maximum Considered Earthquake (MCE) for SDC Dmax.

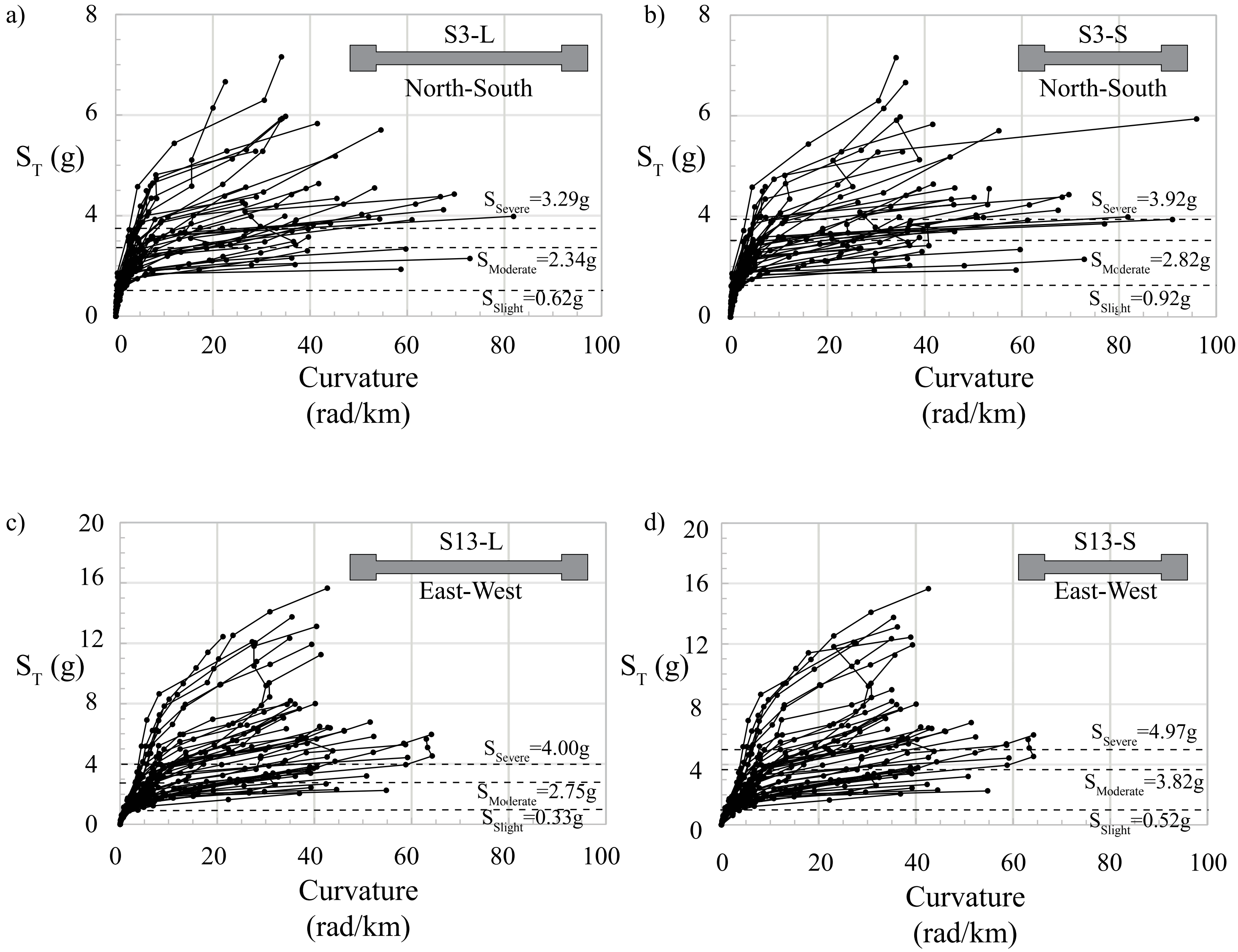

Fig. 4.6: Incremental Dynamic Analysis (IDA) response plot of spectral acceleration versus maximum curvature: (a) Wall S3-L (North-South direction); (b) Wall S3-S (North-South direction); (c) Wall S13-L (East-West direction); (d) Wall S13-S (East-West direction).

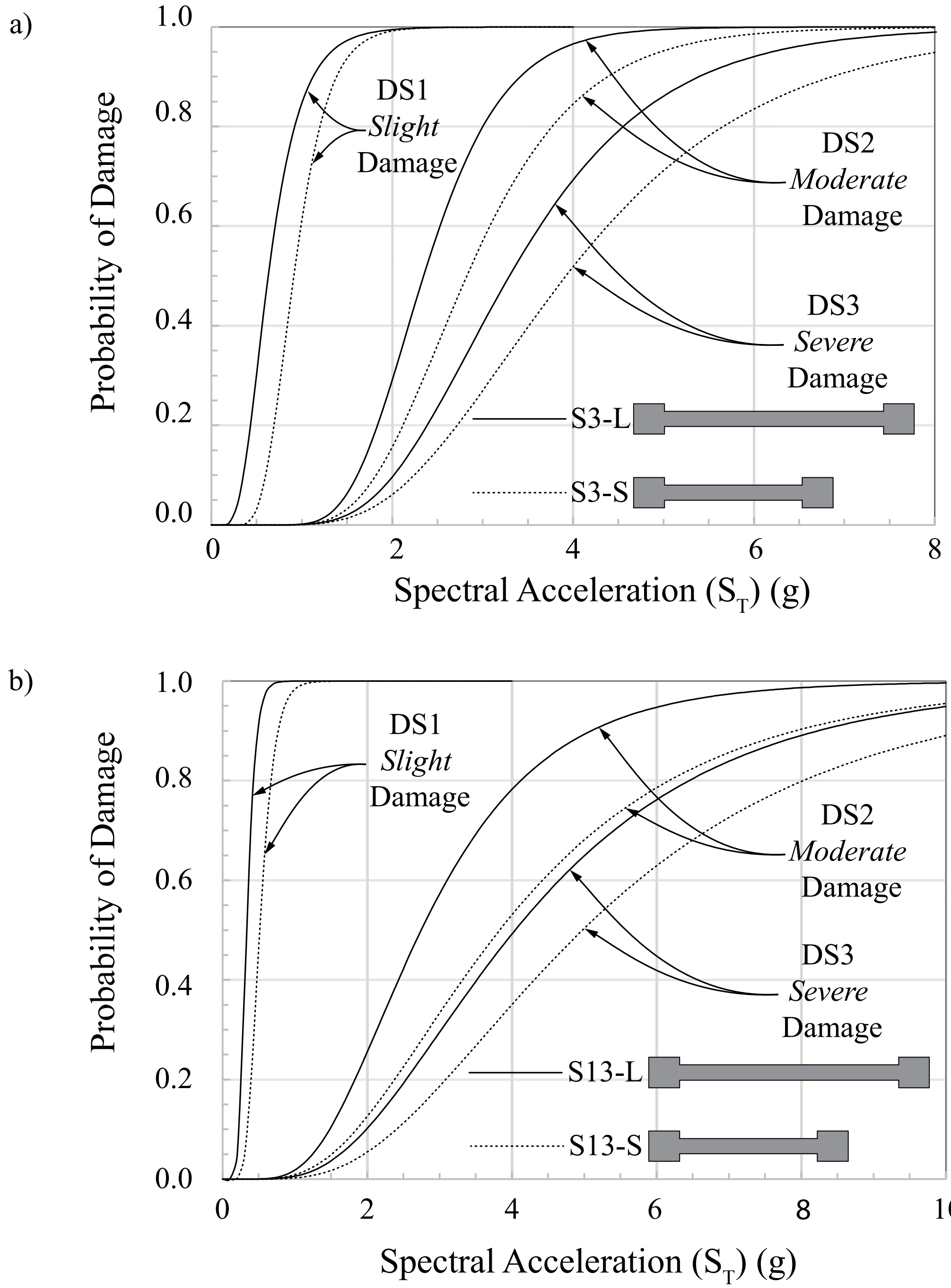

Fig. 4.7: Component fragility curves at *Slight* (DS1), *Moderate* (DS2) and *Severe* (DS3) damage states for: (a) Wall S3-L (North-South direction) and Wall S3-S (North-South direction); (b) Wall S13-L (East-West direction) and Wall S13-S (East-West direction).

a)

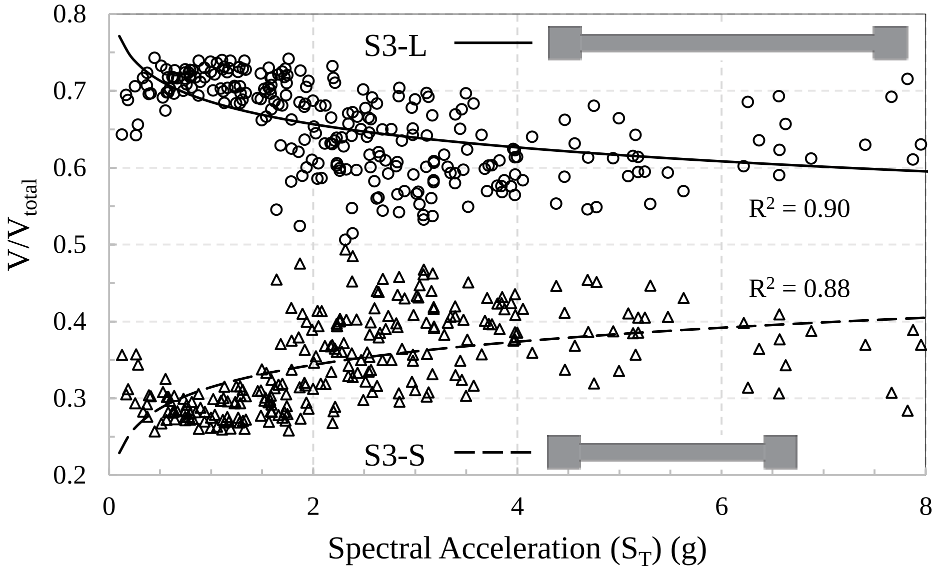

b)

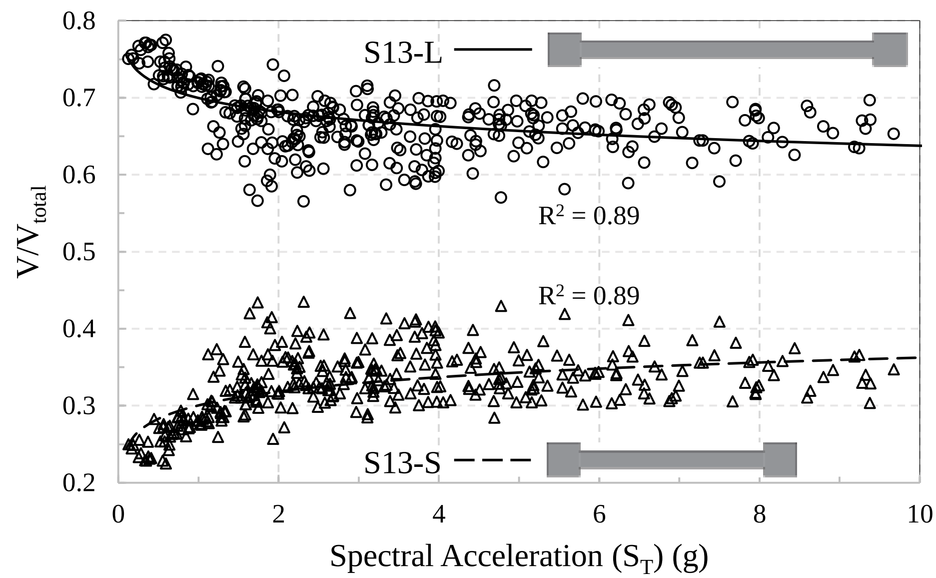

Fig. 4.8: Component to system-level strength contribution :
(a) Wall S3-L (North-South direction) and Wall S3-S (North-South direction);
(b) Wall S13-L (East-West direction) and Wall S13-S (East-West direction).

a)

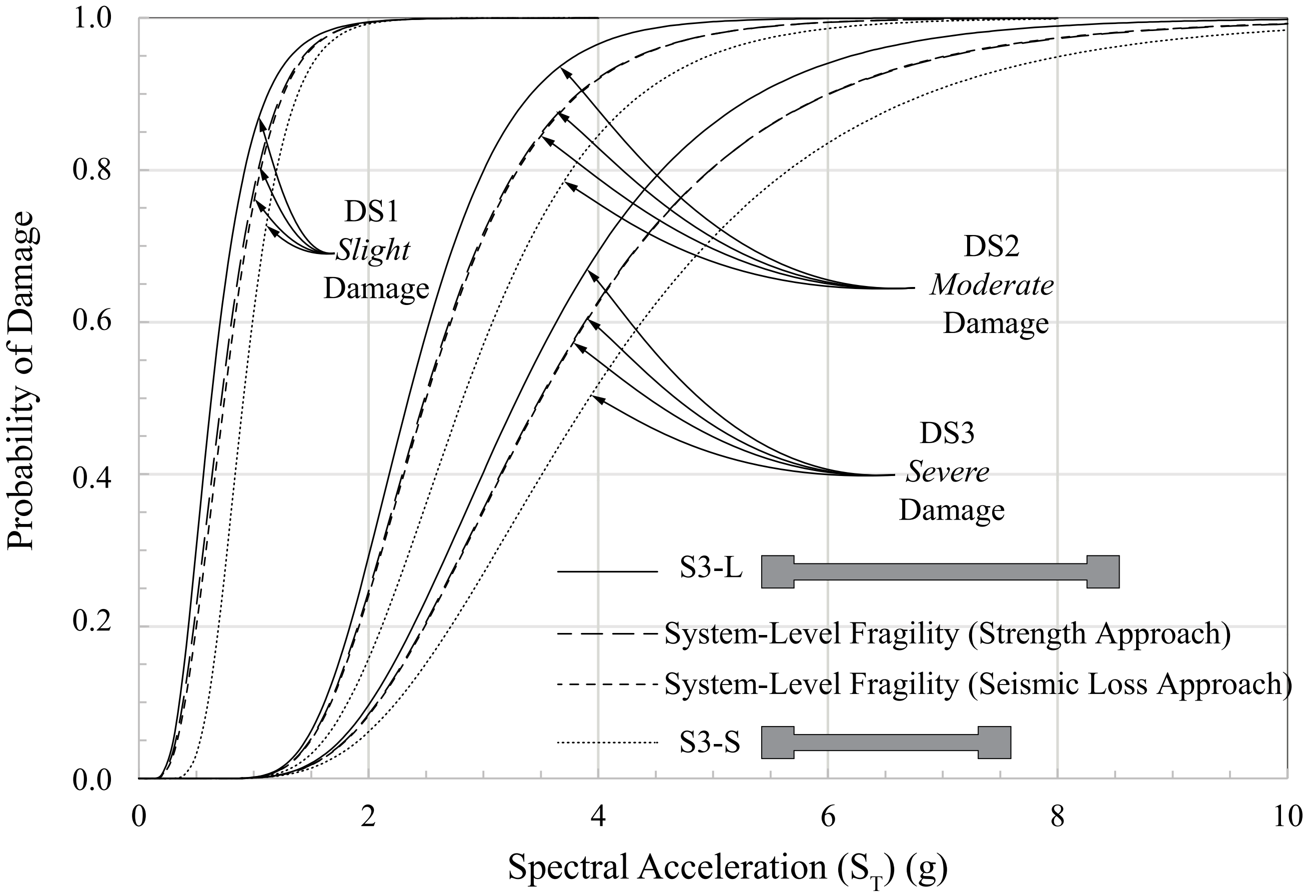

Fig. 4.9: System and component-level fragility curves at *Slight* (DS1), *Moderate* (DS2) and *Severe* (DS3) damage states in the: (a) North-South direction.

b)

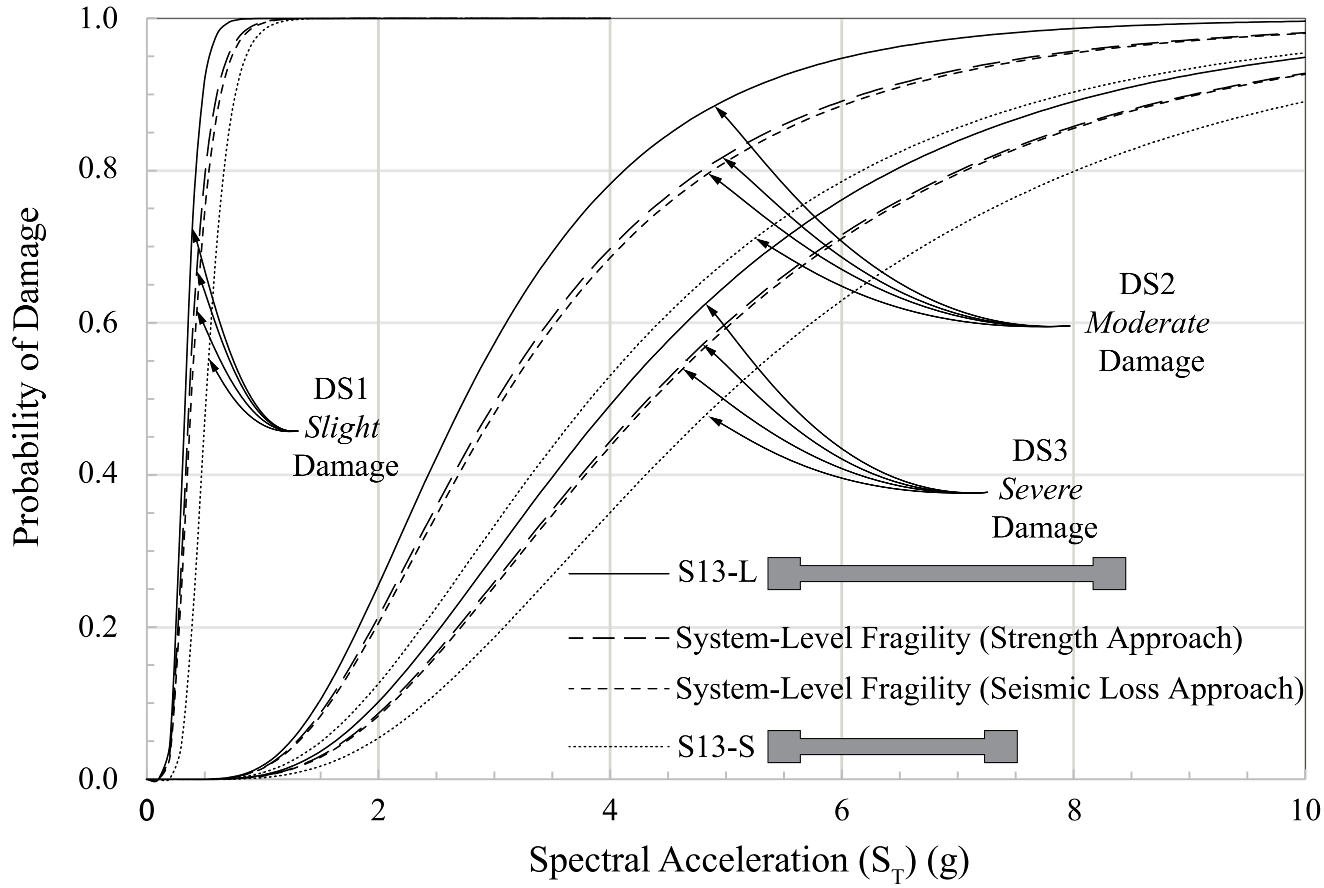

Fig. 4.9 (cont.): System and component-level fragility curves at *Slight* (DS1), *Moderate* (DS2) and *Severe* (DS3) damage states in the: (b) East-West direction.

CHAPTER 5
REINFORCED MASONRY BUILDING SEISMIC RESPONSE MODELS FOR ASCE/SEI-41

5.1 ABSTRACT

The development of models to predict the inelastic behavior of the individual components of a building system at different performance levels is an essential step in performing nonlinear static and dynamic analyses, as recommended in ASCE/SEI 41-13, "*Seismic Evaluation and Retrofit of Existing Buildings*". However, current methodologies for generating nonlinear models for reinforced masonry (RM) buildings do not adequately account for various system-level aspects, such as the influence of the floor slab stiffness. Several recent studies have shown that these aspects would significantly alter the overall building response under seismic loading. In addition, although ASCE/SEI 41-13 defines the capacity parameters of RM shear walls with rectangular cross sections through a standardized force-displacement backbone relationship, no corresponding relationships are available for RM shear walls with boundary elements. Moreover, ASCE/SEI 41-13 does not provide the necessary hysteretic parameters required to define the cyclic behavior of any type of RM shear walls under seismic loading. To address these issues, this chapter focuses on applying two ASCE/SEI 41 models from reinforced concrete (RC) to RM. The first model is a backbone model for RM shear wall buildings without and with boundary elements. The experimentally validated modeling approach shows that RC parameters are

applicable, but it is critical to include the out-of-plane stiffness of the floor diaphragms when evaluating the overall building response. The second model is a concentrated plasticity (spring) model to simulate the hysteretic response of RM shear wall buildings with different configurations. Finally, the developed numerical hysteretic responses are compared with experimental results in terms of the most relevant characteristics, including the initial stiffness, peak load, and stiffness and strength degradation. This chapter aims at presenting useful system-level response prediction tools for the nonlinear static and dynamic procedures specified in ASCE/SEI 41-13.

5.2 INTRODUCTION

Nonlinear analysis is a common tool in in both earthquake engineering practice and research because it provides the means to determine the inelastic structural response under earthquakes, including evaluating stiffness and strength degradation, as required by modern performance-based design approaches. For this reason, nonlinear analysis plays an important role in the seismic risk assessment of new and existing buildings. For example, FEMA 440 (FEMA 2005) provides a comprehensive methodology for the use of nonlinear analysis for the seismic evaluation and retrofit of existing buildings. In addition, nonlinear analysis is being used to improve and validate design codes and standards. For example, FEMA P695 (FEMA 2009) outlines procedures to generate collapse fragility curves and assess the collapse risk of buildings, in order to assess the adequacy of seismic performance factors in current codes and standards. Moreover, nonlinear analysis facilitates the probabilistic assessment of the seismic performance of buildings following FEMA P58 (FEMA 2012).

Nonlinear analyses require nonlinear structural response models that are capable of predicting the inelastic behavior of the individual seismic force resisting system (SFRS) components at different performance levels. These nonlinear models are typically presented in the form of backbone relationships (for Nonlinear Static Procedure, NSP) or hysteretic models (for Nonlinear Dynamic Procedure, NDP) as specified in ASCE/SEI 41-13 (ASCE 2014). Backbone and hysteretic models define the response that would be observed for a component tested under monotonic loading and cyclic loading, respectively. Both models are generally expected to capture post-peak softening response, and stiffness and strength degradation. In addition, hysteretic models also incorporate unloading and reloading stiffnesses, cyclic deterioration and pinching behavior.

The studies that have been conducted to develop nonlinear models for reinforced masonry (RM) shear walls can be mainly categorized by the degree of model idealization as: (1) continuum finite element models, where the nonlinear behavior of the masonry, longitudinal and shear reinforcement that comprise the shear wall are modelled explicitly (e.g. Mojsilovic and Marti 1997; Lourenço and Rots 1997; Guinea et al. 2000; Giambanco et al. 2001; Abdellatef 2011); (2) distributed plasticity (fiber) models, where numerical integration is used through the RM shear wall cross section and along its length to distribute plasticity (e.g.

Stavridis and Shing 2010; Karapitta et al. 2011; Siyam et al. 2015; Ezzeldin et al. 2016a); and (3) concentrated plasticity models, where all the nonlinear effects of the RM shear walls are lumped into an inelastic spring idealized by a single-degree-of-freedom relationship (e.g. moment-rotation) (Dymiotis et al. 2001; Dolšek and Fajfar 2008; Shedid et al. 2010; Andreini et al. 2014; Marques and Lourenço 2014). Although continuum finite element and distributed plasticity models can very accurately capture behaviors such as initiation of masonry cracking and steel yielding, they are nonetheless computationally intensive and have limited ability to capture strength degradation due to such factors as reinforcing bar buckling, bond slip, and shear failure (ATC 2010). Conversely, concentrated plasticity models can capture strength degradation effects and they do not require the level of detailed representation that is needed for both continuum finite element and distributed plasticity models.

Most of the published modelling studies to date have been conducted on RM walls at the component level (i.e. individual wall), with only a few studies focused on system-level response evaluation of RM walls (i.e. complete building) (e.g., Paulay 1997; Priestley et al. 2007; Ashour and El-Dakhakhni 2016; Ezzeldin et al. 2016b). Recently, several studies argued that there are specific system-level aspects (e.g. slab's in-plane and out-of-plane stiffness) that cannot be evaluated or assessed through component-level testing. For example, the in-plane slab stiffness results in different component-level strength and displacement demands from essentially identical RM shear walls (Heerema et al. 2015). In addition, Stavridis et al. (2011) and Ashour et al. (2016) both conducted experimental programs that demonstrated that slab flexural coupling was an important system-level aspect that affected the overall RM building performance. This performance included the building stiffness, lateral resistance capacity, and trend of stiffness degradation, which in turn would significantly alter the overall building response under seismic loading.

The nonlinear models described above have considered only walls with rectangular cross sections, whereas RM buildings with boundary elements are a newly proposed system within the Canadian Standards Association "Design of Masonry Structures" S304-14 (CSA 2014). RM shear walls with boundary elements are also included in the TMS 402-13/ACI 530-13/ASCE 5-13 Masonry Standards Joint Committee code (MSJC 2013) but neither design guidance nor classifications are provided dealing with such walls as a separate SFRS. The use of boundary elements in RM shear walls enhances the overall seismic performance relative to traditional RM shear walls (i.e. with rectangular cross sections) because closed ties and multiple layers of vertical bars can be accommodated within the boundary elements, thus providing a confining reinforcement cage (Shedid et al. 2010; Banting and El-Dakhakhni 2012; Ezzeldin et al. 2016a). Therefore, the nonlinear models developed in this chapter also account for RM buildings with boundary elements in order to facilitate the development of prescriptive design requirements, as recommended by the TMS 402-13/ACI 530-13/ASCE 5-13 (MSJC 2013).

The objective of this chapter is to develop backbone and hysteretic models that can be adapted to perform the NSP and NDP, respectively, for simulating the nonlinear response of RM shear wall buildings with different configurations. In this respect, a backbone analytical model is developed and validated against the experimental results reported by Ashour et al. (2016) and Ezzeldin et al. (2016c). These previous experimental programs are selected because they include walls with different configurations (i.e. without and with boundary elements) with a range of aspect ratios, from 1.5 to 4.6. A summary of these experimental programs is presented in the following section. The current parameters assigned to RM shear walls in ASCE/SEI 41-13 are then assessed and new parameters are proposed and validated. The developed backbone model is subsequently utilized to create a concentrated plasticity (spring) model in *OpenSees* to simulate the hysteretic response of RM shear wall buildings. Finally, the experimental and numerical hysteretic responses are compared in terms of the most relevant characteristics, including the initial stiffness, peak load, stiffness degradation, strength deterioration, hysteretic shape and pinching behavior at different drift levels.

5.3 SUMMARY OF THE EXPERIMENTAL PROGRAMS

Ashour et al. (2016) tested a one-third scaled two-story asymmetrical RM shear wall building (referred to as *Building III* hereafter) under displacement-controlled quasi-static fully-reversed cyclic loading, as shown in Fig. 5.1(a). *Building III* was composed of four traditional (i.e. with rectangular cross section) shear walls aligned along the loading direction ($W1_{III}$, $W2_{III}$, $W5_{III}$ and $W8_{III}$), and four other walls aligned orthogonally ($W3_{III}$, $W4_{III}$, $W6_{III}$ and $W7_{III}$), as shown in Fig. 5.1(b). The asymmetrical wall configuration with respect to the loading direction produced an eccentricity between the building floor Center of Mass, C_M , and the building Center of Rigidity, C_R, at the roof level, that engaged the torsional response of the building under the applied lateral loads. The overall height of the scaled building was 2,160 mm, comprising two floors, each 1,000 mm high (corresponding to 3,000 mm in full-scale), and reinforced concrete (RC) floors, each with dimensions of 2,400 mm × 2,400 mm in plan. The building was fixed to the laboratory strong structural floor by 16 prestressed anchors through a square RC foundation (3,000 mm × 3,000 mm).

Ezzeldin et al. (2016c) tested a similar building with the same nominal strength (to allow for direct comparison with *Building III*), referred to as *Building IV* hereafter. The RM shear walls located along the main direction of loading in *Building III* ($W1_{III}$, $W2_{III}$, $W5_{III}$ and $W8_{III}$) were replaced in *Building IV* by RM shear walls with confined boundary elements ($W1_{IV}$, $W2_{IV}$, $W5_{IV}$ and $W8_{IV}$), as shown in Figs. 5.2 (a and b). The boundary elements were adopted in *Building IV* because they allow closed ties to be used and multiple layers of vertical reinforced bars to be accommodated, thus providing a confining reinforcement cage, as shown in Fig. 5.2(c). Full details of the experimental programs can be found in Ashour et al. (2016) and Ezzeldin et al. (2016c) for *Buildings III* and *IV*, respectively.

Table 5.1 summarizes the material characteristics within *Buildings III* and *IV* reported by Ashour et al. (2016) and Ezzeldin et al. (2016c), respectively, including the masonry compressive strength of the prisms, f'_m, the masonry Young's modulus, E_m, the masonry shear modulus, G_m, the yield strength of the vertical bars, f_{yv}, and the steel reinforcement Young's modulus, E_s.

5.4 RM BACKBONE MODEL IN ASCE/SEI 41-13

The Nonlinear Static Procedure (NSP) specified in ASCE/SEI 41-13 (ASCE 2014) is a more general approach for characterizing the performance of a structure than the linear procedure, which cannot be used for structures that have long periods, major setbacks, torsional or vertical stiffness irregularities, or non-orthogonal SFRS (ASCE 2014). The NSP requires analytical models that directly incorporate the nonlinear load-deformation characteristics of RM shear walls. These models are represented by backbone curves that include strength degradation and residual strength, if any. ASCE/SEI 41-13 (ASCE 2014) provides standardized force-displacement backbone relationships using two different approaches (referred to as *Approaches 1* and *2* hereafter) for simulating the nonlinear response of RM shear walls. More details regarding the definition and the assessment of these backbone curves, using *Buildings III* and *IV*, are given in this section.

5.4.1 Current ASCE/SEI 41-13 Backbone Modeling Approaches

In *Approach 1* of ASCE/SEI 41-13 (ASCE 2014), as shown in Fig. 5.3, generalized backbone curve for RM shear walls is defined in terms of elastic and plastic ranges, where there is an elastic range from point A (unloaded point) to point B (effective yield point) and a plastic range from point B to point E (maximum drift point). At deformation levels greater than that corresponding to point E, the RM shear wall strength is essentially zero. Points C and D are also defined in the plastic range of *Approach 1* to represent the ultimate and residual strength points, respectively. ASCE/SEI 41-13 (ASCE 2014) defines the parameter “d” to represent the ultimate drift, Δ_u, up to the point where a loss of the lateral load capacity at point C occurs, the parameter “e” to represent the maximum drift, Δ_r, up to failure at point E, and the parameter “c” to represent the residual strength corresponding to points D and E. Although ASCE/SEI 41-13 (ASCE 2014) provides specific values for these parameters for RM shear walls, thus defining points B, C, and E, no parameters are given to define point D in *Approach 1*. In addition, the steep transition between points C and D can cause convergence problems in nonlinear analysis and might not even reflect the actual response of RM shear walls (ATC 2010). As such, ASCE/SEI 41-13 (ASCE 2014) proposes *Approach 2* through the use of a modified slope from point C to point E, as shown in Fig. 5.3, to represent the post-peak degrading response and avoid any computational instability.

5.4.2 Current ASCE/SEI 41-13 Backbone Model Parameters

There are three key points needed to determine the individual wall response, as shown in Fig. 5.3. For the yield strength, Q_y, a linear strain profile is used to calculate the yield moment, M_y, with a yield strain of the outermost steel reinforcement set to 0.0025. To calculate the wall ultimate strength, Q_u, based on the ultimate moment, M_u, the ultimate masonry strain is taken as 0.0025, as specified by the TMS 402-13/ACI 530-13/ASCE 5-13 (MSJC 2013). Finally, the residual strength, Q_r, is calculated by multiplying Q_u by the parameter "c" specified in ASCE/SEI 41-13 (ASCE 2014), as discussed in the previous section. For all three strength calculation cases, a bending moment diagram must be assumed to relate the moment to the lateral load. To account for the effect of slab coupling, this diagram was selected based on the results of both experimental programs (i.e. *Building III* and *Building IV*), which showed the significant effect of the diaphragm coupling in terms of changing the system-level response of the RM shear walls aligned along the main direction of loading. More specifically, the orthogonal walls resulted in a coupling moment at the top level, M_{top}, due to the effect of tension force developed at yielding of the reinforcement, T_o, in one pair of the orthogonal walls and an equal compression force, P_o, in the other pair of the orthogonal walls. The T_o in each orthogonal wall pair is equal to 180 kN and 162 kN for *Buildings III* and *IV*, respectively. As such, the coupling moment, M_{top}, is equal to the tension or compression force in one pair of the orthogonal walls multiplied by the distance between the orthogonal walls. This coupling moment is then distributed to the other walls according to their effective moment of inertia, I_e. The coupling at the first level was much less significant. These calculations are supported by the numerical model developed by Ezzeldin et al. (2016b), which indicates that the diaphragm coupling influenced the system-level behavior of *Building IV* by restraining the in-plane rotations of the walls at the top slab level with minor coupling at the first floor slab level, as shown in Figs. 5.4 (a and b). However, the diaphragm coupling decreases gradually at higher drift levels due the cracks developed within the diaphragm, until the walls of *Building IV* respond almost as cantilevers at large drifts, as shown in Fig. 5.4(c). Similar experimental observations were reported for *Building III* by Ashour and El-Dakhakhni (2016). As a simplification of this behavior, the walls aligned along the loading direction in both buildings are assumed to have linear variation of moment over the height from M_y or M_u at the base to M_{top} at the top, until reaching the ultimate point (i.e. point C), as shown in Figs. 5.5 (a and b). At the strength degradation point (i.e. point E), the walls are assumed to be unrestrained by the slab, as shown in Fig. 5.5(c). Based on these assumptions, Eqs. (5.1-a), (5.1-b) and (5.1-c) were used to calculate Q_y, Q_u and Q_r, respectively, while the bending moments (i.e. M_y, M_u, M_{top} and cM_u) used in the previous equations are given in Table 5.2. The elastic stiffness, K_y, and the yield drift, Δ_y, were calculated using Eqs. (5.2) and (5.3), respectively, according to Paulay and

Priestley (1992).

$$Q_y = \frac{M_{top} + M_y}{h} \qquad (5.1\text{-a}) \qquad\qquad Q_u = \frac{M_{top} + M_u}{h} \qquad (5.1\text{-b})$$

$$Q_r = \frac{cM_u}{h} \qquad (5.1\text{-c})$$

$$K_y = \frac{1}{\dfrac{h^3}{12E_m I_e} + \dfrac{1.2h}{G_m A_e}} \qquad (5.2) \qquad\qquad \Delta_y = \frac{Q_y}{K_y} \qquad (5.3)$$

In the equations above, h is the wall height, the "c" parameter is determined as discussed earlier, E_m is the masonry Young's modulus, G_m is the masonry shear modulus, I_e is the wall effective moment of inertia and A_e is the effective masonry wall cross sectional area. Eq. (5.4) was used to calculate I_e and A_e, according to Paulay and Priestley (1992), where α is a reduction factor, I_g is the wall gross moment of inertia, A_g is the gross masonry wall cross sectional area, f_{yv} is the yield strength of the vertical bars, f'_m is the masonry compressive strength and P is the axial load on the wall. These material characteristics are given in Table 5.1 for *Buildings III* and *IV*.

$$I_e = \alpha I_g \qquad\qquad A_e = \alpha A_g \qquad\qquad \alpha = \left(\frac{100}{f_{yv}} + \frac{P}{f'_m A_g}\right) \qquad (5.4)$$

Finally, while ASCE/SEI 41-13 (ASCE 2014) provides the "c", "d" and "e" parameters to determine Δ_u and Δ_r, respectively, of RM shear walls with rectangular cross sections, no corresponding parameters are given for RM shear walls with boundary elements. As such, the parameters for RM shear walls with the same properties but with rectangular cross sections, given in Table 5.3, were used to predict the response of the individual shear walls in *Buildings III* and *IV*.

5.4.3 Assessment of Current Modeling Approaches

The experimental results of *Building III* and *Building IV* were used to assess the current RM backbone models in ASCE/SEI 41-13 (ASCE 2014) using both *Approaches 1* and *2*, as discussed earlier. The system-level response of *Building III* and *Building IV* was calculated through the superposition of the backbone model of the RM shear walls aligned along the main direction of loading at each displacement demand, where the resistance of the orthogonal walls was not considered because of their negligible strength in their out-of-plane direction (Heerema et. al 2015; Ashour and El-Dakhakhni 2016). The twist effects within both buildings were implemented in the superposition procedure using the displacement of each wall aligned along the main direction of loading obtained from the experimental results, and subsequently calculating the corresponding wall resistance using the individual wall backbone model. Finally, the lateral strengths of *Building III*, Q_{III}, and *Building IV*, Q_{IV}, was calculated at each displacement demand using Eq. (5.5) and Eq. (5.6), respectively.

$$Q_{III} = 2 \times Q_{W1_{III}} + Q_{W5_{III}} + Q_{W8_{III}} \tag{5.5}$$

$$Q_{IV} = 2 \times Q_{W1_{IV}} + Q_{W5_{IV}} + Q_{W8_{IV}} \tag{5.6}$$

Figures 5.6 (a and b) compare the experimental lateral load versus the top displacement at the building floor Center of Mass, C_M, to the model predictions for *Buildings III* and *IV*, respectively, using *Approaches 1* and *2* shown in Fig. 5.3. In addition, Table 5.4 summarizes the error of the model predictions for the same buildings. It should be noted that the drift at point D in *Approach 1* was assumed to be equal the average drift of points C and E, which resulted in a small slope, as suggested by ATC (2010), to the segment between points C and D in Fig. 5.3. As shown in Table 5.4, the model predicts the yield strength, Q_y, (i.e. at 0.25% drift) of *Buildings III* and *IV* to within a maximum error of 20% and 15%, respectively. In addition, the ultimate strength, Q_u, is captured closely, with Fig. 5.6 showing a maximum error of less than 20% and 11% relative to the experimental results of *Buildings III* and *IV*, respectively. These results confirm the importance of including the out-of-plane stiffness of the floor diaphragms, as neglecting this stiffness by assuming cantilever walls would have underestimated the strength of *Buildings III* and *IV* by approximately 50%. However, the model fails to predict the postyield branch of the experimental results of both buildings. As shown in Table 5.4, an error of up to 84% is reported for both the predicted postyield load-displacement relationships. This is mainly attributed to the very conservative values of the parameters "c", "d" and "e" in ASCE/SEI 41-13 (ASCE 2014) for RM shear walls. As such, the following section outlines the development of an analytical model that is capable of more accurately predicting the backbone of the load-displacement relationships of *Buildings III* and *IV* up to and following the ultimate strength point.

5.5 PROPOSED BACKBONE MODEL FOR RM BUILDINGS FOR ASCE/SEI 41

5.5.1 Model Development

The proposed backbone model defines the RM shear wall deformations in terms of elastic and plastic rotations using the generalized backbone curve relationship shown in Fig. 5.7. The elastic segment up to point B is defined by the elastic rotation, θ_y. The plastic rotation up to loss of the lateral load capacity at point C, θ_u, is represented by the parameter "a", while the parameter "b" represents the plastic rotation up to failure at point E, θ_r. The parameter "c" is also used to define the residual moment of point D, M_r. Although ASCE/SEI 41-13 (ASCE 2014) provides these parameters (i.e. "a", "b" and "c") for reinforced concrete (RC) shear walls, no corresponding values are currently given for RM shear walls. As such, the parameters specified for RC walls, given in Table 5.5, were used to predict the response of the individual shear walls in *Buildings III* and *IV*. This approach was considered acceptable during the model development because fully grouted RM structural wall construction is very similar to RC structural wall construction in terms of the material behavior and the analysis of displacements (Shedid et al. 2010; Banting and El-Dakhakhni 2014). In addition, several experimental studies have shown that high levels of ductility and small strength degradation, similar to those of RC shear walls, can be achieved with RM shear walls (Shing et al. 1990; Seible et al. 1993; Eikanas 2003; Shedid et al. 2008).

The ASCE/SEI 41-13 (ASCE 2014) also considers the enhanced lateral deformation capacity of RC walls with boundary elements by assigning higher distinctive values for the above parameters (i.e. “a”, “b” and “c”) to those walls than the corresponding values assigned to traditional shear walls with rectangular cross sections, so the same enhanced parameters, given in Table 5.5, were used for *Building IV*.

Figure 5.8 summarizes how to evaluate the key points to build the proposed model. Point A represents the unloaded condition, while point B defines the effective yield point through Q_y and Δ_y, which were given previously in Eqs. (5.1-a) and (5.3), respectively. Point C represents the ultimate strength point, where Q_u and Δ_u can be calculated from Eqs. (5.1-b) and (5.7-a), respectively.

$$\Delta_u = \Delta_y + a(h - l_p) \tag{5.7-a}$$

In Eq. (5.7-a) l_p is the plastic hinge length of the wall, assumed to be 50% of the wall flexural depth but less than the wall height and less than 50% of the wall length, according to ASCE/SEI 41-13 (ASCE 2014). Point D is a point defining the residual strength through Q_r and Δ_r, which can be determined from Eq. (5.1-c) and (5.7-b), respectively.

$$\Delta_r = \Delta_y + b(h - l_p) \tag{5.7-b}$$

At deformation levels beyond point D, the wall strength drops to zero, as represented by point E. The load-displacement relationships of the individual walls aligned along the main direction of loading of *Buildings III* and *IV*, shown in Figs. 5.9 (a and b), respectively, were predicted following Fig. 5.8. As can be seen in Figs. 5.9 (a and b), Δ_u and Δ_r of the walls in *Building IV* increase by an average of 35% and 30%, respectively, relative to their corresponding walls in *Building III*. This indicates the importance of including the confinement effect of the boundary elements when estimating the wall performance. In addition, Fig. 5.9 shows that the walls within each building do not all behave plastically simultaneously. Therefore, adding the strengths of all walls, by assuming that all walls simultaneously reach their ultimate capacities and have adequate ductility to sustain these capacities (ASCE 2014), would overestimate the overall building resistance. This confirms the importance of system-level studies used in this study to validate the developed model.

5.5.2 Comparison of Model Predictions with System-Level Experimental Responses

The system-level response of *Buildings III* and *IV* was calculated through the superposition of the backbone models of all RM shear walls aligned along the main direction of loading at each displacement demand level, considering building twist as discussed earlier. Figure 5.10(a) compares the prediction of the proposed model with the experimental results for *Building III*, and Table 5.6 summarizes the percentage error of the model predictions relative to the experimental data of the same building. As can be seen in Fig. 5.10(a) and Table 5.6, the lateral load of the building is predicted very closely for most lateral drift levels, with a maximum error in the lateral load prediction of less than 9%. In addition, the model captures the yield strength, Q_y, to within 14% error. The proposed model results are compared also with the experimental results of *Building IV* in Fig. 5.10 (b) and Table 5.6. Relative to the experimental results, the maximum error in the lateral load is less than 10%. In addition, the maximum difference between analytical and experimental yield strength, Q_y, is less than 13%.

These results confirm the effectiveness of the proposed parameters “a”, “b” and “c” for predicting the response of *Buildings III* and *IV*. Figs. 5.10 (a and b) show that the model is able to simulate most relevant characteristics of the response at all considered drift levels, including the post-ultimate range (i.e. strength degradation), whereas the current parameters assigned to RM shear walls in ASCE/SEI 41-13 (ASCE 2014) significantly underestimated the post-capacity, as previously shown in Fig. 5.6. This indicates that the parameters that ASCE/SEI 41-13 (ASCE 2014) assigns to RM shear walls with rectangular cross sections (“c”, “d” and “e”) may be unnecessarily conservative and may require revision. This conservatism was based on the limited number of experimental studies at the time when FEMA 356 (FEMA 2000), “*Prestandard and Commentary for the Seismic Rehabilitation of Buildings*”, was originally developed. In addition, distinctive corresponding values are needed for RM shear walls with boundary elements to consider the enhanced lateral deformation capacity achieved when they are adopted (Shedid et al. 2010; Banting and El-Dakhakhni 2012, 2014;

Cyrier 2012; El Ezz et al. 2015; Ezzeldin et al. 2016a; 2016c). These results suggest that the parameters currently given for RC in ASCE/SEI 41-13 (ASCE 2014) may be appropriate.

5.6 Proposed Hysteretic Model for RM Buildings for ASCE/SEI 41

5.6.1 Model Development

The Nonlinear Dynamic Procedure (NDP) evaluates the inelastic demands of a structure subjected to a suite of ground motion records based on nonlinear time history analysis (ASCE 2014; FEMA 2000). The NDP is considered a more desirable procedure compared to NSP because it represents the demands the structure would experience during a specific seismic event (ASCE 2014), including the shifts in inertial load patterns as structural softening occurs. However, the NDP requires hysteretic models that are able to capture not only the initial stiffness, peak load and strength deterioration, but also the stiffness degradation, hysteretic shape and pinching behavior.

In this respect, a simplified numerical model is developed in this chapter using *OpenSees* (McKenna et al. 2000) and validated against the experimental results of *Buildings III* and *IV*. The developed numerical model adopts a concentrated plasticity approach, where elastic beam-column elements are used to model the walls of both buildings, with the wall inelastic behavior accounted for through a zero-length inelastic rotational spring at the base of each wall, as shown in Fig. 5.11(a). These springs follow a bilinear hysteretic response based on the modified Ibarra-Medina-Krawinkler deterioration model with pinching hysteretic response (Ibarra et al. 2005, ModIMKPinching material in *OpenSees*). The model is represented by a moment-rotation relationship, as shown in Fig. 5.11(b), that depends on the yield moment, M_y, the ultimate moment, M_u, the residual moment, M_r, the rotational stiffness, K_θ, the pre-ultimate plastic rotation, θ_p, the post-ultimate plastic rotation, θ_{pc}, and other parameters that define strength deterioration and pinching behavior. The parameters M_y, M_u and M_r were defined earlier, while K_θ, θ_p and θ_{pc} can be calculated from Eqs. (5.8), (5.9-a) and (5.9-b), respectively, in terms of the previously defined parameters I_e, h, θ_y, θ_u and θ_r.

$$K_\theta = \frac{(n+1)6EI_e}{h} \tag{5.8}$$

$$\theta_p = \theta_u - \theta_y \tag{5.9-a}$$

$$\theta_{pc} = \theta_r - \theta_u \tag{5.9-b}$$

In Eq. (5.8) a stiffness modifier, n, of value 10 is used in calculating the rotational stiffness, K_θ, since the wall is modeled as a rotational spring connected in series with elastic beam-column element, as shown in Fig. 5.11(b). Subsequently, the stiffness of these components is modified so that their equivalent stiffness, K_w, is equal to the stiffness of the actual wall. For this reason and also to avoid any numerical problems, the rotational spring stiffness,

K_θ, and the elastic element stiffness, K_e, are multiplied by modification factors of $(n+1)$ and $(n+1/n)$, respectively, as suggested by Ibarra and Krawinkler (2005), and wall equivalent stiffness, K_w, is then calculated.

$$K_w = \frac{K_\theta K_e}{K_\theta + K_e} \tag{5.10}$$

The strength deterioration and pinching behavior parameters were defined as suggested by Lignos and Krawinkler (2012) based on database of 200 RC components with different configurations. The model accounts for the boundary conditions through the calculation of K_θ, where the RM shear walls are considered fixed at the foundation and partially fixed at the roof levels (from Eq. (5.8)). Therefore, the RC floor slabs of *Buildings III* and *IV* were modelled considering the diaphragm possessing no out-of-plane stiffness, while still being stiff in the in-plane direction.

5.6.2 Model Validation

Figure 5.12(a) compares the results of the numerical model with the corresponding experimental results for *Building III* tested by Ashour et al. (2016). The figure shows that the model is capable of simulating most relevant characteristics of the cyclic response at different drift levels. The drift ranges in Fig. 5.12 cover the entire load-displacement curve up to degradation to 80% of the ultimate strength. The lateral capacity of the building is predicted closely for most of the lateral drift levels, with a maximum deviation in the lateral load prediction of less than 16%. In addition, the increase of energy dissipation with loading is represented well by the hysteretic model, with a maximum deviation of 15% compared to the experimental results.

To verify the effectiveness of the developed model for buildings with boundary elements, the model results are compared with the experimental results from *Building IV* (Ezzeldin et al. 2016c) in Fig. 5.12(b) and the individual experimental and numerical hysteresis loops for the same building, using the first cycle at each of the second floor drift levels is shown in Fig. 5.13. Relative to the experimental results, the maximum error in the lateral load prediction is less than 10%. In addition, the model captures the energy dissipation with a maximum error of approximately 9%. Overall, the comparison between the experimental and numerical results shows that the proposed model, based on previous results for RC, is capable of capturing the hysteretic response of RM shear wall buildings both with and without boundary elements.

5.7 CONCLUSIONS

The Nonlinear Static Procedure (NSP) and the Nonlinear Dynamic Procedure (NDP), specified in ASCE/SEI 41-13 (ASCE 2014), require nonlinear structural response models that are capable of predicting the inelastic behavior of buildings at different performance levels. This chapter demonstrated that existing recommendations for reinforced masonry (RM) may not adequately predict this behavior, and proposed alternate new backbone and hysteretic models for simulating the nonlinear response of shear wall buildings with different configurations. Subsequently, these models were validated against the experimental results of *Buildings III* and *IV* reported by Ashour et al. (2016) and Ezzeldin et al. (2016c), respectively. The backbone model accurately captured the complete load-displacement relationships of both buildings, with maximum errors of 14%. In addition, a hysteretic model was developed using *OpenSees* to simulate the hysteretic response of RM shear wall buildings. The inelastic behavior of each wall in that model is represented by a zero-length inelastic rotational spring at the base of the wall. Finally, the results showed that the developed model satisfies the ASCE/SEI 41-13 (ASCE 2014) requirements in terms of simulating the initial stiffness, peak load, stiffness degradation, strength deterioration, hysteretic shape and pinching behavior at different drift levels.

In general, the results confirmed the importance of including out-of-plane stiffness of the floor diaphragms to estimate the overall building response. In addition, the results showed that the current parameters assigned to RM shear walls in ASCE/SEI 41-13 need to be revised, because the models developed based on those parameters failed to capture the postyield branch of the experimental results. Moreover, ASCE/SEI 41-13 (ASCE 2014) provides parameters only for RM shear walls with rectangular cross sections. This chapter showed that distinctive corresponding values should be provided for RM shear walls with boundary elements, so as to consider the enhanced lateral deformation capacity achieved when such systems are adopted. These values may be based on what is currently specified for reinforced concrete (RC) shear walls.

The analyses in this chapter were limited to two two-story RM shear wall buildings, one with walls having rectangular cross sections and the other with walls with boundary elements. More RM buildings with different numbers of stories and configurations should be studied to further validate the developed models presented in this chapter, thus facilitating the development of prescriptive design requirements for such SFRS.

5.8 ACKNOWLEDGMENTS

The financial support for this project was provided through the Natural Sciences and Engineering Research Council of Canada and the Canada Masonry Design Centre (CMDC). Support was also provided by the McMaster University Centre for Effective Design of Structures, funded through the Ontario Research and Development Challenge Fund of the Ministry of Research and Innovation.

5.9 NOTATIONS

The following symbols are used in this chapter:

A_e = Effective cross section area;
A_g = Gross cross section area;
a = Plastic rotation up to loss of the wall lateral load capacity;
b = Plastic rotation up to wall failure;
c = Residual moment/strength ratio;
C_M = Building floor center of mass;
C_R = Building center of rigidity;
d = Parameter to represent the ultimate drift;
E_m = Masonry modulus of elasticity;
e = Parameter to represent the maximum drift;
f'_m = Masonry compressive strength;
f_{yv} = Vertical reinforcement yield strength;
G_m = Masonry shear modulus;
h = Wall height;
I_e = Effective moment of inertia;
I_g = Gross moment of inertia;
K_y = Elastic stiffness;
K_e = Elastic element stiffness;
K_w = Wall equivalent stiffness;
K_θ = Spring rotational stiffness;
l_p = Plastic hinge length of the wall;
M_r = Residual moment;
M_{top} = Top coupling moment;
M_u = Ultimate moment;
M_y = Yield moment;
P = Wall axial load;
P_o = Orthogonal walls compression force;
Q_r = Residual strength;
Q_u = Ultimate strength;
Q_{III} = Lateral strength of *Building III*;
Q_{IV} = Lateral strength of *Building IV*;
Q_y = Yield strength;
T_o = Orthogonal walls tension force;
Δ_y = Yield drift ratio;
Δ_u = Ultimate drift ratio;
Δ_r = Maximum drift ratio;
θ_p = Pre-ultimate rotation;
θ_{pc} = Post-ultimate rotation;
θ_r = Maximum rotation capacity;
θ_u = Ultimate rotation;

θ_y = Yield rotation;
α = Reduction factor.

5.10 REFERENCES

Abdellatef, M. (2011). “The development of a simplified modelling technique for the finite element analysis of reinforced masonry shear walls.” M.Sc. thesis, Dept. of Civil and Environmental Engineering, Washington State Univ., Pullman, WA.

Andreini, M., De Falco, A., Giresini, L., and Sassu, M. (2014). “Mechanical characterization of masonry walls with chaotic texture: procedures and results of in-situ tests.” *International Journal of Architectural Heritage*, 8(3), 376-407.

Ashour, A., and El-Dakhakhni, W. (2016). “Influence of floor diaphragm–wall coupling on the system-level seismic performance of an asymmetrical reinforced concrete block building.” *J. Struct. Eng*., 04016071.

Ashour, A., El-Dakhakhni, W., and Shedid, M. (2016). “Experimental evaluation of the system-level seismic performance and robustness of an asymmetrical reinforced concrete block building.” *J. Struct. Eng*., 04016072.

ASCE/SEI (Structural Engineering Institute). (2014). “Seismic Evaluation and Retrofit of Existing Buildings.” *ASCE/SEI 41-13*, Reston, VA.

ATC (Applied Technology Council) (2010). “Modeling and acceptance criteria for seismic design and analysis of tall buildings.” *PEER/ATC Report No. 72-1*, Redwood City.

Banting, B. and El-Dakhakhni, W. (2012). ”Force-and displacement-based seismic performance parameters for reinforced masonry structural walls with boundary elements." *J. Struct. Eng.*, 10.1061/(ASCE)ST.1943-541X.0000572, 1477–1491.

Banting, B. and El-Dakhakhni, W. (2014). "Seismic performance quantification of reinforced masonry structural walls with boundary elements." *J. Struct. Eng.*, 10.1061/(ASCE) ST.1943-541X.0000895, 04014001.

Canadian Standards Association (CSA). (2014) "Design of masonry structures." CSA S304-14, Mississauga, Canada.

Cyrier, W. B. (2012). "Performance of concrete masonry shear walls with integral confined concrete boundary elements" Ph.D. dissertation, Washington State Univ.

Dolšek, M., and Fajfar, P. (2008). "The effect of masonry infills on the seismic response of a four-storey reinforced concrete frame—a deterministic assessment." *Engineering Structures*, 30(7), 1991-2001.

Dymiotis, C., Kappos, A. J., and Chryssanthopoulos, M. K. (2001). "Seismic reliability of masonry-infilled RC frames." *J. Struct. Eng.*, 127(3), 296-305.

El Ezz, A. A., Seif Eldin, H. M., and Galal, K. (2015). "Influence of confinement reinforcement on the compression stress–strain of grouted reinforced concrete block masonry boundary elements." *Structures*, 2, 32–43.

Eikanas, I. (2003). "Behaviour of concrete masonry shear walls with varying aspect ratio and flexural reinforcement." MS thesis, Washington State Univ.

Ezzeldin, M., Wiebe, L., and El-Dakhakhni, W. (2016a). "Seismic collapse risk assessment of reinforced masonry walls with boundary elements using the FEMA P695 methodology." *J. Struct. Eng*., 142(11), 04016108.

Ezzeldin, M., Wiebe, L., and El-Dakhakhni, W. (2016b). "Numerical modelling of reinforced concrete block structural wall buildings under seismic loading." *The Annual conf. of Canadian Society of Civil Engineering*, London, Canada.

Ezzeldin, M., El-Dakhakhni, W., and Wiebe, L. (2016c). "Experimental Assessment of the System-Level Seismic Performance of an Asymmetrical Reinforced Concrete Block Wall Building with Boundary Elements." *J. Struct. Eng*., 10.1061/(ASCE)ST.1943-541X.0001790.

FEMA. (2005). "Improvement of nonlinear static seismic analysis procedures." *FEMA 440*, Washington, DC.

FEMA. (2009). "Quantification of building seismic performance factors." *FEMA P695*, Washington, DC.

FEMA. (2000). "Prestandard and commentary for the seismic rehabilitation of buildings." *FEMA 356*, Washington, DC.

FEMA. (2012). "Seismic performance assessment of buildings." *FEMA P58-1*, Washington, DC.

Giambanco, G., Rizzo, S., and Spallino, R. (2001). "Numerical analysis of masonry structures via interface models." *Computer methods in applied mechanics and engineering*, 190(49), 6493-6511.

Guinea, G. V., Hussein, G., Elices, M., and Planas, J. (2000). "Micromechanical modeling of brick-masonry fracture." *Cement and concrete research*, 30(5), 731-737.

Heerema, P., Shedid, M., Konstantinidis, D., and El-Dakhakhni, W. (2015). "System-level seismic performance assessment of an asymmetrical reinforced concrete block shear wall building." *J. Struct. Eng.*, 141(12), 04015047.

Ibarra, L. F., Medina, R. A., and Krawinkler, H. (2005). "Hysteretic models that incorporate strength and stiffness deterioration." *Earthquake engineering and structural dynamics*, 34(12), 1489-1511.

Ibarra, L. F., and Krawinkler, H. (2005). "Global collapse of frame structures under seismic excitations." Berkeley, CA: *Pacific Earthquake Engineering Research Center*.

Karapitta, L., Mouzakis, H., and Carydis, P. (2011). "Explicit finite-element analysis for the in-plane cyclic behavior of unreinforced masonry structures." *Earthquake Engineering and Structural Dynamics*, 40(2), 175-193.

Lignos, D. G., and Krawinkler, H. (2012). "Development and utilization of structural component databases for performance-based earthquake engineering." *J. Struct. Eng.*, 139(8), 1382-1394.

Lourenço, P. B., and Rots, J. G. (1997). "Multisurface interface model for analysis of masonry structures." *Journal of engineering mechanics*, 123(7), 660-668.

Marques, R., and Lourenço, P. B. (2014). "Unreinforced and confined masonry buildings in seismic regions: Validation of macro-element models and cost analysis." *Engineering Structures*, 64, 52-67.

Masonry Standards Joint Committee. (MSJC). (2013). "Building code requirements and specifications for masonry structures." *TMS 402-13/ ACI 530-13/ASCE 5-13*, the Masonry Society, American Society of Civil Engineers, Boulder, New York/American Concrete Institute, and Detroit, USA.

McKenna, F., Fenves, GL., and Scott, MH. (2000). "Open System for Earthquake Engineering Simulation." University of California, Berkeley, CA, 2000. Available from: *http://opensees.berkeley.edu*, Version 2.4.3.

Mojsilovic, N., and Marti, P. (1997). "Strength of masonry subjected to combined actions." *ACI structural journal*, 94(6), 633-642.

Paulay, T. (1997). "Seismic torsional effects on ductile structural wall systems." *J. Earthquake Eng*., 1(4), 721–745.

Paulay, T., and Priestly, M. (1992). *Seismic design of reinforced concrete and masonry buildings*, Wiley, New York.

Priestley, N., Calvi, G., and Kowalsky, M. (2007). *Displacement-based seismic design of structures*, IUSS Press, Pavia, Italy.

Schodek, D. L., and Bechthold, M. (2001). *Structures*, 6th edition, Prentice Hall.

Seible, F., Kürkchübasche, A. G., and Kingsley, G. R. (1993). "Three-dimensional analysis model for complete masonry buildings." *In Structural*

Engineering in Natural Hazards Mitigation, ASCE, 1185-1190.

Shedid, M. T., Drysdale, R. G., and El-Dakhakhni, W. W. (2008). “Behavior of fully grouted reinforced concrete masonry shear walls failing in flexure: Experimental results.” *J. Struct. Eng*., 134(11), 1754-1767.

Shedid, M. T., El-Dakhakhni, W. W. and Drysdale, R. G. (2010). “Alternative strategies to enhance the seismic performance of reinforced concrete-block shear wall systems.” *J. Struct. Eng*., 136(6), 676-689.

Shing, P. B., Schuller, M., and Hoskere, V. S. (1990). “In-plane resistance of reinforced masonry shear walls.” *J. Struct. Eng*., 116(3), 619-640.

Siyam, M., El-Dakhakhni, W., Shedid, M., and Drysdale, R. (2015). "Seismic response evaluation of ductile reinforced concrete block structural walls. I: experimental results and force-based design parameters." *J. Perform. Constr. Facil.* , 10.1061/(ASCE)CF.1943-5509.0000794, 04015066.

Stavridis, A., and Shing, P. B. (2010). “Finite-element modeling of nonlinear behavior of masonry-infilled RC frames.” *J. Struct. Eng*., 136(3), 285-296.

Stavridis, A., Ahmadi, F., Mavros, M., Koutromanos, I., Hernández, J., Rodríguez, J., Shing, P.B. and Klingner, R.E. (2011). “Shake-table tests of a 3-story, full-scale masonry wall system.” *Proc., ACI Masonry Seminar*, Dallas.

Table 5.1 Summary of Material Properties within *Building III* and *Building IV*.

Walls properties		*Building III*	*Building IV*
Masonry	f'_m (MPa)	19	17
	E_m (MPa)	12,600	12,100
	G_m (MPa)	5,050	4,850
Rebar	f_{yv} (MPa)	500	457
	E_s (MPa)	200,000	200,000

Table 5.2 Summary of Bending Moments along the Wall Height Within *Building III* and *Building IV*.

Building	Wall	Bending Moment Along the Wall Height (kN.m)				
		At Yield (Point B)		At Ultimate (Point C)		At Strength Degradation (Point E)
		M_y	M_{top}	M_u	M_{top}	cM_u
Building III	$W1_{III}$ and $W2_{III}$	21	8	31	8	19
	$W5_{III}$	122	128	184	128	110
	$W8_{III}$	189	224	263	224	158
Building IV	$W1_{IV}$ and $W2_{IV}$	23	12	29	12	22
	$W5_{IV}$	153	150	178	150	134
	$W8_{IV}$	193	150	239	150	179

Table 5.3 Summary of Modelling Parameters Assigned to RM Walls Within *Building III* and *Building IV* based on ASCE (2014).

Wall	Modelling parameters		
	c (%)	d (% drift)	e (% drift)
$W1_{III/IV}$ & $W2_{III/IV}$	67	0.66	1.32
$W5_{III/IV}$	67	0.40	0.80
$W8_{III/IV}$	70	0.30	0.60

Table 5.4 Error for the Predicted Values Using the Current Backbone Models in ASCE/SEI 41-13 versus the Experimental Data at Each Drift Level

		Error													
Building	Approach	Negative loading direction (Drift)							Positive loading direction (Drift)						
		-1.80%	-1.50%	-1.20%	-0.90%	-0.60%	-0.40%	-0.25%	0.25%	0.40%	0.60%	0.90%	1.20%	1.50%	1.80%
Building III[a]	1	N.A.	—	—	-83%	-64%	-28%	20%	8%	-21%	-47%	-83%	-82%	—	N.A.
	2	N.A.	—	—	-71%	-55%	-10%	18%	20%	-2%	-45%	-74%	—	—	N.A.
Building IV[b]	1	—	—	—	-83%	-63%	-15%	15%	15%	3%	-51%	-84%	—	—	—
	2	—	—	—	-75%	-30%	-3%	15%	15%	5%	-21%	-78%	—	—	—

Notes: N.A. = Experimental data not available

Entries with — denote model predicting zero strength

[a] Based on data from Ashour et al. (2016)

[b] Based on data from Ezzeldin et al. (2016c)

Table 5.5. Summary of Modelling Parameters Assigned to the Proposed Model of RM Walls within *Building III* and *Building IV* based on ASCE (2014).

Building	Modelling parameters		
	a (rad)	b (rad)	c (%)
Building III	0.006	0.015	60
Building IV	0.010	0.020	75

Table 5.6. Error for the Predicted Values using the Proposed Backbone Model in ASCE/SEI-41 versus the Experimental Data at Each Drift Level

	Error													
Building	Negative loading direction (Drift)							Positive loading direction (Drift)						
	-1.80%	-1.50%	-1.20%	-0.90%	-0.60%	-0.40%	-0.25%	0.25%	0.40%	0.60%	0.90%	1.20%	1.50%	1.80%
Building III[a]	N.A.	-9%	-2%	1%	1%	-1%	-14%	3%	1%	-1%	-5%	-9%	-5%	N.A.
Building IV[b]	-10%	-2%	10%	3%	4%	3%	13%	13%	2%	1%	2%	9%	5%	-8%

Note: N.A. = Experimental data not available

[a] Based on data from Ashour et al. (2016)

[b] Based on data from Ezzeldin et al. (2016c)

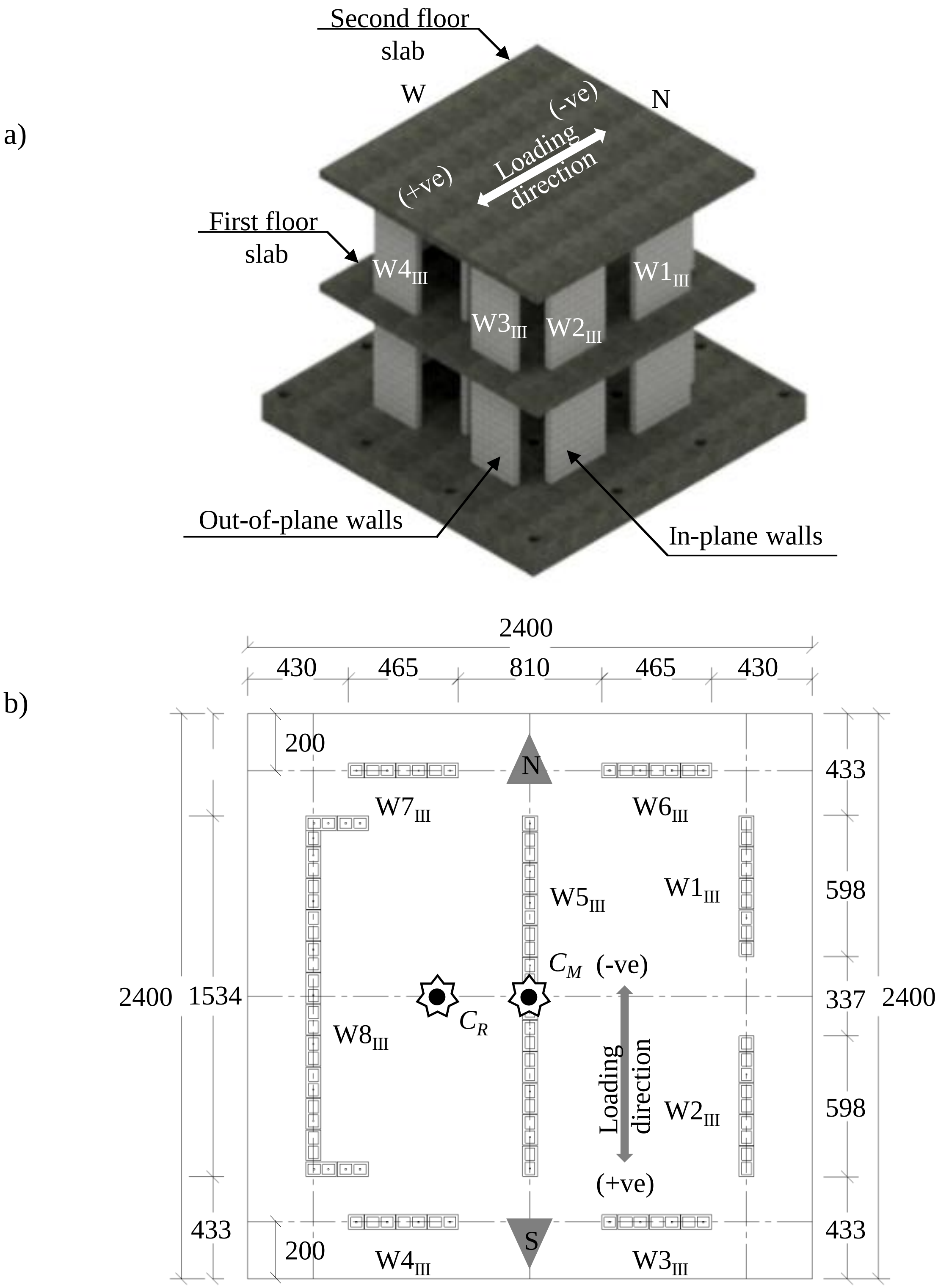

Fig. 5.1: *Building III* configuration (data from Ashour et al. 2016);
a) Isometric view from South-East direction; b) Typical plan, all dimensions are in (mm).

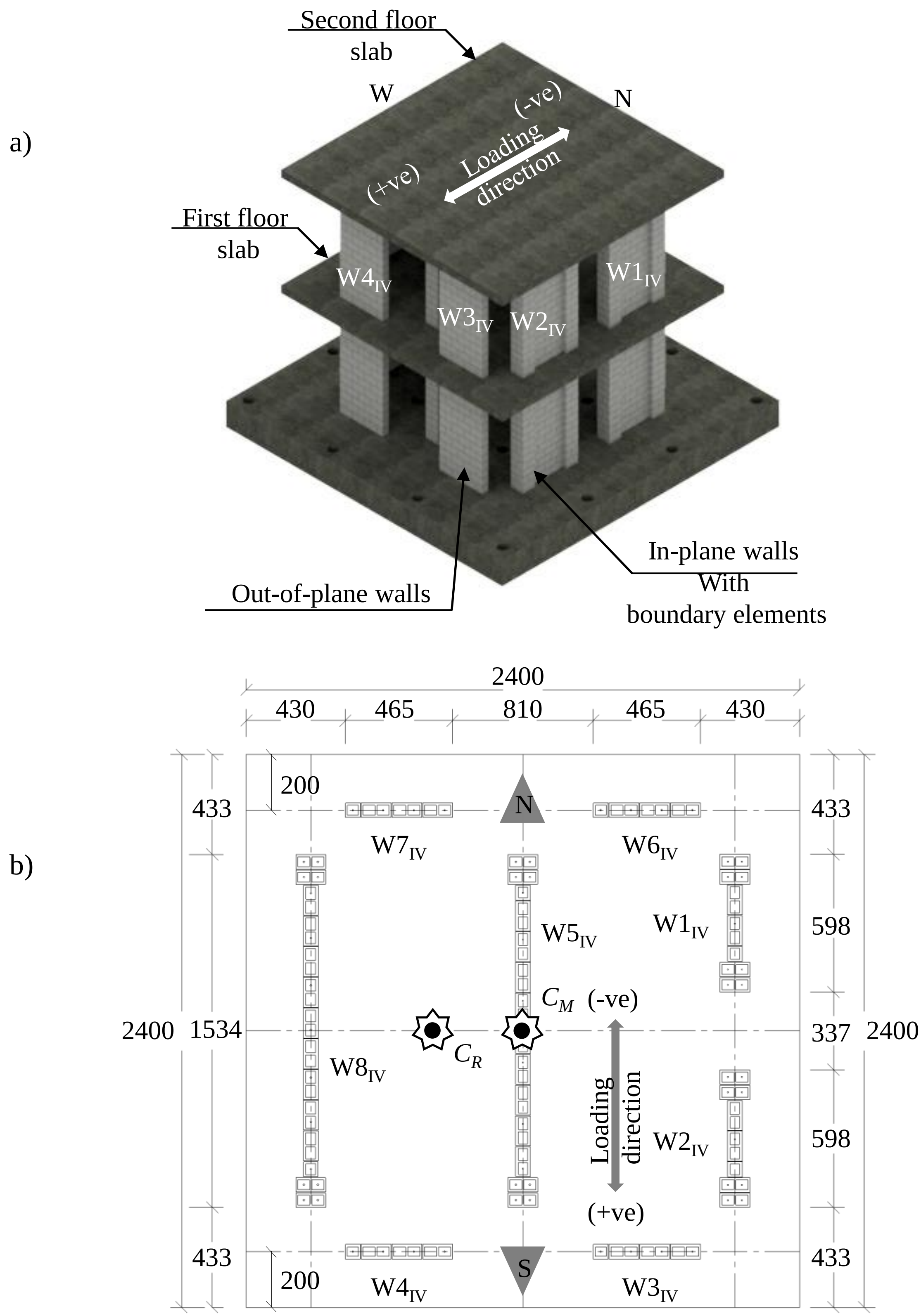

Fig. 5.2: *Building IV* configuration (data from Ezzeldin et al. 2016c);
a) Isometric view from South-East direction; b) Typical plan, all dimensions are in (mm).

c)

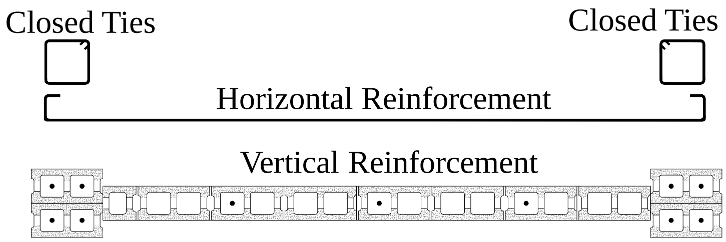

Fig. 5.2 (cont.): *Building IV* configuration (data from Ezzeldin et al. 2016c);
c) In-plane walls with boundary elements configuration.

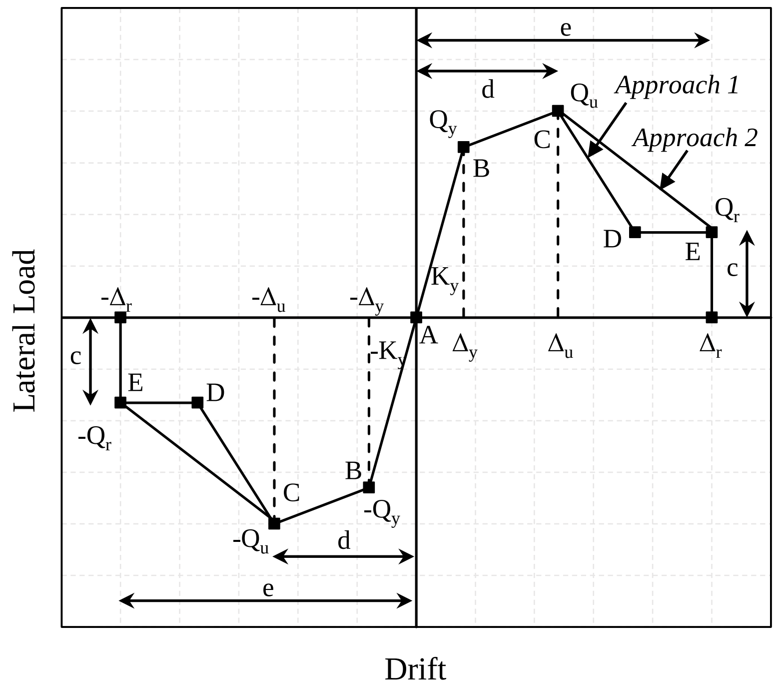

Fig. 5.3: Simplified load-drift relationship of reinforced masonry shear walls in ASCE/SEI 41-13 (ASCE 2014).

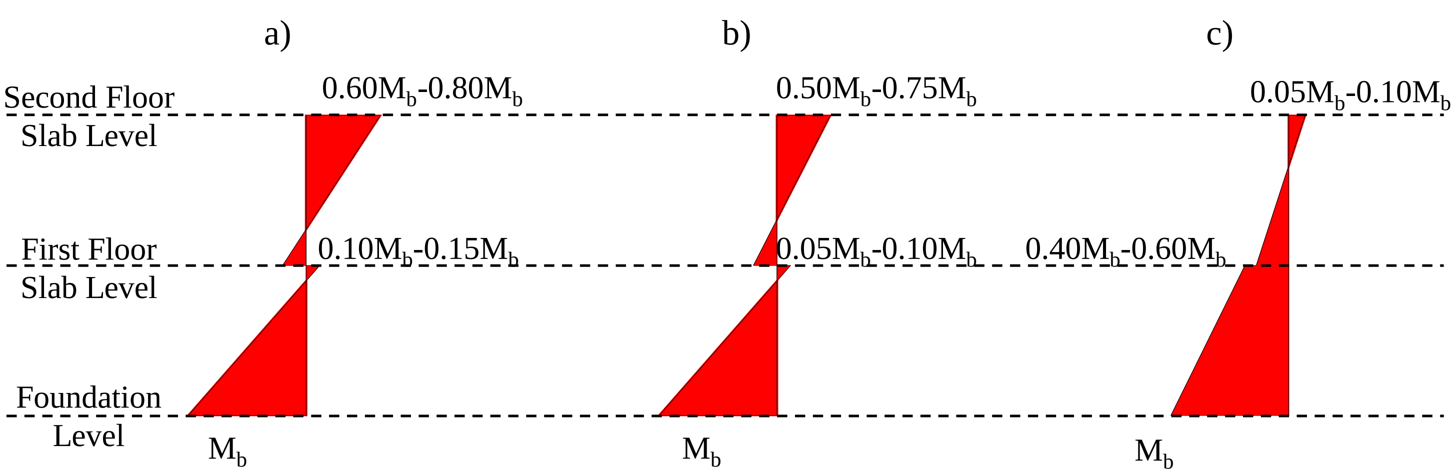

Fig. 5.4: Bending moments along the wall height of *Building IV* based on the numerical model developed by Ezzeldin et al. (2016b);
a) At drift = 0.25 %; b) At drift = 0.90 %; c) At drift = 2.00 %.

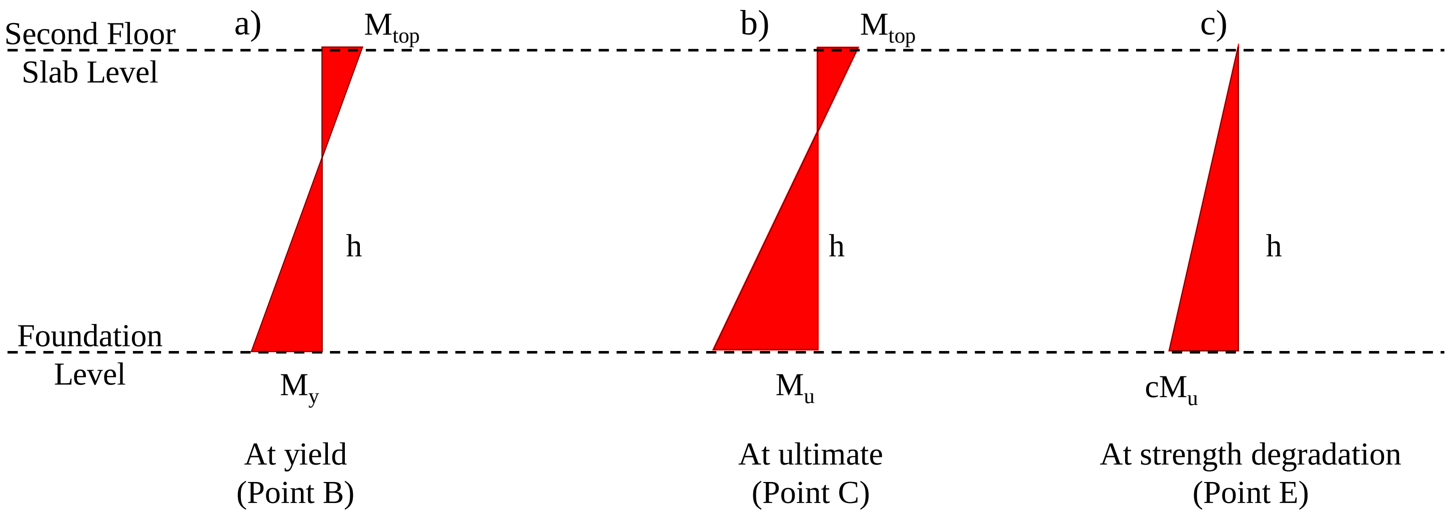

Fig. 5.5: Assumed bending moments along the wall height;
a) Yield point; b) Ultimate point; c) Strength degradation point.

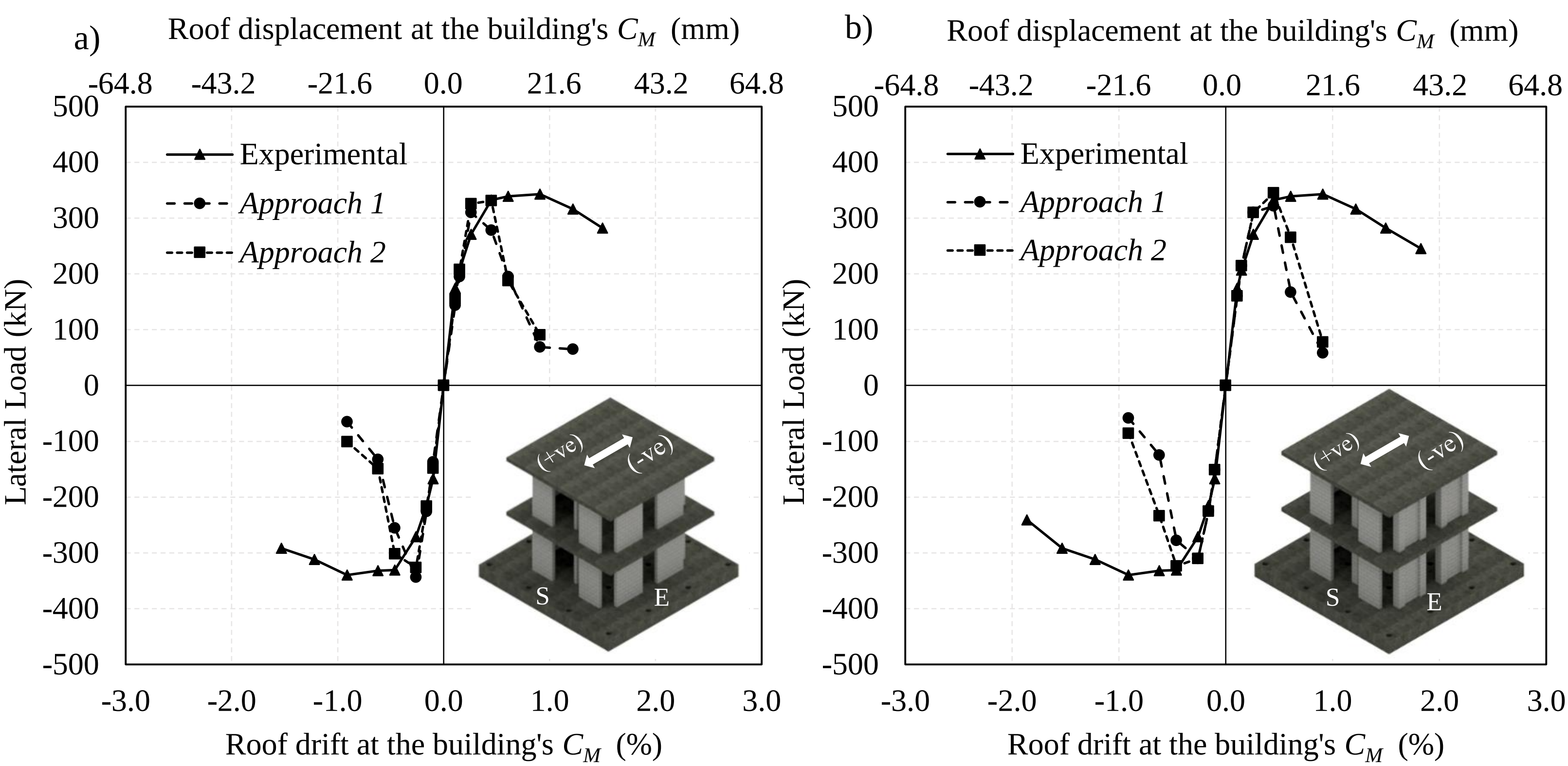

Fig. 5.6: Experimental and analytical envelopes based on ASCE/SEI 41-13 (ASCE 2014)
using *Approach 1 and Approach 2*;
a) *Building III* (data from Ashour et al. 2016); b) *Building IV* (data from Ezzeldin et al. 2016c).

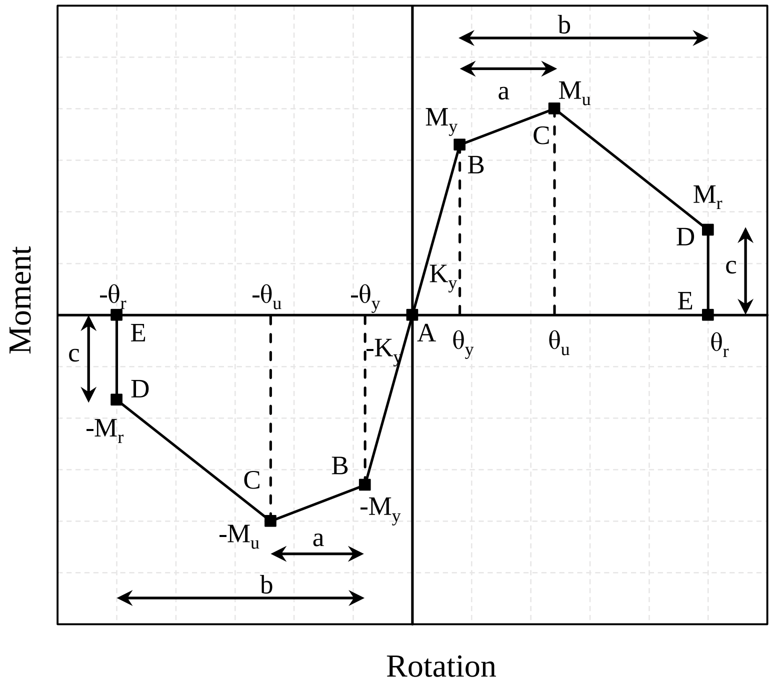

Fig. 5.7: Proposed simplified moment-rotation relationship for reinforced masonry shear walls without and with boundary elements.

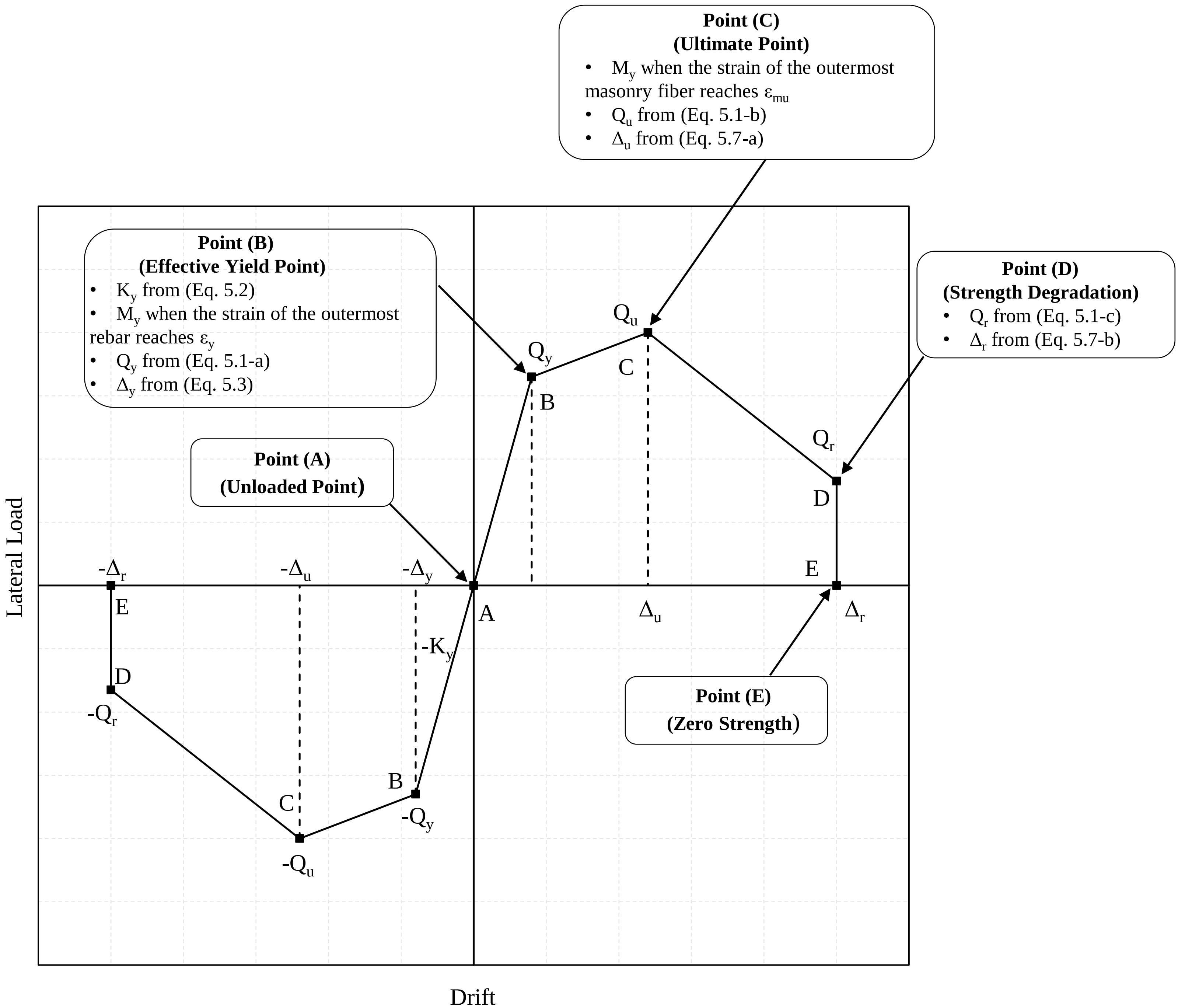

Fig. 5.8: Proposed simplified load-drift relationship for reinforced masonry shear walls without and with boundary elements.

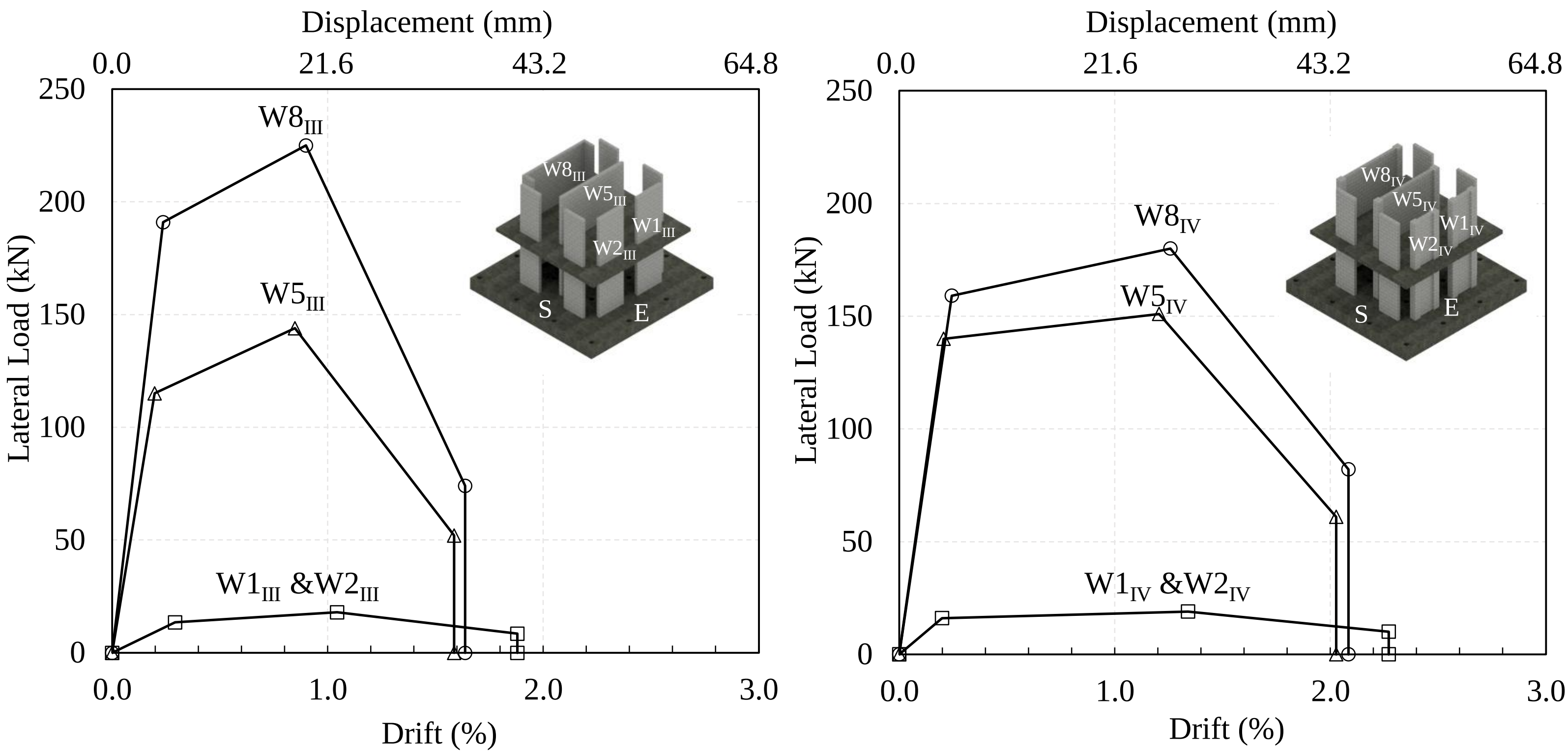

Fig. 5.9: Load-drift relationship of walls aligned along the loading direction;
a) *Building III* (data from Ashour et al. 2016); b) *Building IV* (data from Ezzeldin et al. 2016c).

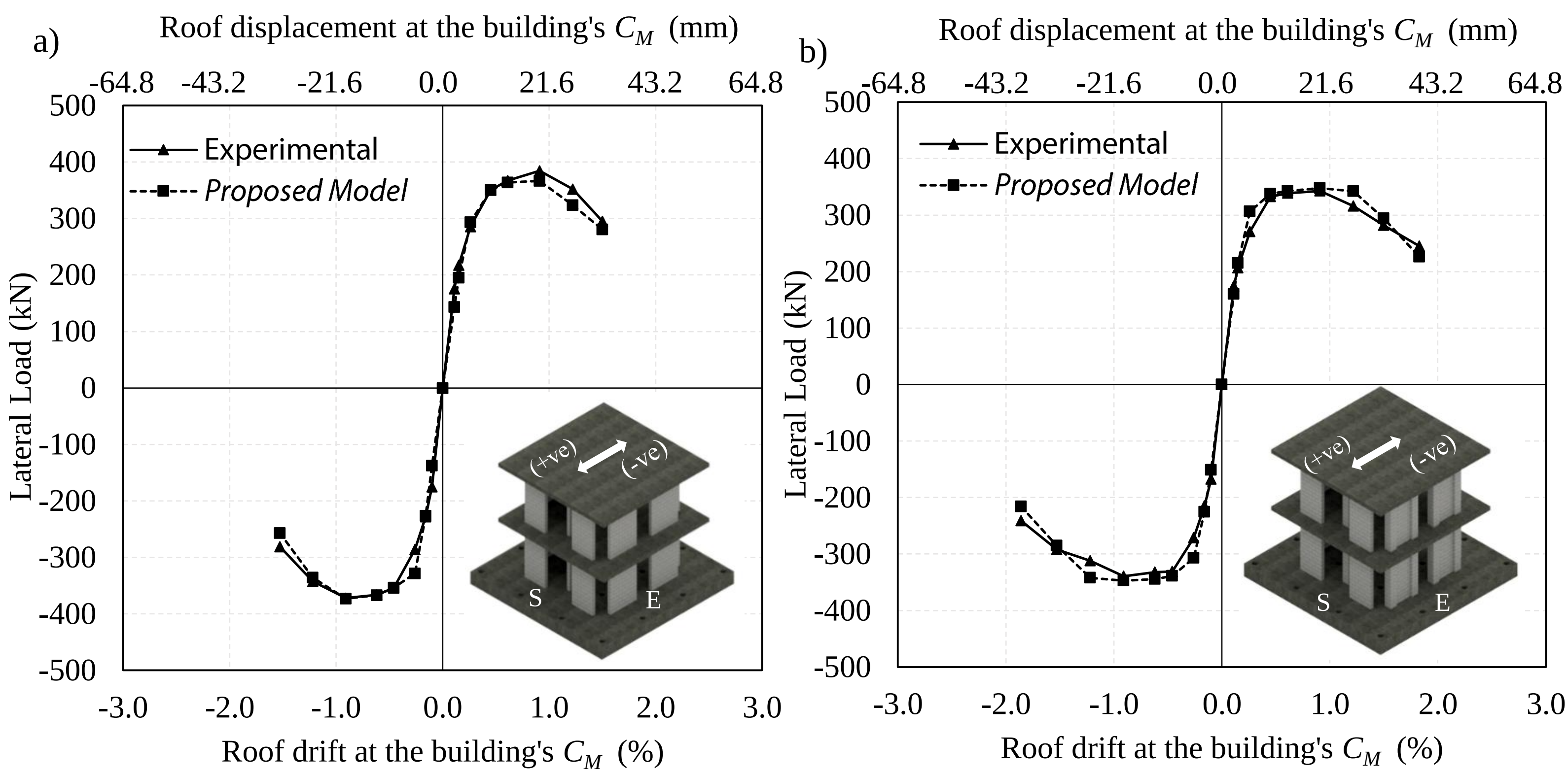

Fig. 5.10: Experimental and analytical envelopes based on the proposed modelling approach;
a) *Building III* (data from Ashour et al. 2016); b) *Building IV* (data from Ezzeldin et al. 2016c).

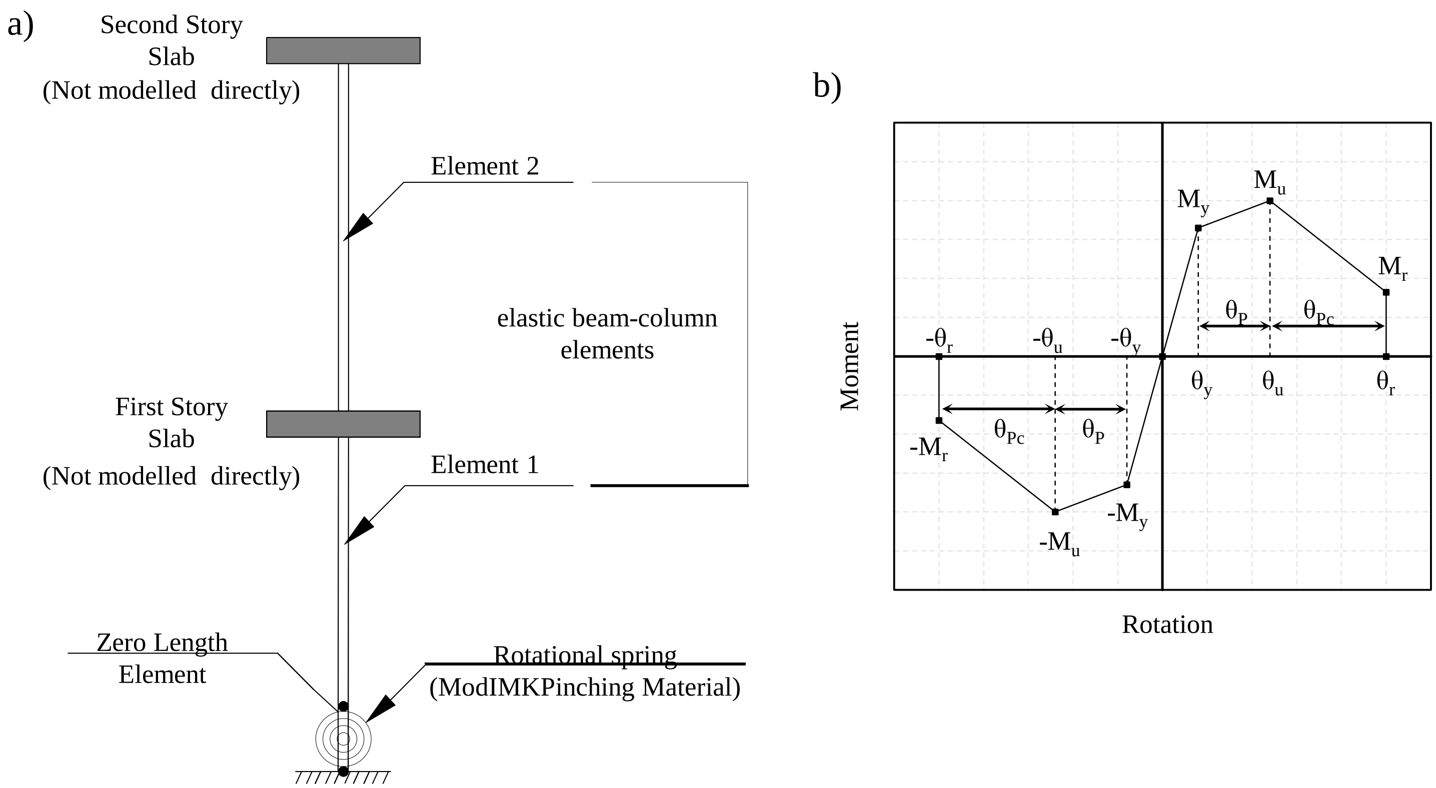

Fig. 5.11: Schematic diagram of the model.

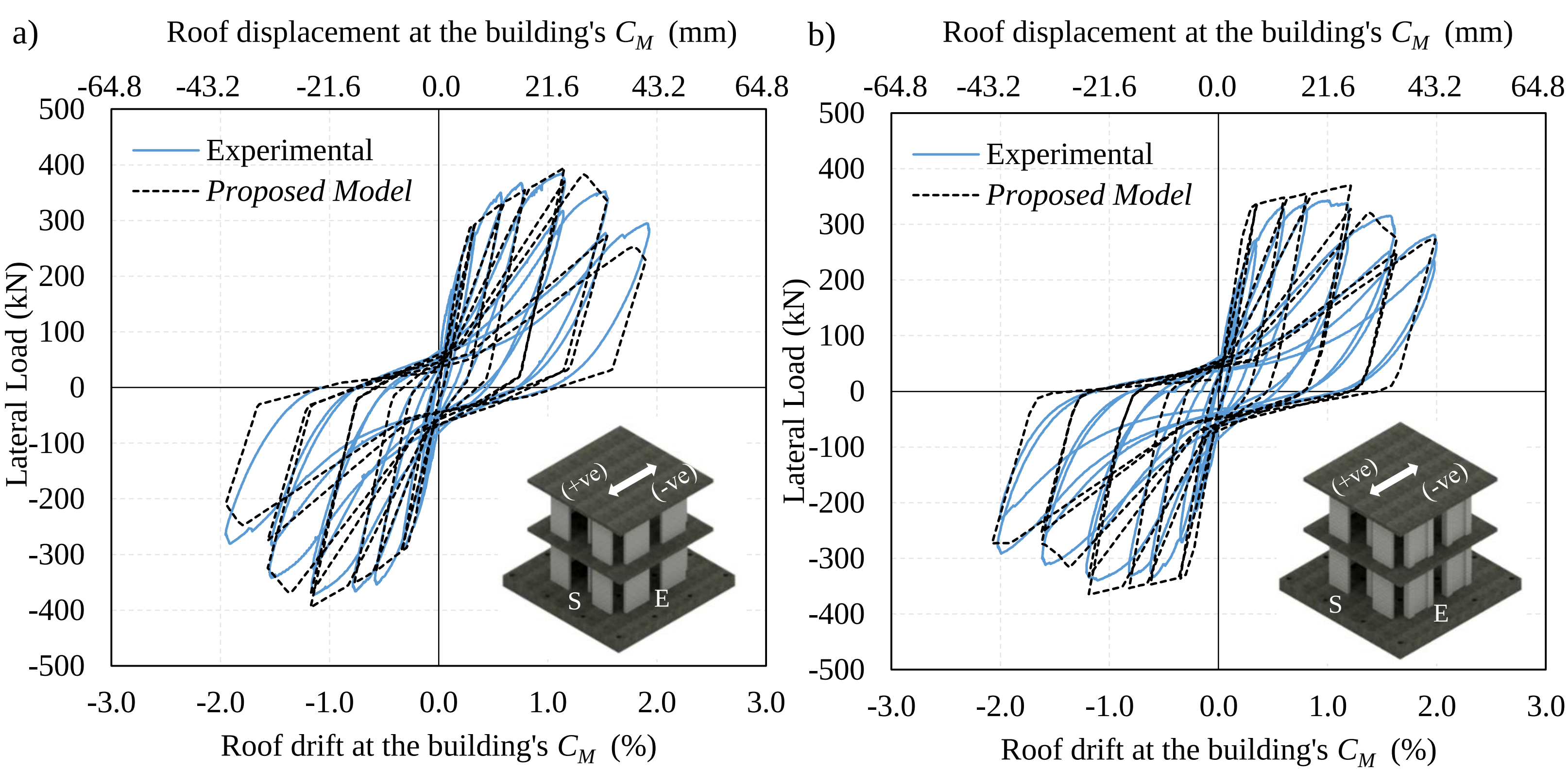

Fig. 5.12: Experimental and numerical hysteresis loops;
a) *Building III* (data from Ashour et al. 2016); b) *Building IV* (data from Ezzeldin et al. 2016c).

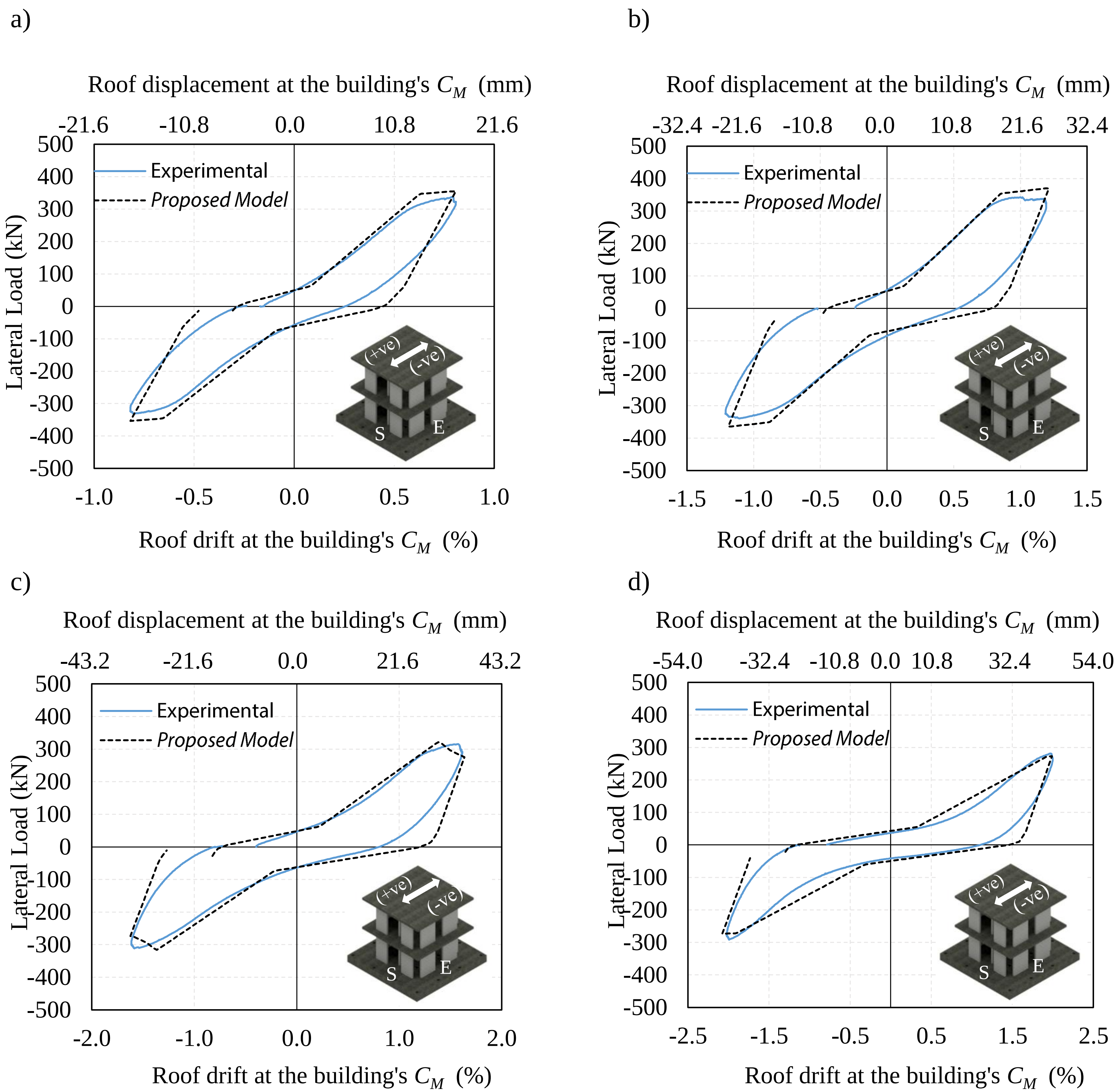

Fig. 5.13: Detailed experimental and numerical hysteresis loops of *Building IV* (data from Ezzeldin et al. 2016c); a) At drift = 0.90 %; b) At drift = 1.20 %; c) At drift = 1.50 %; d) At drift = 2.00%.

CHAPTER 6
SUMMARY, CONCLUSIONS AND RECOMMENDATIONS

6.1 SUMMARY

This dissertation focuses on investigating the system-level seismic response of RM shear wall buildings with boundary elements. The main objective of this dissertation is to facilitate the adoption of this system as a new and more resilient SFRS in future editions of the CSA S304 and TMS 402. In addition to its own focus and objectives, this dissertation also represents the results of the fourth phase (*Phase IV)* of a multi-phase research program at McMaster University that investigates the discrepancies between the seismic responses of RM shear walls at the component- and system-levels. In this respect, a seismic collapse risk simulation is performed first to evaluate the seismic collapse margin ratios of RM walls with boundary elements at the component-level. Following this component-level simulation, the system-level experimental results are presented for a scaled RM shear wall two-story building with boundary elements, *Building IV*, tested under quasi-static displacement-controlled cyclic loading representing the seismic loading. Based on the experimental results, an innovative risk assessment methodology is proposed to generate more realistic system-level fragility curves, in an effort to quantify the overall building system risk under different levels of seismic hazard. Finally, simplified backbone and hysteretic models are developed to simulate the nonlinear response of RM shear wall buildings with different configurations. These models can be used to perform the NSP and NDP specified in North American codes and standards (e.g. ASCE/SEI 41-13).

6.2 CONCLUSIONS

The numerical, analytical and experimental results presented in this dissertation highlight the ability of boundary elements to enhance the seismic response of RM shear walls at both the component- and system-levels. The dissertation contributes to the knowledgebase pertaining to this new building system and presents the following overarching conclusions based on the research results reported in the preceding chapters.

Within the context of the current North American codes and standards, there are no clear and unique design provisions regarding RM wall components (i.e. individual walls) or systems (i.e. complete buildings) with boundary elements. However, the component- and system-level results in this study demonstrated the influence of boundary elements in enhancing the displacement and ductility capacities of such walls when compared to their counterparts with rectangular cross sections. This behavior also increases the energy dissipation, with an overall enhancement of performance of the RM system under extreme events. These findings also support the notion that unique seismic modification factors and reinforcement detailing requirements should be provided for RM shear walls with boundary elements within the next editions of the CSA S304 and the TMS 402 masonry design codes/standards, so as to consider the enhanced resilience achieved when such systems are adopted.

The TMS 402-13/ACI 530-13/ASCE 5-13 and the CSA S304-14 ignore the system-level response in their masonry wall design procedures. The TMS 402-13/ACI 530-13/ASCE 5-13 does not consider the slabs as a coupling element of RM shear walls. The seismic design provisions (*Clause 16*) of CSA S304-14 also note that *"the benefits of minor coupling through continuity of floor slabs may conservatively be ignored"*. However, the results showed significant discrepancies between the component-level wall responses and the associated system-level responses due to the diaphragm-wall coupling. Although this coupling enhanced the system strength and stiffness, this enhancement was also accompanied by increased (flexure/shear/sliding) demands on the walls that were not originally accounted for when they were designed and the reinforcement was detailed following the current component-by-component design in TMS 402-13/ACI 530-13/ASCE 5-13 and CSA S304-14. These demands may lead to unpredictable failure modes as weaker links develop within the building system. Moreover, although the system-level (i.e. building) ductility capacity is influenced by the component-level (i.e. wall) ductility capacity, the two ductility capacity values are not equivalent. This difference between component- and system-level ductility should be expected since not all walls respond plastically simultaneously under most practical levels of seismic demands. This indicates the importance of introducing clauses to future editions of TMS 402 and CSA S304 that include new analysis and design procedures to consider system-level aspects that cannot be evaluated through the current traditional component-by-component design procedures.

The distributed plasticity (fiber) model used in this study was able to capture the response of the RM shear walls with different configurations at both the component- and system-levels. The cross-section of the wall in this model was broken down into fibers where materials were defined independently to simulate the stress-strain relations of the masonry and reinforcing steel. However, this fiber model was computationally intensive and sometimes caused solution convergence problems, especially during dynamic analysis. Moreover, the reliability of the fiber model was shown to depend on the assumed plastic hinge length. As such, this dissertation went further into developing an alternative simplified concentrated plasticity (spring) model that was capable of simulating the behavior of RM shear wall systems without and with boundary elements. This simplified model did not require the level of detailed representation that was needed for the fiber model. Elastic beam-column elements were used to model the walls, with the wall inelastic behavior accounted for through zero-length elements with an inelastic rotational spring at the wall base. The spring model is in good agreement with the experimental results in terms of simulating the initial stiffness, peak load, stiffness degradation, strength deterioration, hysteretic shape and pinching behavior at different drift levels. Therefore, this model is expected to be a useful system-level response prediction tool that can be subsequently adapted for the NSP and NDP.

The results in this study showed that the current ASCE/SEI 41-13 modelling parameters assigned for RM shear walls with rectangular cross sections or with boundary elements may be unnecessarily conservative. More specifically, the models (i.e. fiber or spring models), based on those current ASCE/SEI 41-13 parameters, failed to capture the postyield branch of the experimental results at both the component- and system-levels. This excessive conservatism might have resulted from the limited number of experimental studies at the time when these parameters were originally proposed in FEMA 356. This part of the dissertation highlights the fact that these parameters need to be revised as more experimental studies are currently available for SFRS that are composed of RM walls.

The existing procedures to generate system-level fragility curves consider global demand parameters (e.g. inter-story drift) in their risk assessments. However, the results showed that these parameters may not be appropriate for all components. This is because some components may be able to sustain a higher level of demand before reaching a particular damage state when compared to other components, even when all components are made of the same material and meet the same seismic detailing requirements. This highlights the importance of the methodology developed in this study that integrates the contributions of multiple components with distinct fragilities to the overall seismic risk of the complete RM building system. The methodology showed that the building (as a system) is neither more fragile than the most vulnerable individual component nor less fragile than the least vulnerable individual component. Therefore, using simplified but accurate models to account for the vulnerability of all system components would yield more realistic risk assessment for complete building systems.

6.3 RECOMMENDATIONS FOR FUTURE RESEARCH

The research presented in this dissertation included numerical, analytical and experimental investigation and response quantification of RM shear wall systems with boundary elements. However, as in any innovative research focus, several issues remain unresolved and require further investigation. The following points present possible extensions to the research to expand the knowledge related to the system-level seismic response of RM buildings with boundary elements:

1. This study adopted masonry boundary elements detailed as confined columns, which does not deviate from conventional pilasters construction practice. However, special materials could be introduced to the grout mix in the boundary element region in an effort to increase the ultimate strain of the RM in the boundary region, and therefore to enhance the overall

seismic performance of the system and subsequently its resilience under extreme events.

2. This study also demonstrated the influence of the adopted boundary element configuration on minimizing the collapse risk of RM shear walls at both the component- and system-levels. Parametric experimental, numerical, and analytical studies would be very useful in terms of identifying the effects of different parameters on this configuration. For example, walls with larger boundary elements could be tested to investigate the effect of their size on the overall wall response. In this case, recommendations regarding the minimum boundary element size to achieve specific ductility levels could be established.
3. The loading protocol adopted in the experimental work of the four phases was quasi-static fully-reversed cyclic loading. Although this type of loading makes it possible to clearly evaluate the wall damage propagation, additional experimental tests under dynamic loading (e.g. shake table tests) are still needed because they represent demands closer to those experienced during seismic events.
4. Research is needed to study the effect of the axial load level on the RM shear walls response and subsequently on the system-level response.
5. RM shear walls with boundary elements can be easily achieved in construction and possibly without requiring major changes to architectural

practices. Additional full-scale experimental tests with different number of stories would be useful to develop a better understanding of the behavior of RM buildings with boundary elements. Along with scaled-tests, such test results are expected to facilitate adoption of this new SFRS within the TMS 402-22 (2022) and the CSA S304-24 (2024) masonry design codes.